University of Birmingham

Optical Modulation and Carrier Dynamics of Structured Silicon Membranes

by

Ammar Zakar

A thesis submitted in partial fulfillment for the degree of Doctor of Philosophy

in the

Nanoscale Physics Research Laboratory

The School of Physics and Astronomy

October 2017

Declaration of Authorship

I, Ammar Zakar, declare that this thesis titled, 'Optical Modulation and Carrier Dynamics of Structured Silicon Membranes' and the work presented in it are my own. I confirm that:

- This work was done wholly or mainly while in candidature for a research degree at this University.
- Where any part of this thesis has previously been submitted for a degree or any other qualification at this University or any other institution, this has been clearly stated.
- Where I have consulted the published work of others, this is always clearly attributed.
- Where I have quoted from the work of others, the source is always given. With the exception of such quotations, this thesis is entirely my own work.
- I have acknowledged all main sources of help.
- Where the thesis is based on work done by myself jointly with others, I have made clear exactly what was done by others and what I have contributed myself.

Signed: Ammar Zakar

Date:

University of Birmingham

Abstract

Nanoscale Physics Research Laboratory
The School of Physics and Astronomy

Doctor of Philosophy

by Ammar Zakar

In this work, the potential and feasibility of using structured silicon membranes as an active electro-optical light modulators in the Mid-Wave Infrared $MWIR$ range are evaluated and compared. The study involved using Near IR pump-Mid IR probe to investigate the spectral, fluence dependence and time dependence optical properties of the nanoporous $npSi$ and microporous $mpSi$ silicon structures. The results the spectral feature of both samples is structure dependent parameter including the skeleton dimensions, pore size distribution and porosity of the sample. The spectral characterisation indicated that the ground state transmission for both membranes is about 90% with 60% achievable modulation when pumped at fluences less than $5mJ/cm^2$. The $npSi$ sample demonstrated response time as fast as few tens of picoseconds allowing its use in the GHz regime, while the $mpSi$ demonstrated response time three orders of magnitude slower with a possibility of operating in the MHz regime.

The recombination of the excited carrier for both samples are also evaluated and compared at different excitation fluences. The results demonstrated that the carrier recombination of the excited $mpSi$ follows Shockly Read Hall SRH process with recombination coefficient of about $1.65s^{-1}$. The situation is different with $npSi$ membrane since it demonstrated that the SRH dominating the recombination at low excitation fluences, while at high excitation fluences, the Auger recombination type competes with the SRH or even become faster at some probe wavelengths. However, The $npSi$ membrane demonstrated longer SRH recombination time at $3.5\mu m$ probing wavelength which attributed to the vibrational-electronic state coupling.

Acknowledgements

First and foremost I would like to express my deep gratitude to The Higher Committee For Education Development in Iraq for their support during the years of study, without their support this thesis would not have been completed. I would also like to thank my supervisor, Dr. Andrey Kaplan, who accepted me as a PhD student and for his professional supervision and guidance. He has always given me great support throughout my PhD project. Without his consistent encouragement, I would not have been able to complete this thesis.

I would also like to thank Prof. Leigh Canham for providing the nanoporous silicon samples used in this study. My sincere thanks also goes to to Dr. Guixin Li for the FTIR measurements.

Im very thankful to Dimitri Chekulaev for his guidance and contribution in constructing the pump-probe setup. I also thank my fellow lab-mate Sung Jin Park for the stimulating discussions and his contribution in obtaining the experimental results. My special thank goes to my colleague Vera L. Zerova for her contribution in calculating the optical response of the nanoporous silicon. I would also like to express my gratitude to my colleague Rihan Wu for here great contribution in analysing some of the experimental results related to the carrier dynamics in nanoporous silicon. I would also like to thank everybody in the group for letting me have a good time besides the hard working research.

Last but not the least, I would like to thank my family: my parents and to my brothers and sister for supporting me spiritually during the many years of study.

Contents

List of Figures

List of Tables

Abbreviations

OPO	Optical parametric oscillator
OPA	Optical parametric amplifier
HHG	High order harmonic generation
MWIR	Mid-wave infrared
LWIR	Long-Wave infrared
OEICs	Optoelectronic electric circuits
QCL	Quantum cascade laser
nc−Si	nano crystalline silicon
c−Si	Crystalline silicon
a−Si:H	Amorphous silicon Hydrogenate
FTIR	Fourier transform infrared spectroscopy
$mpSi$	microporous silicon
$npSi$	nanoporous silicon
K−K	Kramer-Kronig relation
MG	Maxwell Garnett
WKB	Wentzel−Kramers−Brilloun
Ti:Sapphire	Titanium:Sapphire
DFG	Different frequency generation
EMA	Effective medium approximation
FWHM	Full width at half maximum
VB	Valence band
CB	Conduction Band
p−	Lightly doped p−type silicon
p+	Heavily doped p−type silicon

Physical Constants

c	Speed of light in vacuum	$(2.99792 \times 10^{8})m/s$
h	Plank's costant	$(6.62607 \times 10^{-34})J.s$
	$\hbar = h/2\pi$	$(1.05457 \times 10^{-34})J.s$
ϵ_0	Free space permittivity	$(8.85419 \times 10^{-12}F/m)$
e	Electron charge	$(1.60218 \times 10^{-19}C)$
m_e	Free electron mass	$(9.10938 \times 10^{-31}kg)$
μ_0	Free space permeability	$(4\pi\cdot)10^{-7}$

Symbols

q	Integer number	
d	Thickness of the layer	m
I	Intensity	W/m^2
r	Reflection coefficient	
t	Transmission coefficient	
E_i	Electric field of the incident light	
E_r	Electric field of the reflected light	
N	Complex refractive index of the material	
n	Real part of the complex refractive index	
k	Imaginary part of the refractive index	
ϵ	Complex dielectric function	
α	Absorption coefficient	m^{-1}
E	Photon energy	eV
θ_i	incident angle	degree
θ_r	reflection angle	degree
R	Reflectance	
T	Transmittance	
ω	Angular frequency	rad/s
ω_p	Plasma frequency	s^{-1}
Γ	Damping rate	s^{-1}
R_0	Reflection without pump	
T_0	Transmission without pump	
F	$Fluence$	J/m^2

m_e Optical mass of the excited electron

m_h Optical mass of the excited hole

To my Family and all Friends

Chapter 1

Introduction

In the past few decades, the optical properties of the silicon and silicon derivative materials have attracted great attention due to their technological importance [1–4]. Using these materials in different technological areas requires a deep understanding about the carrier dynamics including mobility, band structure , phonons and many ultrafast processes . The emergence of ultrafast lasers which have the ability of providing pulses with time duration less than $10fs$ ($1fs = 10^{-15}s$), the time resolution of various spectroscopic approaches have been highly improved. Moreover, using a solid state laser to pump optical parametric oscillators (OPO) provide the capabilities of extending the tunability range. Availability of such laser sources with tunable parameters such as pulse width, pulse repetition, wavelength etc, have allowed investigation into not only the wide range of physical phenomena but also feasible applications of emerging technologies. Recent advances in ultrafast spectroscopy have yielded various spectroscopic approaches such as generation of sub-femtosecond pulses using high order harmonic generation (HHG) [5]. Investigation of optical properties of semiconductor materials using pump-probe spectroscopy based on either reflection and transmission, or photoluminescence geometries [6–10]. Moreover, the optical pump-terahertz probe technique has been recently used to investigate frequency dependant conductivity [11–15]and z-scan method was also used to evaluate the optical non-linearities [16–18]. This chapter

focuses on background review of carrier dynamics in semiconductors. In particular, the mechanisms of light intensity modulation using structured silicon samples as well as optically excited carriers and recombination process that follows optical excitation. This is performed using different optical approaches such as time resolved optical pump-MIR probe reflection and transmission, pump power dependence and spectral dependence reflection and transmission for nanoporous silicon (npS)as well as micro hole arrays silicon(mpSi). Since mid-infrared light was used as a probe to detect the optical properties change in the porous silicon, the vibrational modes in the porous silicon are also presented.

1.1 Motivation

The fast optical modulator for infrared and thermal cameras as well as telecommunication networks has attracted considerable attention recently due to its availability and high performance. Previously, there were limited options for cameras operating in mid-wave infrared(MWIR) as well as long-wave infrared (LWIR)regimes. Such cameras are heavily based on electro-mechanical optical modulators which, although being well sophisticated and effective technologies have drawbacks associated with modulation response, mechanical stability, and component dimension [19, 20]. The realization of reliable electro-optical modulators provide capability to overcome not only the inherent limitations observed in the electro-mechanical modulators but could also enables new tendencies to achieve time-of-flight and hyperspectral imaging, fast non-uniform correction and rapid protection of activated sensors. Moreover, it is expected that the next generation of the signal transfer and communication technologies are likely to be reliant on switches and optically controlled modulators [21–23]. Despite the availability of well developed components of (NIR)silicon photonics that operate in optical communication regimes as all- optical and electro-optical modulators [24–27],the number of optical components capable of operating in mid-wave infrared (MWIR)and long-wave infrared (LWIR), covering the wavelength spectral range between 3 and 12 μm, are considerably small [19]. Furthermore, silicon photonic platforms have recently extended

to cover various mid-IR application including bio-chemical sensing, medicine, industrial control, wave guiding and much more [28–30]. The integration of electronic circuits with different optical components such as ultrafast optical modulators, switches and detectors will be the most required optical parts for the next generation of optoelectronic electronic circuits(OEICs) [31–34]. In addition, current available cost effective fabrication processes makes silicon structures as a potential candidates to operate as active modulator, filters and infrared light guiding beyond absorption edge of silicon [34, 35].

The transmitted light through optical modulators can be controlled using an external light source to alter the optical properties of modulator. The two widely used mechanisms for optical modulation and switching implementation mainly rely on the plasma effect [36, 37] and thermal effect [38]. However, many studies showed that there is no significant contribution of both Kerr and Franz-Keldysh effects in silicon [25, 37]. In the case of plasma effect, the externally excited electron-hole pairs can be exploited to control the light transmitted through the optical modulators by changing the optical properties of the device which in turn to change the real and imaginary parts of the dielectric function of the device [37]. The reliability of exploiting plasma effect in optically modulated MWIR components comes from the fact that such devices have the capability of providing fast switching speed associated with carrier life time and less accounted noise.

With invention of laser sources,which mainly operate based on intersubband transition such as quantum cascade laser QCL, modulate such light sources by optically controlling the reflectivity of laser cavity facets has been realized [39, 40]. Many studies investigated the feasibility of using nanocrystalline(nc-Si)as a promising material in the technology of optical modulators and switches. These studies indicated that the (nc-Si) possess absorption cross section associated with free carriers are one order of magnitude greater than of that in bulk silicon, this can be exploited in the development and application of emerging technoloies [41–43]. On the other hand, other studies have demonstrated the enhancement of the dielectric function associated with free carriers for (nc-Si) at longer wavelengths which can be regarded as a feature of intensity modulation in the MWIR and LWIR regimes

[44, 45]. Although the optical components used in infrared regime have attracted a considerable interest, the number of studies investigating the feasibility of using crystalline and nanocrystalline silicon remains limited, these works were usually covering a narrow part of the spectral band or a few single wavelengths while the remnant of the MWIR spectral range remains undetectable.

1.2 Excitation and relaxation dynamics in silicon

Many interesting and ultrafast physical processes in semiconductor materials occur in the femto and picosecond time scales. At high power levels, illuminating the condensed matter with an intense and short laser pulse may lead to either melting or sample ablation within short time scale. In the case of lower power, the situation is different since the sample will absorb the energy from the laser pulse and dissipate it as heat. The observation of melting or heating effects can be obtained using electrical measurements. However, realizing the sequence of steps that follow the excitation,at which the pulse energy first absorbed by electrons then released to the lattice, can be achieved using pump-probe approach and short laser pulses. This approach allows the identification of several ultrafast processes such as carrier excitation, carrier cooling through scattering, carrier redistribution, and carrier diffusion and recombination. The time sequence of these processes can not be distinguished separately since they may overlap in time. This ambiguty in time makes the isolation of a single process rather complicated, especially for carrier densities greater than $10^{20} cm^{-3}$ [46]. In the case of a pump-probe approach, the excitation pulse is typically weak at which the generated electron-hole pairs are in the range of $10^{15} - 10^{19} cm^{-3}$ which allows investigation of electron and phonon dynamics in laser excited semiconductors [46]. The importance of evaluating such ultrafast processes lies in their significant contribution in the optimisation and minimisation of emerging optoelectronic devices [47–51]. Under equilibrium conditions, the

distribution of free carriers in semiconductor materials follows Fermi-Dirac statistics while the phonons are distributed according to Bose-Einstein statistics [52]. In the absence of any excitation, the alternation of energy and momentum occurs through either carrier-carrier or carrier-phonon scattering resulting in a common temperature for both distributions. Thus, the average momentum for both carrier and phonon regimes reaches zero while their average energies can be described based on their common temperature. This equilibrium condition disrupts once the semiconductor absorbs the optical electromagnetic radiation yielding various thermal states for both regimes. However,once the external excitation is removed, the excited carriers in the semiconductor recover the equilibrium condition within a short period of time. At this stage, the average momentum reaches zero while the average temperature of the carriers will be in equilibrium with lattice temperature due to energy and momentum relaxation via various scattering channels.

Figure 1.1 shows the schematic illustration of ultrafast processes in direct band gap semiconductors excited using a monochromatic polarised laser assumed to be a delta function in time which is an approximation of a real ultrashort pulse excitation. Optical excitation of semiconductors with the pulse energy greater band gap E_g, yields in generation of electron hole pairs with with excess kinetic energies identical to the residual energy ($\hbar\omega_o - E_g$). The initial photoexcitation using monochromatic and polarised light result in narrow energy distributions of electrons $\delta(E_e)$ and holes $\delta(E_h)$ respectively. The distribution is governed by the Pauli exclusion principle and peaked at a specific directions $\delta(|k_e|)$ and $\delta(|k_h|)$ in momentum space as it is shown in Figure 1.1(a)

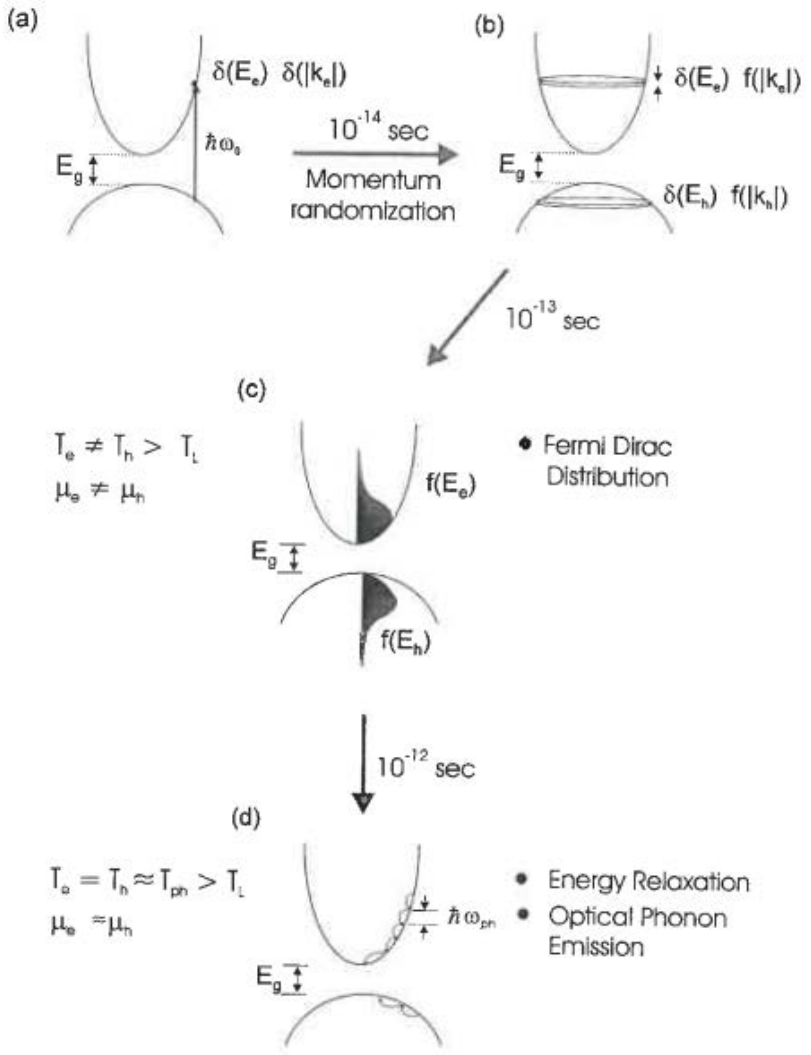

FIGURE 1.1: Schematic illustration of semiconductor photoexcitation and followed relaxation processes:(a)Immediately after photoexcitation, the energy and momentum of the excited carries will posses delta function.(b) The momentum randomisation occurs within tens of femtoseconds.(c) Carrier densities greater than $10^{19} cm^{-3}$ thermalise into Fermi-Dirac destribution through carrier collision within $10^{-13} s$.(d) As time evolves, the hot carriers reach thermal equilibrium with lattice where the carriers lose their excess kinetic energy through hot carrier - optical phonon scattering process [53].

This process is then followed by momenta randomisation through an elastic and inelastic scattering event within tens of femtoseconds time period Figure 1.1(b). Following photoexcitation, the electrons possess most of the excess kinetic energy due to smaller effective mass compared to the holes. This case suggests that both electrons and holes can be regarded as separated individual regimes with different

thermal distributions each yielding weaker electron-hole interactions compared to that shown in other carrier-carrier regimes. It should be mentioned that the collision of electron-electron or hole-hole are density dependent process. For carrier densities above $10^{19} cm^{-3}$ with thermal energies around $1000K$, the thermalisation of carriers into a Fermi-Dirac distribution occurs through carrier-carrier collisions on the time scale of $10^{-13} s$ Figure 1.1(c). The subscripts L,e and h shown in the Figure 1.1 refer to lattice, electrons and holes respectively while the temperature and chemical potential are illustrated as T and μ respectively. The distribution function temperature of electrons $f(E_e)$ differs from that assigned for holes $f(E_h)$,which could be lower or higher than lattice temperature, since they mainly depend on applied photon energy $\hbar\omega_o$. With the time evolution, the hot carriers attempts to attain the equilibrium with the lattice. In this case, hot carriers release their excess kinetic energy via different scattering process. The most efficient scattering process is assigned to optical phonon production where the population of non-equilibrium phonons increases due to interaction with carriers and thermalise with other lattice modes within picosecond time scale through phonon-phonon scattering processes.

1.2.1 Ultrafast Carrier Dynamics

In the last section we introduced various ultrafast processes following the excitation of semiconductors using above band gap laser pulses. Figure 1.2 summarises the time scale characterisation for different dynamical processes of electrons and lattices in semiconductors [46]. Absorption of above band gap electromagnetic radiation by a semiconductors yields the generation of high density of non-equilibrium carriers with relatively high carrier temperatures. Several orders of magnitude carrier densities above equilibrium can be achieved depending on the photon energy and the employed laser fluence. Moreover, the high carrier temperatures, few thousand degrees,can also be reached. The temperature change alters different microscopical parameters especially those in relation with various optical properties of the material. Following optical excitation, the spatial and temporal evolution

of electron and holes occur with characteristic times which in turn depend on the number relaxation process being involved as it is described in previous section. The carriers undergo primarily to the energy relaxation process through optical phonon emission while the situation is different with holes since the interaction with optical phonon occurs near the Brillouin zone center.

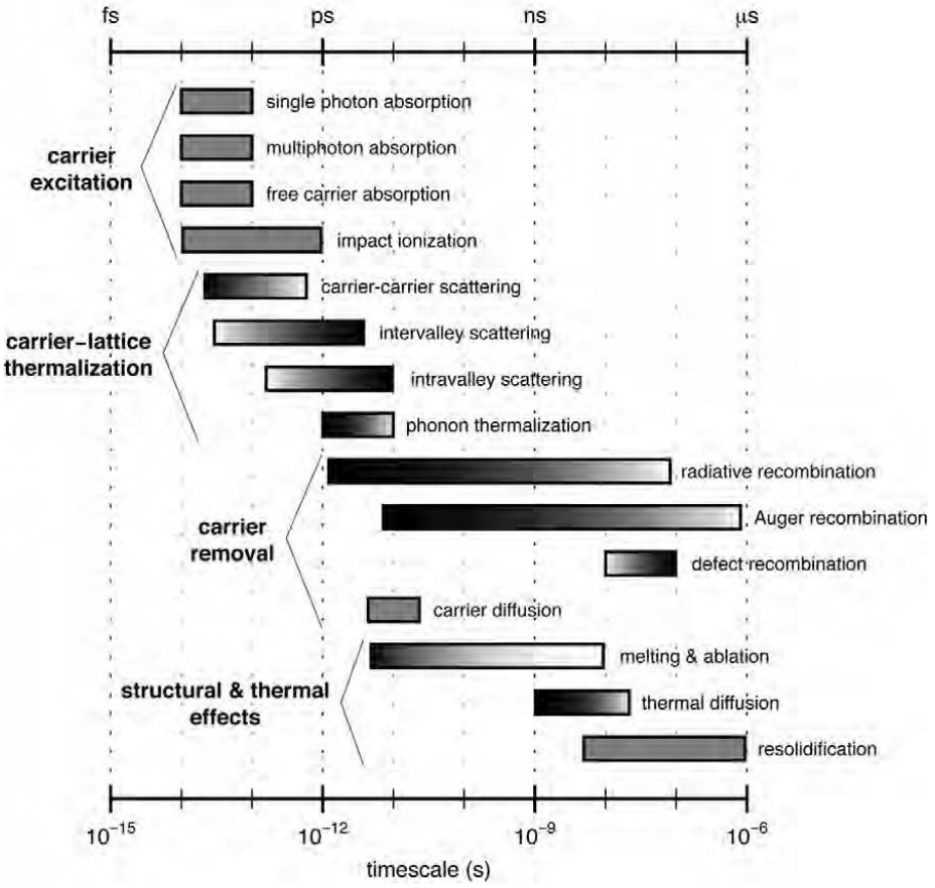

FIGURE 1.2: Characteristic time scales for different dynamical processes in semiconductor. the bars indicates the rough time scale expected for carrier density between 10^{17} and $10^{22} cm^{-3}$. The color gradient within the bar indicates the time scale dependence on the carrier density where the dark and light ends indicates the characteristic time scales at high and low carrier densities [46].

In addition to phonon scattering processes,it should be mentioned that the scattering of carriers in nano-structured or amorphous semiconductors may involve interaction with defect states or material boundaries (in the case of multi phase material). Many studies have showed that there is still a lack of information about the carrier scattering mechanisms in such structured materials [54–58].

1.3 Optical Characteristic of Semiconductor Excited States

The technology that exploits silicon in various optical functionalities is called silicon photonics. This field has attracted considerable attention recently due to the availability of various fabrication processes of nano-structured samples as well as the capability of controlling size and shape morphology. Adoption of such nano-structuring provides the possibility of realising the silicon structures with potential to operate as an active component in different application such as modulators, sources,detectors and applications of photo-voltaics, optical resonators and sensing [59]. Then, the fabrication of such devices requires a careful understanding of the carrier dynamics in these types of photonic materials, which in turn provides clear understanding of how the device should be fabricated. Despite enormous studies that have been conducted to investigate nanostructured silicon with various morphologies, only a few studies were focused on the investigation of carrier dynamics in such types of materials [12, 60–62]. The terahhertz spectroscopic technique has been previously performed to investigate nano-structured silicon where various processes can be revealed since the interaction length of the terahhertz radiation is comparable with embedded nano-structure dimensions. The measurable length, which represents the ratio between diffusion coefficient$D$ of carriers in material and the frequency of the probe ω, can be expressed by $L_\omega = \sqrt{D/\omega}$ [15]. In bulk materials, the carrier-carrier scattering has been shown to be on the order of $10fs$, followed by carrier relaxation towards the edge of the band and finally the inter-band transition takes place which lasts for nearly several nanoseconds [63]. The study also reported that nano-structuring semiconductor materials provides the possibility of altering the characteristic relaxation time scale of the carriers. Many ultrafast studies about whether the change of optical properties can provide deep understanding of the transient dynamics of surface electrons have been carried out [64–66]. Since the emerging of ultrashort laser sources, there have considerable interest in carrier dynamic and phase induced transitions in various types of materials such as dielectric, metals and semiconductors [67–71]. Shank et al[63]

have performed pioneering work that investigates the contribution of generated charge carrier N_{eh} on the optical characteristics of crystalline silicon. The study exploited simple Drude model expression to estimate the refractive index as well as the contribution of generated electron-hole plasma to the sample reflectivity [63].

$$n_p = n_c(1 - \omega_p^2/\omega^2)^{1/2} \tag{1.1}$$

Where, n_p and n_c represent the plasma and unperturbed crystalline silicon refractive indices respectively, ω_p is the frequency of the generated e-h plasma and ω is the frequency of the incident light. It should be noted that the contribution of the imaginary part of the refractive index is ignored from the model in the work of Shank and many other studies. Such assumptions can not be applied when dealing with more complicated samples [72–75]. The Equation 1.1 implies that the refractive index and as a result the reflectivity decreases when probing the sample with frequency ω bigger than that of the e-h plasma frequency ω_p. In this case, measurements of refractive index change $\Delta n_p(\tau)$ provides the possibility of estimating the e-h plasma frequency.

$$\omega_p = (N_{eh}e^2/m_e\epsilon_o) \tag{1.2}$$

Here, m_e and ϵ_o represent free electron mass and free space permittivity respectively. For optical properties estimation, the theoretical relation should be connected to the absorption, transmission and the reflection of the sample.

It has been proposed that the measured reflectivity change can be controlled through two linear contributions: the first one is related to the contribution of conduction band free carriers to the dielectric function while the second one is attributed to the contribution of recombination process(interband transition).The free carrier related contribution can be dealt with using simple Drude model as demonstrated in Shank's work [63].On the other hand, the contribution of inter

band can be assigned for various processes such as state filling,band gap renromalization and changes in lattice temperature. In some cases where the real part of the dielectric function $R(\varepsilon)$ is much bigger than the imaginary part $I(\varepsilon)$ and $R(\Delta\varepsilon) \geq I(\Delta\varepsilon)$, the change in reflectivity can be assumed to be only due to the change in the real part of the dielectric. This hence allows the connection between the reflectivity and the change in the real part of the refractive index n through Fresnel formula as follows:

$$\frac{\Delta R}{R} = \frac{4n_0\cos(\phi)}{(n_0^2-1)(n_0^2-\sin^2(\phi))^{1/2}}\Delta n_p \tag{1.3}$$

Here, ϕ and n_0 represent the angle of incidence and the ambient refractive index respectively. The above equation is applicable only for very small change in the refractive index.It has been shown that the contribution of the following effects: state and band filling, band structure renormalisation and the free carrier response to the effective dielectric function can be treated as nearly independent according to [76].

For the sake of the simplicity each effect has assumed to contribute separately to the effective dielectric function of the excited sample:

$$\varepsilon^* = \varepsilon_g + \Delta\varepsilon_{pop} + \Delta\varepsilon_{bgs} + \Delta\varepsilon_{fcr} \tag{1.4}$$

Where ε_g represents the dielectric function of the unexcited sample, which is around $13.656 + i0.048$ for silicon at 800 nm wavelength according to[77]. while $\Delta\varepsilon_{pop}$,$\Delta\varepsilon_{bgs}$ and $\Delta\varepsilon_{fcr}$ refer to the contribution of state and band filling, band gap renormalisation and free carrier response to the dielectric constant respectively.

Detailed explanation of state and band filling needs a deep understanding of the distribution of the carriers in both conduction and valence bands. However, since the generated plasma possess a temperature above $1000K$, it plausible to regard the distribution of the free carriers as nearly uniform across the Brillouin zone. Thus, the estimation of the state and band filling to the dielectric constant $\Delta\varepsilon_{pop}$

can be simply obtained through the ratio of the excited electron-hole pair $N_{e-h}$and the density of the valence band electrons N_0, according to [78]. In the case of silicon, the total density of the valence band is equal to $N_0 = 2 \times 10^{23} cm^{-3}$, in the absence of any excitation the dielectric change due to state and band filling can be described as follows:

$$\Delta\varepsilon_{pop} = -(\varepsilon_g - 1)\frac{N_{e-h}}{N_0} \tag{1.5}$$

Therefore, the rough estimated value for this change can be calculated through $\Delta\varepsilon_{pop} \approx -(13.6 - 1) \times \frac{5\times10^{20}}{2\times10^{23}} = -0.03$.

In case of band structure renormlisation, the many body interaction yields a change in energy of the single particle in the excited plasma which in turn lead to rigid shift of band structure. As a result, the shrinkage of the energy gap ΔE_{gap} occurs and the deviation from cubic root of the density role can be expected due to the dependence of the energy gap ΔE_{gap} on the temperature. Ignoring the temperature dependence yields an estimation of the optical properties changes using the rigid band shift model. In this model,the shift in the rigid band can be estimated from the corresponding shift of the optical spectra as follows:

$$\Delta\varepsilon_{bgs} = \varepsilon_g(\hbar\omega + \Delta E_{gap}) - \varepsilon_g(\hbar\omega) \tag{1.6}$$

It has been demonstrated that for $50meV$ band gap renormalisation the optical properties change based on the above equation can be estimated to be $\Delta\varepsilon_{bgs} = 0.01$ according to [79].

As mentioned before, the contribution of free carriers to the optical properties, far from the plasma resonance, can be described by Drude model as follows:

$$\Delta\varepsilon_{fcr} = -\frac{N_{e-h}e^2}{\varepsilon_0\varepsilon_{host}m_{opt}\omega^2}\frac{1}{1 + i(\omega\tau_D)^{-1}} = -\left(\frac{\omega_p}{\omega}\right)^2(1 + i(\omega\tau_D)^{-1})^{-1} \tag{1.7}$$

Where, ε_0, ε_{host} refers to the dielectric constant of the ambient and the host material respectively, while ω, ω_p and τ_D represent the frequency of photo excitation, the plasm frequency and collision time (damping time)respectively. m_{opt} refers to the optical effective mass of the carriers. Since the optical effective mass for the carriers is proportional to mobility effective mass for the electron m_{eff} and the holes m_{heff} through the relation $m_{opt} = (1/m_{eff} + 1/m_{heff})^{-1}$; thus the relation between the total mobility and the optical effective mass can be described by $\mu \propto 1/m_{eff} + 1/m_{heff} = 1/m_{opt}$. For silicon, it has been shown that, at dense plasma, the optical mass varies between $0.156m_e$ and $0.205m_e$ at the plasma temperatures $300K$ and $2000K$ respectively. The Drude damping τ_D has been shown to be temperature and carrier dependant parameter. Thus, at low carrier densities the damping time has been found to be on the order hundred of femtosecond which is estimated from carrier-phonon collision. While at high carrier densities the situation is different since carrier - carrier collisions is dominated and the magnitude of the damping time is two order lower.

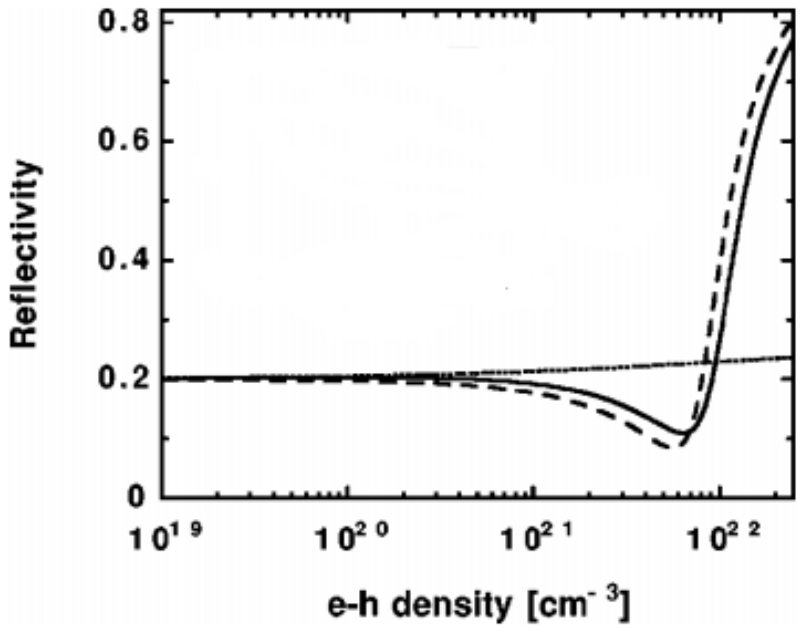

FIGURE 1.3: shows silicon reflectivity as a function of carrier density predicted theoretically at the angle of incidence 45^o, $625nm$ and p polarised light. Dotted line shows band filling and band gap shrinkage contributions respectivily.While dashed curve shows the contribution of the pure Drude model; solid line total reflectivity based on the Eq.1.4[76]

The approximate estimation of the contribution of free carriers to the dielectric constant yields $\Delta\varepsilon_{fcr} \approx -(\omega_p/\omega)^2$ at 800 and $N_{e-h} = 5 \times 10^{20}$. Summarising all the previous contributions, it can be concluded that the main contribution to the dielectric constant is due to the free carrier response,while the other contributions have minor or negligible effects and are ignored for the sake of calculation simplicity. Figure.1.3 shows the p- polarised reflectivity change of silicon as a function of carrier density at $625nm$ wavelength.The figure shows the contribution of the combination of the state and band filling as well as band gap renormalisation estimated according to the Equation 1.5 and Equation 1.6 (dotted curve). The relatively small change in the reflectivity attributed to the opposite signs of both contributions. The figure also shows the contribution of free carrier response according to pure Drude model(dashed curve). It can be seen from the figure that the contribution of free carriers(Drude model contribution)on the reflectivity is relatively small at low carrier densities while it shows significant increase at higher carrier densities.

On the other hand, the effect of lattice temperature on the dielectric constant can be numerically estimated using linear thermo-optical coefficient (dn/dT_L)according to [80]:

$$\Delta n_{LT} = \left(\frac{dn}{dT_L}\right) \Delta T_L \tag{1.8}$$

Where T_L represents lattice temperature and Δn_{LT} is the change in refractive index due to lattice temperature. The thermo-optical coefficient (dn/dT_L) for wavelength relevant to our study is approximately3.4×10^{-4} [80]. Therefore, a rough estimation of the refractive index at lattice temperature of approximately $1000K$ is ~ 0.005 and as a result $|\Delta n_{LT}| \ll |\Delta\sqrt{\varepsilon_{fcr}}|$. This indicates that the optical properties change due to lattice temperature is less significant or even negligible comparing to that estimated for free carrier contribution. Thus, this conclusion provides the possibility to deal with the change in optical properties of silicon in the frame of the free carrier contribution only.

1.4 Vibration Modes in Porous Silicon

The preparation of porous silicon reveals various vibrational modes during sample fabrication which can be investigated using FTIR spectroscopy as shown in the Figure.1.4.

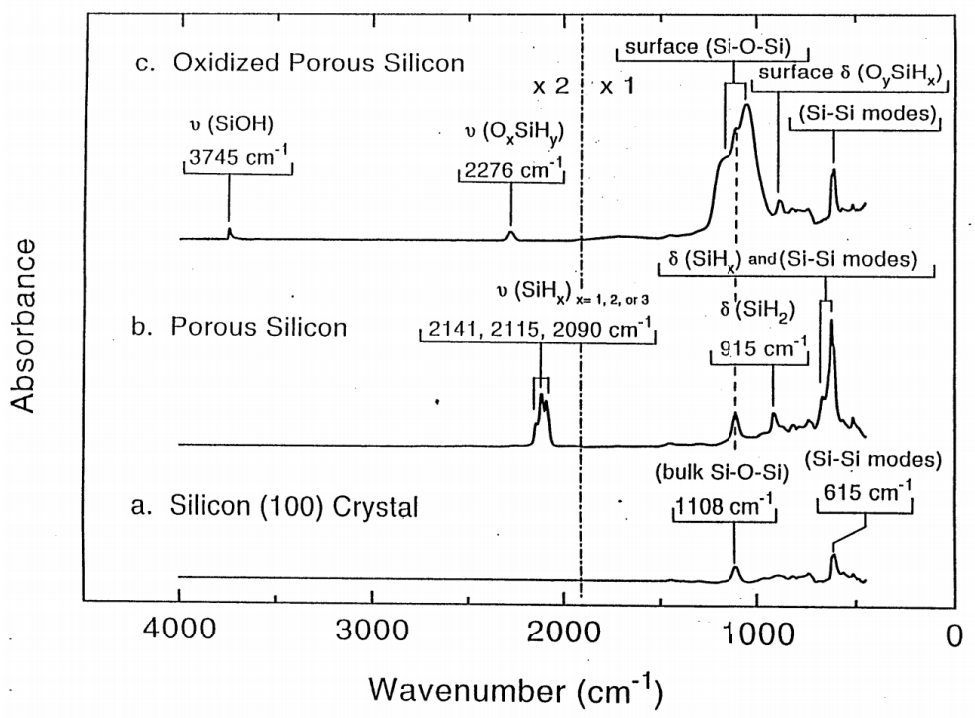

FIGURE 1.4: FTIR Spectra measured at $298K$ for (a) silicon (100) crystal (b) porous silicon and (c) oxidized porous silicon. The figure presented to show the contribution of various vibrational modes of the silicon during fabrication process [81].

For unetched silicon (100) crystal the contribution of various crystal impurties together with Si-O-Si can be assigned at $1108cm^{-1}$ Figure.1.4(a). While for electrochemically etched silicon, the spectrum introduces a bunch of new absorbencies. The assigned peaks at $2141cm^{-1}$, $2115cm^{-1}$ and $2090cm^{-1}$ indicate the contribution of the $SiH_{x(3,1,2)}$ stretching modes respectively [81], Figure 1.4(b). At longer wavelengths(lower wavenumbers), the contribution of Si-O-Si is still exist with manifestation of new feature at $915cm^{-1}$ which is assigned for SiH_2 vibrational mode. Moreover, various overlapped absorption peaks at $666cm^{-1}$, $622cm^{-1}$ and $615cm^{-1}$ are respectively observed and attributed to SiH_x deformation modes.

Figure.1.4(c) also shows that the porous silicon after heavy oxidation produced new vibrational modes in the spectrum which attributed to the contribution of $Si-OH$,O_ySiH_x and $Si-O-Si$ vibrational modes respectively.

1.5 Research Content

This thesis is categorised into six chapters, the first chapter provides a background review about the carrier dynamics and the motivation of studying the optical properties of silicon and silicon derivative materials. The chapter also illustrates carrier dynamics in silicon and focuses on the generation of the electron hole pairs as well as the the relaxation processes following excitation. Since this study deals with carrier dynamics of nano and micro porous silicon in the Mid infrared range, the vibration modes in the porous silicon are also considered here.

The second chapter provides information about the fabrication process of producing the the micro and nano porous silicon using electrochemical etching. The chapter also includes some characterisation procedure to investigate the optical properties of porous silicon. The comparison between the optical properties of porous silicon structure and many other silicon morphologies are also illustrated.

In chapter three, detailed information about the laser system is explained together with reflection and transmission principles as they might be used in the derivation of the transfer matrices of the samples. Different models used to obtain the optical properties of the various silicon structures are also explained. The interconnection between the transfer matrix method and the dispersion relation and effective medium theories including Maxwell Garnett and Bruggeman models is also covered. Detailed information about the ultrafast pump-probe technique and related optical setup are introduced. The simulation procedure and an example about the capability of our optical model to obtain the optical properties of nano and micro porous are also presented.

In chapter four, we investigate and compare the possibility of using nano porous and micro porous silicon (ordered hole arrays) as an optically controlled modulators operating in the wavelength range between $3.3\mu m$ to $5\mu m$ of the Mid Wave infrared (MWIR)spectrum. The pump- probe technique is used to measure the spectral, fluence and transient dependence reflection and transmission for different sample thicknesses. The spectral section includes a comparison of the FTIR measurements of the nanoporous $npSi$ and microporous silicon $mpSi$ for different sample thicknesses. The fluence dependence section covers the reflection and transmission changes for the same samples mentioned in the spectral section and the related simulated absorption coefficient as well as the carrier concentration extracted from the optical model. The last section in this chapter compares the modulation speed for both nano and micro porous silicon structures.

Chapter five illustrates and compares the recombination decay of the nano and micro porous samples . The model based on the Maxwell Garnett model is employed to extract the transient carrier concentration from the time resolved at different excitation powers. From the model the corresponding carrier concentration at the maximum transmittance change is extracted. The rate equation with two recombination coefficient is used to extract the related recombination process for both samples.

Chapter six summarises the concluded findings of this work and provides suggestions about how to improve the optical modulation in structured silicon membranes.

Chapter 2

Fabrication and Optical Properties of Porous silicon

2.1 Introduction

This study focused mainly on optical properties of two novel semiconductor structures. The first one is micro porous silicon ($mpSi$),which contains an pattern of 0.8μm holes separated by 1μm on a hexagonal 2D lattice. The second sample is nanporous silicon structure ($npSi$) that composed by ambient holes and crystalline silicon nano wires. This chapter encompasses a review of the fabrication procedure, characterisation methods, and optical properties of both $mpSi$ and $npSi$ respectively.

2.2 Fabrication and characteristic of Nano and Micro porous Silicon

Silicon substrates are considered as high quality single crystals with no contribution of defects, low assigned impurities and with the possibility of controlling the

amount of dopants. Following the standard method used in microelectronic fabrication, the surface could be also prepared flat. Thus, unidirectional pore formation on such materials is intriguing as the corrosion pitting the is associated with defects of the material as well as the passive layer leakage. The general method used to fabricate porous silicon is through electrochemically etching a crystalline silicon wafer [82]. The result yields a sponge like network with pore size less than $100nm$ and wire diameter less than $50nm$. The nanometer-scale silicon provides unique features that have significant effect on optical and electrical properties such as higher surface to volume ratio, small pore size compared to probe wavelength and confinement of carrier mean free path compared to that shown in bulk silicon.The porous silicon was generally fabricated using etching system shown in the figure 2.1.

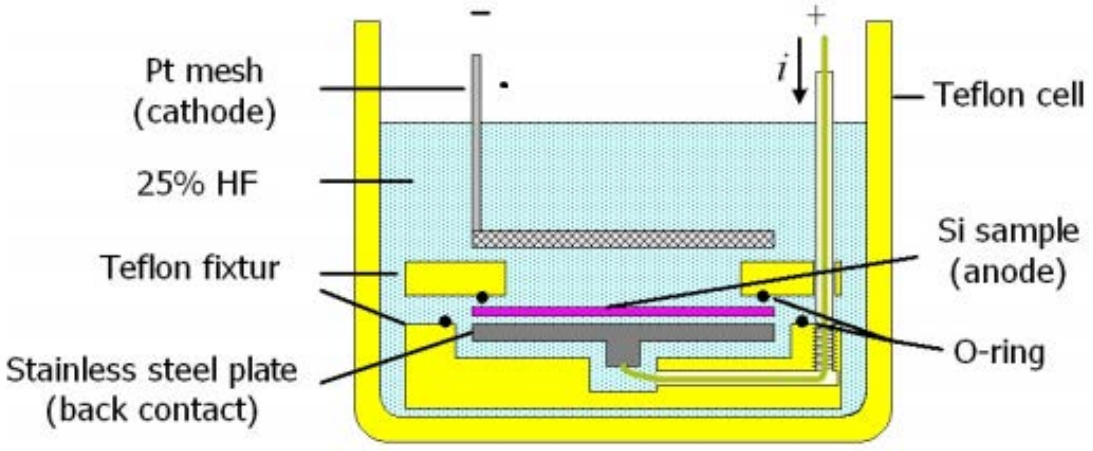

FIGURE 2.1: schematic digram of porous silicon etching system. The figure is taken from [83]

The samples for this study were fabricated using electrochemical etching at various conditions depending on sample structure. Electrochemical anodisation of Si(100) wafer using methanol electrolyte and 40% HF in ratio 1:1 to fabricate nanoporous materials at current density $30mA/cm^2$. The resulting porous layer was separated from the substrate by applying a current density (120 mA/cm^2) for 10s before removing it from electrolyte[84]. Different porous silicon thicknesses can be achieved by precisely controlling the anodisation time. The obtained porous membrane was

then rinsed in methanol and air dried. It should be noted that various pore geometry and morphologies can be obtained by electrochemically etching the silicon wafer. The features of the produced structure rely not only on the etching process but also on the amount of doping level,etching current,concentration of HF. [85, 86]. Among these parameters, the etching current is the most critical parameter in the microporous silicon fabrication process since it leads to homogeneous growth of pores. To achieve that the etching current should be synchronized with pore growth which in turn led to a collection of well arranged cylindrical pores [87]. According to Lehmann's law, this can be accomplished by constantly illuminating the back side of the Si wafer in conjunction with etching process. Otherwise, the process results in collection of cone like generated pores with diameter changing from top of the hole to the bottom. Moreover, this technique can be also used to produce 2D infrared photonic crystals with well ordered and straight pores. This process includes coating micropore arrays using a lithographic mask after the electrochemical etching process [87]. The porous silicon samples used in this study had thicknesses 13μm, 27μm and 111μm respectively Fig.2.2(a). In addition, we investigated two micropore samples with thicknesses 16μm and 50μm respectively as it is shown in Fig.2.2(b).

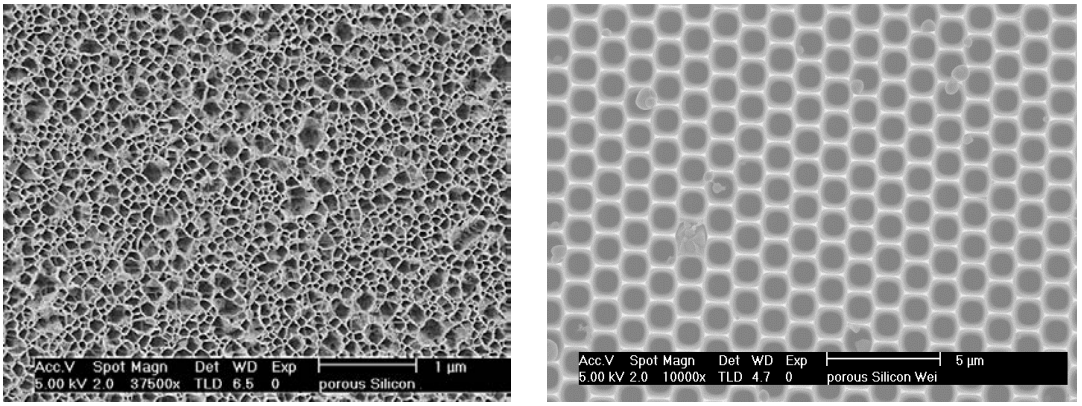

(a) (b)

FIGURE 2.2: SEM cross section imagies of (a)nanoporous Silicon (b) microporous Silicon.

It can be seen from Fig.2.2(a) that the cross section surface of porous silicon contains arrays of randomly arranged holes, while microporous encompasses a well

arranged pores with diameter about 0.8μm separated by 1μm pitch on hexagonal pattern Fig.2.2(b). The microporous silicon membranes $mpSi$ were made by photoelectrochemical etching of silicon in HF using a procedure similar to that described elsewhere [88]. The arrangement of the pores and the interpore distance are defined by a prestructured photo mask.

2.3 Optical Properties of Porous Si structures

Structured silicon membranes have attracted considerable attention since 1990 when the first report suggested the possibility of efficient light emission from porous silicon in room temperature [89]. From that stage, a lot of researches have been conducted to explore the optical properties of porous silicon luminescence. It has been shown that the luminescence of porous silicon covers the range of spectrum from NIR [90] to blue [91] wavelengths. However, most of the studies were focused on the red band where 10% luminescence efficiency had been obtained [92] as shown in Fig 2.3. Following that, the light emission from porous silicon was first confirmed in 1991 [93]and allowed the incorporation of porous silicon light emitting diodes with real world of electronic circuits five years later [94]. This finding has critical impact not only from scientific viewpoint but also the great promise that the material holds in the technology of wide panel displays and optical interconnection. It is therefore essential to investigate the evolution of the population of injected carriers in the temporal and spectral prospectives. Ultrafast techniques have emerged as potential tools to evaluate the carrier dynamics in semiconductor materials. Particularly, the availability of generating stable and short pulses by employing mode-locking technique have been broadened to cover the spectrum from ultraviolet to the far infrared. Moreover, the possibility of using various amplification techniques provide the ability to generate intense light covering most of the spectrum mentioned above. Using different pump-probe schemes, several optical parameters of the semiconductor materials can be evaluated both temporarily

and spectrally. These encompasses reflection [95], transmission [96],and luminescence [97] which can be modulated to extract material related optical parameters such as complex refractive index.

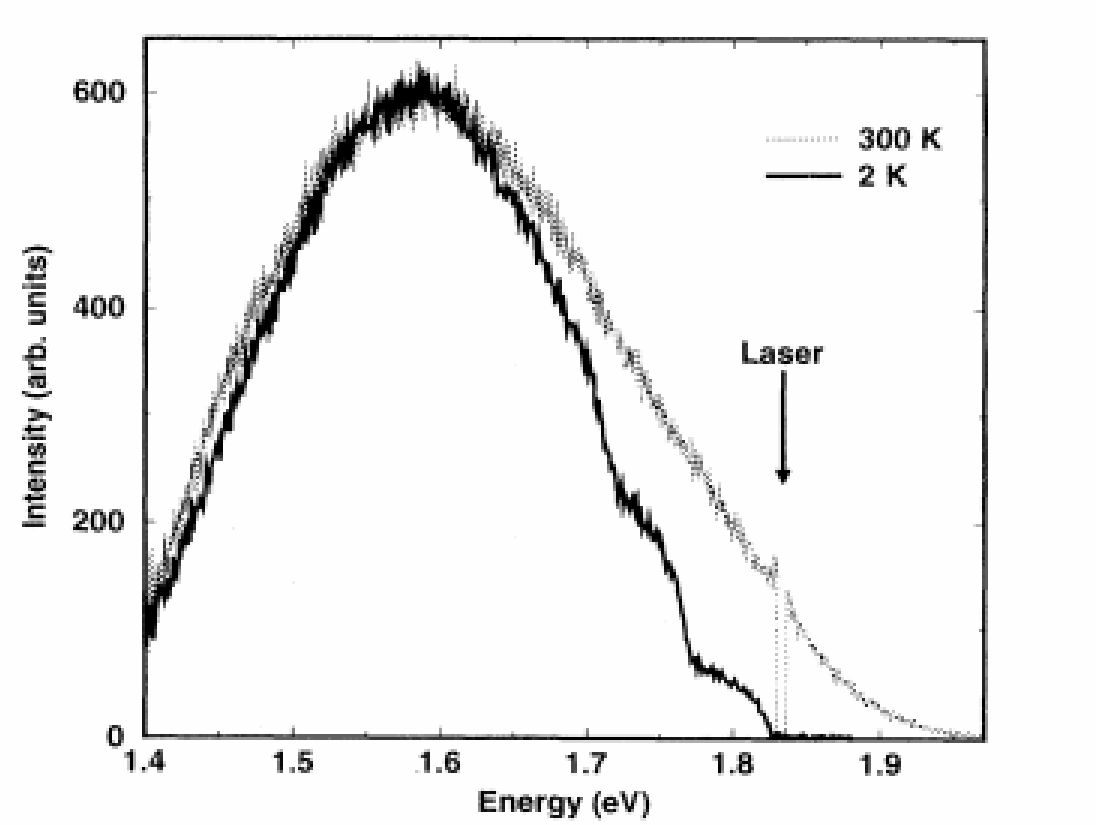

FIGURE 2.3: Luminescence spectra of porous silicon resonantly excited by (1.833 ev) at two different temperatures [92]

Once the refractive index is estimated from experimentally acquired data, the sample dielectric constant and the absorption coefficient can be also calculated. Indeed, both dielectric constant ϵ and absorption coefficient α are correlated to each other. In the case of semiconductor materials, the absorption coefficient is a significant parameter since it indicates the absorption of sample at specific excitation. In most of ultrafast measurements, extracting optical properties of the semiconductors mainly rely on reflectivity and transmission spectrum which can be modulated using different optical models. The simplest modelling approach includes measurements of the reflectance or transmittance at a broad spectral range as shown in Figure.2.4. Figure.2.4 shows the reflectivity of porous silicon (pSi) (solid line) and c-Si (dashed line) at photon energies covering the range from

$2-20eV$ measured using a synchrotron radiation source. Then, the optical parameters of the sample can be extracted using proper method such as Kramers-Kronig (K-K) relations [98]. The relations provide the possibility of extracting the real and imaginary part of the sample dielectric constant.These relations were obtained based on causality and linearity principle which assumes that the absorption of light occurs when light enters the sample [99].

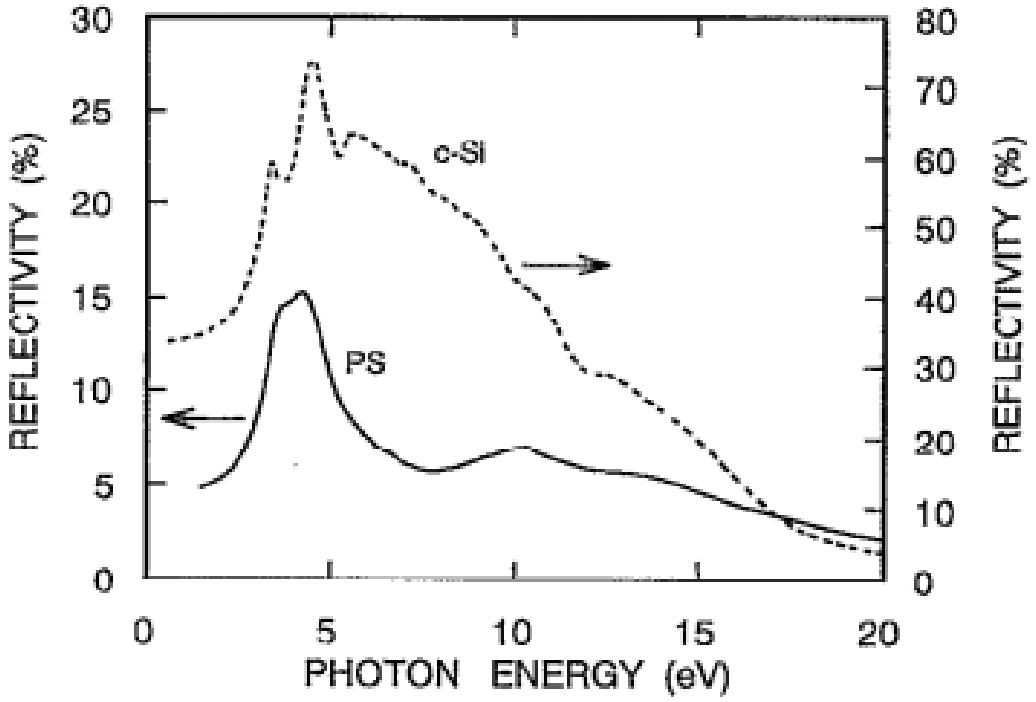

FIGURE 2.4: reflectance spectra of c-Si (dashed line)and Porous silicon (solid line) covering the photon energy range $2-20eV$ measured by a synchrotron radiation source [100].

The relation also provides interconnection between the real ϵ_r and the imaginary parts ϵ_i of the dielectric constant of the media. The K-K relation can be expressed as follows:

$$\varepsilon_r(\omega) = 1 + \frac{2}{\pi} P \int_0^{\infty} \frac{\omega' \varepsilon_i(\omega')}{\omega'^2 - \omega^2} d\omega' \tag{2.1}$$

$$\varepsilon_i(\omega) = -\frac{2\omega}{\pi} P \int_0^{\infty} \frac{\varepsilon_r(\omega') - 1}{\omega'^2 - \omega^2} d\omega' \tag{2.2}$$

Where P represents the integral principal value and ϵ=ϵ_r-i.ϵ_i shows the complex dielectric constant of the media. In order to apply K-K relation, the angular frequency range needs to be taken in the consideration. As it is clear from the equations 2.1 and 2.2 , the angular frequency should cover a wide range of photon energies starting from $2 - 20eV$ to avoid any analyses errors. For shorter photon energy ranges, an extended approach is required to account for undetected reflectance spectra. The drawback of using an extended approach is that it provides different dielectric constant values leading to possibility of bigger chance of errors. In some cases, the reflectance and transmittance measurements shows interference fringes (Fabry−Perot fringes)which can be exploited in evaluation process of the dielectric constant as it is shown in Fig.2.5.

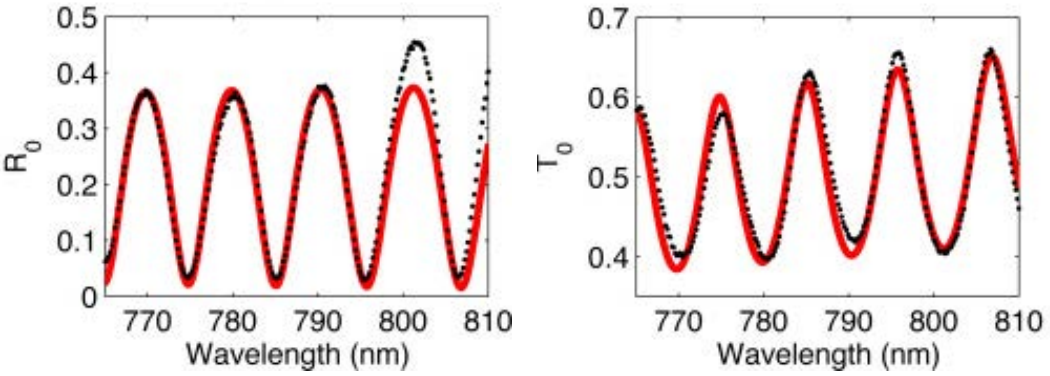

(a) (b)

FIGURE 2.5: (a)Ground state reflection spectra and (b)ground state transmission spectra for 13μm with porosity> 50%; The black doted line represents the expermintal results while the red solid line corresponds to WKB approach fitting [101].

Here, the four terms Forouhi-Bloomer model combined with Bruggeman model were employed to fit the results shown above and extract the real and imaginary parts of the crystalline silicon constituent (c-Si) of the PS membrane as shown in the figure 2.6. The figure also shows the real and imaginary parts of the effective dielectric function of the whole membrane.

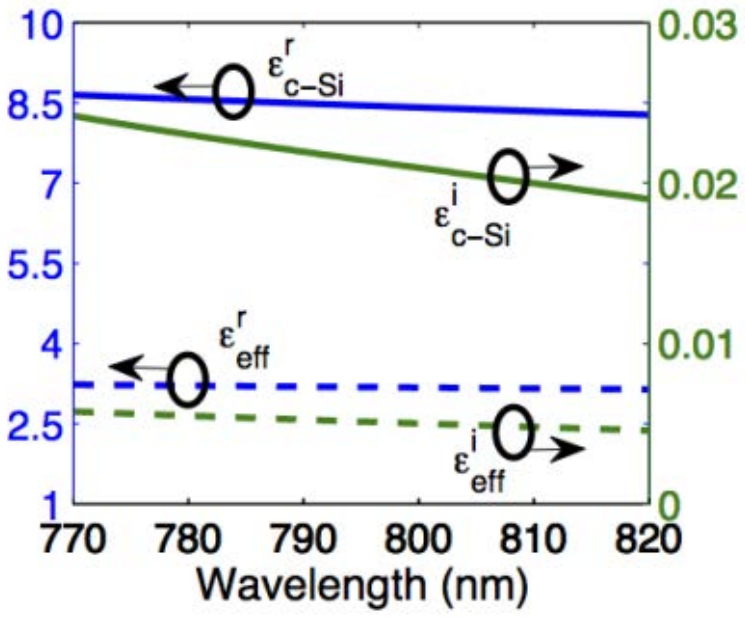

FIGURE 2.6: Real and imaginary parts of the dielectric functions of the crystalline silicon constituent (c-Si) of the PS membrane (solid lines) and the effective medium approximation (dashed lines). The left axis corresponds to the real parts; the right axis corresponds to the imaginary parts, the figure is taken from [102]

On the other hand, the pump-probe technique allows one not only to evaluate the reflection and transmission of unexcited sample but also evaluate and fit the reflection and transmission spectrum under optical excitation as shown in Fig.2.7. The results can be obtained by exciting the electrons within the sample and use another probe signal to detect the transmittance and reflectance changes respectively. The fitting process encompasses use of semi classical models together with effective medium approximations and transfer matrix method. The required parameters can be extracted by adjusting the sample parameters such as thickness, porosity, carrier concentration and the collision time of the carriers to find best fit of the reflectance and transmittance changes [103–105].

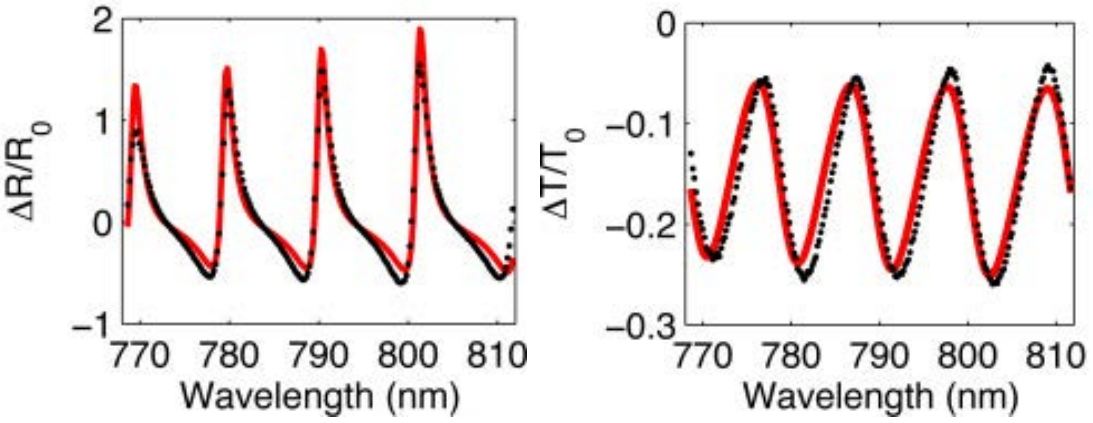

(a) (b)

FIGURE 2.7: (a)Transmittance change and (b)reflectance change for 13μm with porosity$>$ 50% at pump fluence $1.5mJ/cm^2$ and $5ps$ delay time after zero delay between pump and probe signals; The black dotted line represents the expermintal results while the red solid line corresponds to WKB approach fitting [101].

Apart from that, the spectroscopy ellipsometry method, which includes measurement of amplitude ψ and the phase difference Δ between light waves, was widely applied to evaluate the optical properties of porous semiconductors [106]. In the present investigation, the Maxwell-Garnet effective medium approximation was applied to extract the carrier concentration N, dielectric constant ϵ and damping time Γ from reflectance and transmittance spectra. More details about optical model and fitting process will be explained in details in the following chapter.

Figure 2.8 shows a typical absorption coefficient for Bulk silicon , hydrogenated amorphous silicon, p− porous silicon and p+ porous silicon. It can be seen that the absorption coefficient of p− (low doped pSi) increases over the energy range $0.75 - 2.3eV$ while a sharper increase was noticed for p+ (higly doped pSi) particularly at the energies greater than $1.1eV$. On the other hand, hydrogenated amorphous silicon showed one order of magnitude smaller absorption coefficient than that of bulk silicon at energies grater than energy gap of bulk silicon. For porous silicon samples, p− and p+ with same porosity, both samples exhibited different trends with absorption coefficient of p− porous silicon one order of magnitude smaller than that of p+ porous silicon. This indicates that the porous

silicon microstructure depends not only on the sample porosity but also on the doping of the starting substrate [107]. Furthermore, the p− porous silicon indicated significant absorption at energies less than $1.1eV$ and the assigned peak is attributed to some vibrational mode of the surface impurities such as SiH and SiO [108]. The assigned strong absorption for energies lower than energy gap of bulk silicon is striking result since porous silicon is considered as crystalline material at which the transparent behaviour should be predominant. This assigned sub-band gap absorption could be attributed to the presence of tail states (Urbach tail)associated with volume or sample surface.

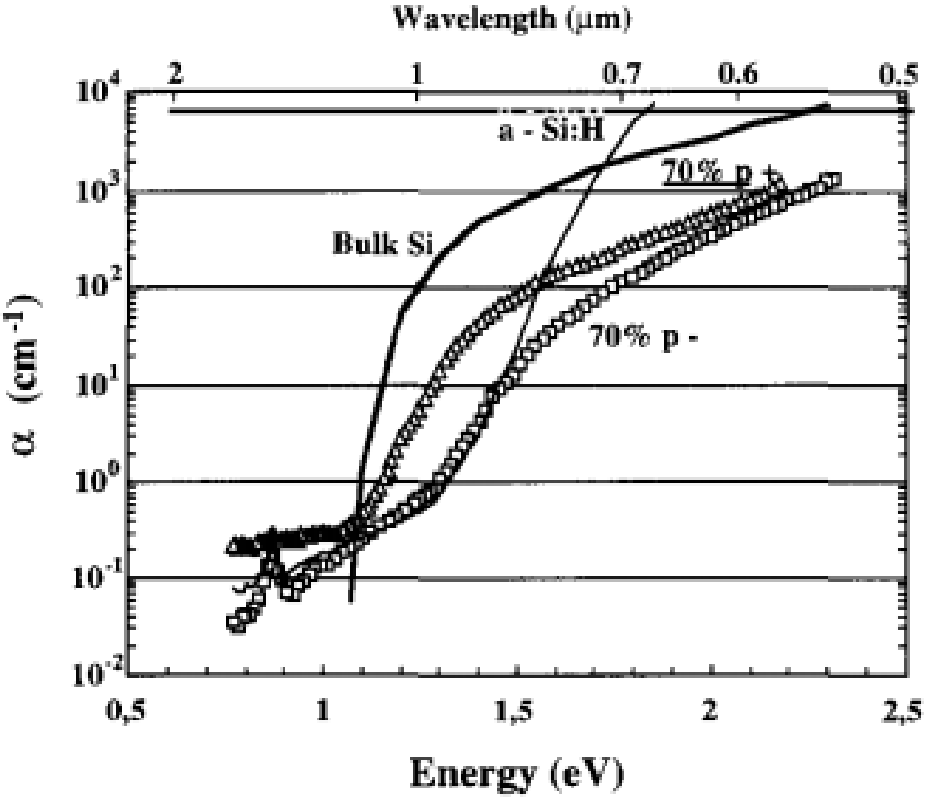

FIGURE 2.8: Optical absorption coefficient as a function of photon energy for bulk silicon, a-Si:H and two p− and p+ porous silicon [107]

Above band gap of bulk silicon, taking the confinement model in the consideration[89, 109], the smooth change of the p− porous silicon can be attributed to the band gap continuum associated with distribution of crystallite size. It is also clearly

seen that the absorption coefficients of the a-Si:H are much higher than that of p− porous silicon for energies above $1.5eV$. For lower photon energies, both a-Si:H and p− porous silicon showed the same absorption coefficients while higher than this observed for p+ porous silicon. The comparison between a-Si:H and porous silicon confirms the tail states similarity for both samples. It is also indicates that the a-Si:H and porous silicon behave differently in the near infrared and visible range at which porous silicon photo-luminescence occurs.

2.4 Summary

In this chapter, the fabrication procedures of the porous silicon structures have been presented. The review also indicated the pores formation and the tunable parameters that contribute in the controlling of pore size and diameter. For the sake of the study, the optical characteristics such as photo-luminescence, reflection and transmission from porous structures are introduced as well. Moreover, the so called (K-K)relation which provides the possibility to extract the real and imaginary parts of porous silicon dielectric function through experimental data is also presented and discussed. The chapter included a comparison between the optical properties such as reflection and absorption coefficient of porous silicon and different silicon morphologies such as bulk and amorphous silicon.

Chapter 3

Experimental Methods and Optical model

3.1 Introduction

This chapter presents information about the laser system used to investigate the carrier dynamics and modulation in nano $npSi$ and micro porous silicon $mpSi$. The chapter also provides experimental details regarding the spectroscopic approaches used in the measurements. The reflection and transmission approaches that can be incorporated in the optical model construction are also explained and discussed. In order to theoretically simulate the reflection and transmission of the samples, the transfer matrix and the Wentzel-Kramers-Brilloun (WKB) methods are introduced and explained in detail for both p- and s- polarised light. The chapter also provides information about the the effective medium approximations and their incorporation into the optical model construction. The contribution of the free carrier absorption to the effective dielectric function of the sample is also discussed.

3.2 Experimental Setup

The field of ultrafast laser spectroscopy was generally based on the Titanium:sapphire (Ti:sapphire) crystal. The crystal possess excellent optical, thermal and mechanical properties. Moreover, they are very efficient due the large band width gain which makes them effective in the field of tunable ultrafast lasers and short pulse generations. It is well known that the efficient down conversion of NIR pulses generated using Ti:sapphire into longer wavelength (far-IR) is a challenge due to high repetition rate of the pulse specified by pulse trip inside the cavity and low pulse power. Recently, this obstacle has been overcome by employing optical parametric oscillators(OPO) [110, 111]. Further spectral extension can be obtained through employing different frequency mixing of the signal and idler or through using multi-stage optical parametric oscillator. Both of these methods are capable of producing low energy pulses. Similarly, long IR pulses can also be generated from the broad band of a mode-locked laser using different frequency mixing [112].

In this study, a Coherent Ti:saphire laser system was employed to generate ultrafast seed pulses through mode locked oscillator Micra. The seed pulses possess $80MHz$ repetition rate with spectral band width centred around $800nm$ and the average power for the generated pulse is around $500mW$, see Figure.3.1. The emerged pulses then guided to the regenerative amplifier for the purpose of stretching, amplification and compressing [113]. In the amplification stage the pulse energy increases allowing wavelength conversion based non-linear processes. In addition, the non-linear process also allows the sample to relax between laser shots by reducing the pulse repetition rate to the desired range.

In the stretching stage, the process involves stretching the time duration of the pulse through linear dispersion induction. The single grating and focal telescope are employed in order to avoid any convergence or divergence of the beam [114]. The purpose of grating is to manipulate the path length of the pulse allowing separation of different pulse wavelengths in such way that makes longer wavelengths experience shorter path lengths. In the stretching stage, the oscillator pulse intensity reduces which in turn yields two advantages: first, it remove all undesired

interaction that occur in the amplification medium and secondly, it avoids any possible damage of the optical components in the amplification stage.

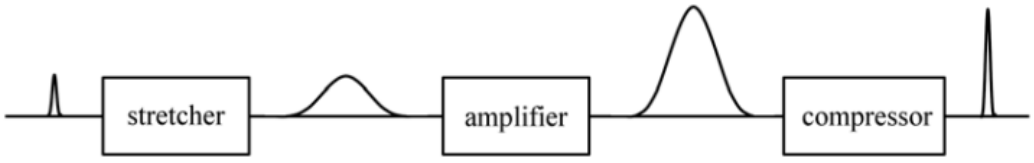

FIGURE 3.1: Simple illustration of the pulse amplification stages [115].

Following the stretching stage, the pulse is amplified using another Ti:sapphire regenerative amplifier. Using a fast and high voltage controlled Pockels cell, the polarisation of the oscillator pulse can be rotated when injecting the pulse inside the cavity. The pulse trapped inside the cavity is amplified and ultimately guided out of the cavity by controlling the voltage applied to the Pockels cell. Applying high voltage on the fast Pockels cell yields polarisation rotation of the trapped pulse to the original orientation allowing its exit outside the cavity. The amplification of the pulse occurs by employing another $527nm$ laser pulses generated using Evolution-15/30 diode pumped intra-cavity doubled, Q- switched Nd:YLF laser. The pulses generated with repetition rate of $1kHz$. Electronic timing provides the ability to synchronise the Pump laser (Nd:YLF) and the trapped pulse inside the cavity, allowing them temporally overlap within the cavity. This resultant pulses much more powerful than those originally generated, however, at this stage the pulses are still stretched in time. To make pulses usable, the induced dispersion resulting from the stretcher and amplification stages should be removed. This can be achieved using a compressor to compensate for the second and third order of the dispersion induced by previous stages.

The compressor stage includes two parallel gratings that disperse the entered beam spectrally providing different path length for each wavelength. Furthermore, the path length of the beam wavelengths can be also adjusted by changing the distance between two gratings in a such way the trailing and leading wavelengths also experience different path lengths. Despite the compensating capability of the

compressor for the second and third order dispersion, the full compensation of higher order dispersions requires more sophisticated devices such as pulse shapers. The pulse shaping process involves removing the higher order dispersions through manipulating the phase of the pulse, full explanation about pulse shaping process can be found elsewhere [116]. The three stages of the amplifier are shown in the Figure. 3.2.

3.2.1 Pump-Probe Reflection and Transmission

To implement optical Pump-mid IR probe measurements, spectral range broadening towards longer wavelengths is required. This can be achieved using an optical parametric amplifier. The wavelength of the pulses from amplifier is centred around $800nm$ with a $1kHz$ repetition rate, $60fs$ time width and an average power of $3.2W$. For the time and spectral measurement of the output pulses, commercial autocollimator spectrometer has been employed, both characteristics are shown in the Figure.3.2. From panel(b)it can be seen that the distribution of the laser pulse profile is Gaussian with spectral range of the excitation.

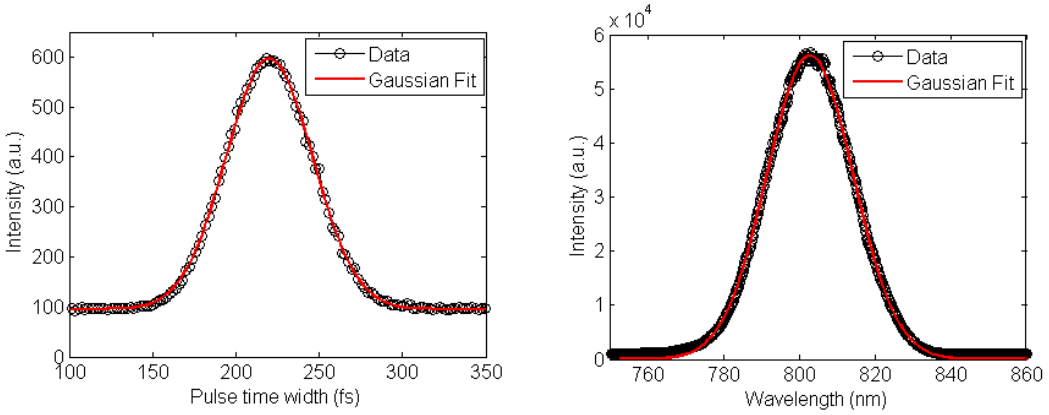

(a) (b)

FIGURE 3.2: distribution profile of the laser pulse(a)Laser time width (b) Spectral distribution of the laser pulse. Here, black circle- dashed line shows the experimental data while the red line shows the Gaussian fit for both figures respectively[102].

The output laser beam is then split into two parts using beamsplitter. The transmitted part (2%) is used as pump pulse while the reflected part (98%) is sent to feed the optical parametric amplifier(OPA). An optical parametric amplifier, capable of producing wavelengths ranging from $3.4\mu m$ to around $9\mu m$, was used in our study. The laser passes through many stages within the optical parametric amplifier including white light continuum generation, white light pre-amplification, power amplification and infrared light generation using DFG crystal. Schematic digram of the various stages within optical parametric amplifier are illustrated in the Figure 3.3. The output mid IR pulses from OPA are used to probe the change in the optical properties of the sample. In order to achieve the desired time delay between the pump and probe signals, a reflector mounted on motorised translation stage was used. The precise distance on the delay stage can be obtained using the relation $c = x/t$, where c represents the velocity of the light, t refers to the delay time between pump and probe in s. Therefore, for a $1fs$ time delay between pump and probe the motorised stage moves a distance of $0.15\mu m$. With careful alignment this technique allows precise measurement of the delay time between pump and probe. The probe beam was vertically polarised while the pump beam is horizontally polarised, as such the contribution of the optical interference can be cancelled out. The power of the pump was controlled using the combination of a half wave plate and polariser.

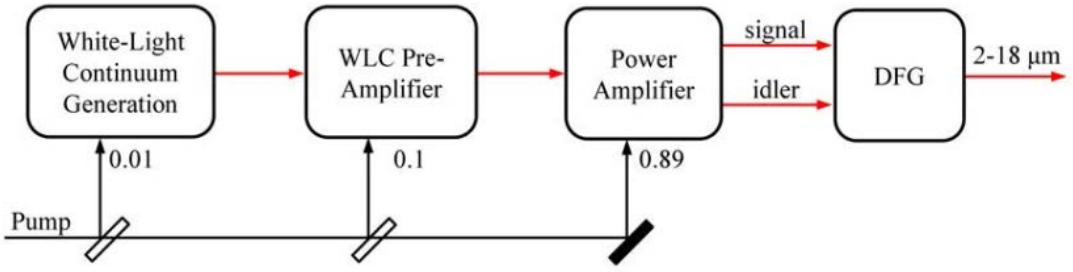

FIGURE 3.3: Schematic illustration of the stages of the optical parametric amplifier. The approximate pump functions associated with each stage are also illustrated [115].

The angle of incidence, with respect to the normal, is fixed at 24^o and 60^o for the pump and probe beams respectively. The sample was mounted on the rotatable

mount providing the possibility of performing pump-probe measurements at different incident angles. For spot size measurements, a slit mounted on one dimensional motorised stage was used. By measuring the intensity of either pump or probe as a function of slit moving distance, the intensity distribution can be obtained from which the spot size can be extracted using Gaussian fit. The schematic representation of the pump-probe setup used in this study is shown in the Figure 3.4. Spot sizes of $620\mu m$ and $200\mu m$ was obtained for the pump and probe respectively. For the detection purpose, two identical Hamamatsu InSb photoconductive detectors were employed.

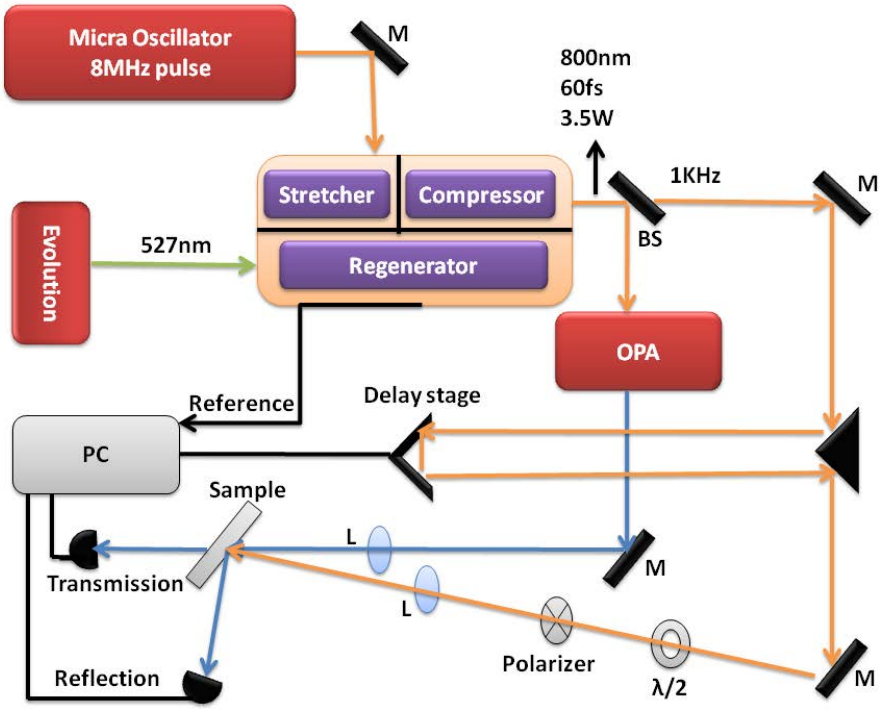

FIGURE 3.4: Schematic representation of the pump-probe setup. The light from the amplifier is divided into two parts representing the pump and probe signals respectively. The computerised reflector mounted on one dimensional translation stage has been employed to obtain the required optical path length between pump and probe signals. Both temporal and spatial overlapping of the pump and probe were obtained on the sample surface during the alignment procedure. All the computerised parts in this setup controlled via LabView software.

The two photoconductive detectors were ultimately connected to two separate lock-in amplifiers for the purpose of small signal amplification and detection. Here,

SR830 DSP lock-in amplifier was used to detect reflected signal while 7265 DSP model is used to detect the transmitted signal. More information about pump probe setup can be found elsewhere [117].

3.3 Reflection and Transmission Principles and Terminologies

When the monochromatic light impinges on the sample, a set of optical parameters can be extracted such as the intensity of the reflection and transmission as well as the intensity of incident light. The intensity ratio between the reflected and incident light is referenced to a sample reflectance, while the intensity ratio between the transmitted and incident light is called the sample transmittance.

3.3.1 Reflection and Transmission at Normal Incidence

The following sections, optical approach of describing the reflection and transmission from the semiconductors. For the sake of simplicity, all measurements are assumed to be at normal incidence which implies that all the cosine terms within Fresnel related coefficients are equal to unity. This assumption also removes the discrimination between s and p polarised waves since at normal incidence the axial symmetry will be verified. For samples without any films or another material deposited on the surface such as bulk silicon the Fresnel formulas can be expressed as follows:

$$r = \frac{N_s - N_i}{N_s + N_i} \tag{3.1}$$

$$t = \frac{2N_i}{N_s + N_i} \tag{3.2}$$

Here, r, t represent the reflection and transmission coefficients and N_s refers to the complex refractive index of the bulk material while N_i represents the complex refractive index of the medium surrounding the bulk. Normally, the measurements are performed in the ambient(air), so the refractive index is taken as $Ni = 1 - i.0$. The sample can also be regarded as a bulk with semi -infinite substrate with the possibility to detect the transmission within the bulk. Although our investigated samples are membranes, the discussion about multilayer systems will be presented in the later sections. Figure 3.5 shows the schematic representation of the reflection and transmission beams at an arbitrary angle of incident. As it can be seen from figure that a part of the incident light is transmitted and another part is reflected with angle equal to the incident angle. The intensity ratio between the reflected and the incident beams is called reflectance R while the intensity ratio between the transmitted and the incident beams is called transmittance T. Therefore reflectance and transmittance can be obtained once the coefficients of the reflection and transmission are acquired.

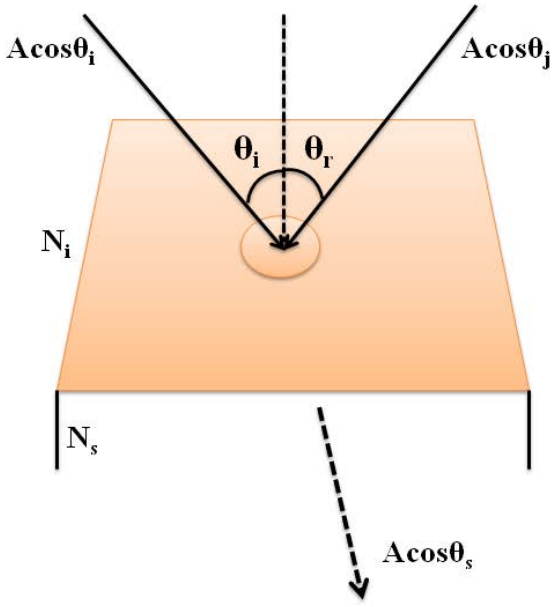

FIGURE 3.5: The reflection and transmission beams at an arbitrary incident angle

Since the mathematical expression of the reflection coefficient is $r = E_r/E_i$. Therefore, taking in the consideration the cross-sectional area of the incident and the reflected beams shown in the Figure 3.5, the reflection coefficient can be related to the reflectance R as follows:

$$R = \frac{I_r.A\cos\theta_r}{I_i.A\cos\theta_i} = \frac{I_r}{I_i} = \left|\frac{E_r}{E_i}\right|^2 = |r|^2 \tag{3.3}$$

Here, the angle of the incident beam is assumed to be equal to reflected beam for the sake of calculation simplicity. Similarly, the transmittance T is also obtained through the ratio between the incident and transmitted beams. However, the mathematical expression for the transmittance is different since the refractive index of substrate should be taken into account, hence $I_t \propto n_s.|E_t|^2$ where $N_s = n_s - i.k_s$[118, 119]. Thus, the transmittance is related to the transmission coefficient through:

$$T = \frac{n_s.E_t^2.A\cos\theta_s}{n_i.E_i^2.A\cos\theta_i} = \left(\frac{n_s\cos\theta_s}{n_i\cos\theta_i}\right).|t|^2 \tag{3.4}$$

As we mentioned above, at normal incidence, the polarisation of reflected and transmitted beams are same for either s-polarisation or p-polarised waves. As a result, reflectance and transmittance relations would be expressed as follows:

$$R = R_s = R_p = (\frac{N_s - N_i}{N_s + N_i})^2 \tag{3.5}$$

$$T = T_s = T_p = \frac{4n_sn_i}{(N_s + N_i)^2} \tag{3.6}$$

Once the reflectance and transmittance are measured, valuable information regarding the real and imaginary parts of the refractive index of the bulk material can be obtained. It should be noted that mounting the detector within the bulk material is complicated in the case of transmission measurements. It should also be mentioned that all the materials are assumed to possess isotropic structure.

Usually, slab like structure is used to extract some important optical parameters such as the complex refractive index of the sample. The analytical expression proposed by Enrico Nichelatti [120] was previously used to obtain the complex refractive index N_s for a planar slab from the reflectance and transmittance at normal incidence angle as illustrated in the equations below:

$$\begin{aligned} R_F &= \frac{\sqrt{2+T^2-(1-R)^2-[2+T^2-(1-R)^2]^2-4R(2-R)}}{[2(2-R)]} \\ k(R,T) &= \frac{\lambda}{4\pi h}\ln[\frac{R_F(R,T)T}{R-R_F(R,T)}] \\ n_{\pm}(R,T) &= \frac{1+R_F(R,T)}{1-R_F(R,T)} \pm \left\{\frac{4R_F(R,T)}{[1-R_F(R,T)]^2} - (\frac{\lambda}{4\pi h})^2 \ln^2[\frac{R_F(R,T)T}{R-R_F(R,T)}]\right\}^{1/2} \end{aligned} \tag{3.7}$$

Here, λ refers to the wavelength of the incident light and h is the sample thickness. This demonstrated that once the reflectance and transmittance are measured, the real and imaginary parts of the complex refractive index of the sample can be obtained. From the equations above, the term R_F is first obtained from the measured reflection and transmission (R,T).

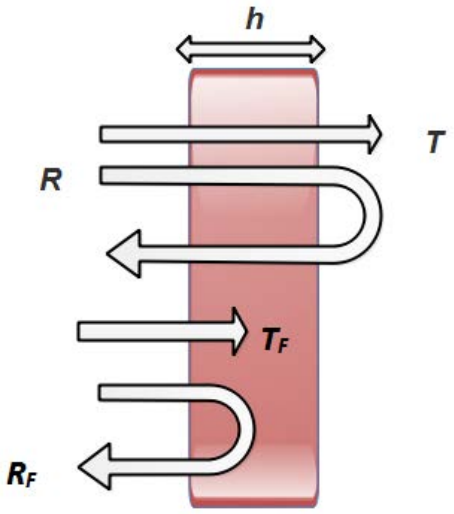

FIGURE 3.6: A slab with partial absorption and plan parallel faces, where h refers to the slab thickness; Overall coefficients of the reflectance and transmittance are represented by (R,T) while the single face reflectance and transmittance coefficients are referred to as (R_F,T_F)

[120].

The real and imaginary expressions can then be employed to calculate the complex refractive index of the sample. There are two possible solutions to the equations, the proper solution can be chosen by consideration of the condition ($k_s \ll n_s, n_s > 1$). Khashan [121] and Stezel [122] proposed the equations 3.7 to determine the optical constant of the of a planar slab from reflection and transmission at normal incidence. It can be concluded that the analytical expressions illustrated above are regarded as valuable method to determine the optical constant of the material. In addition to above mentioned method, the slab can be modelled as multilayer regime as (air/slab/air) providing the possibility to use multilayer analytical method such as transfer matrix method to calculate (R, T) of the sample. The transfer matrix method will also be discussed in detail in the later sections.

For thick samples, obtaining the optical constant based on the reflectance and transmittance is often unreliable since the transmittance is small undetectable due to sample absorption. In this case, the optical constant can not be obtained as extracting two optical parameters n_s, k_s using single measurement is not valid. As discussed before, this method relies on a nearly normal incidence. Therefore, finding a way of obtaining the optical parameters of different sample structures, with no restriction and special assumption, is of considerable interest.

3.3.2 Reflection and Transmission at any angle of incidence

In order to understand the reflection and transmission of any sample structure, various sample parameters need to be taken in to consideration such as the polarisation of the light, sample layers, refractive index e.t.c. For the sake of the simplicity, the sample is assumed to be attached to the semi-infinite substrate. Figure.3.7 shows schematic representation of an incident electric E_i of an electromagnetic wave. The E_{is} and E_{ip} symbols indicated in the figure correspond to the vertical and parallel components with respect to the plane of the incidence. Similarly, the polarisation components for the reflected and transmitted light are

indicated as (E_{rs}, E_{rp}) and (E_{ts}, E_{tp}) corresponding to $s-$ and $p-$ polarisation components of the electric field respectively. The complex refractive index for the ambient media and substrate region are expressed as N_0 and N_s respectively. To proceed with this, continuity of the of tangential electric and magnetic components across the boundary is required [123, 124]. The tangential components on the incident and transmitted sides are equal. As a result, the polarisation dependence of the Fresnel formulas for the reflection and transmission coefficients can be extracted as follows:

$$r_s = \frac{E_{rs}}{E_{is}} = \frac{N_0 \cos\theta_i - N_s \cos\theta_t}{N_0 \cos\theta_i + N_s \cos\theta_t} \tag{3.8}$$

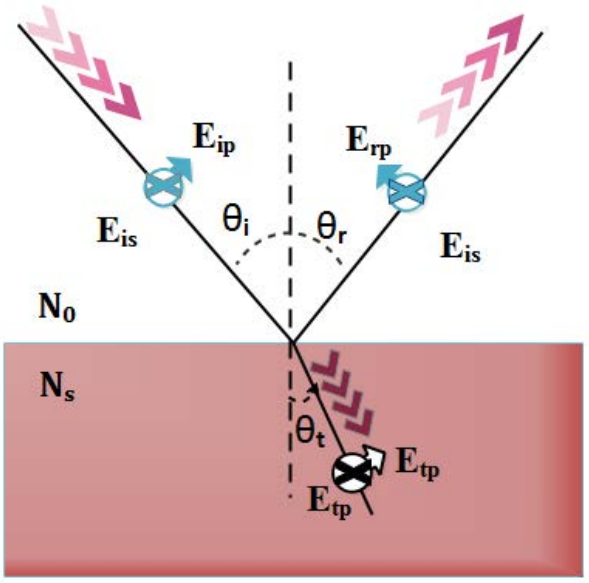

FIGURE 3.7: The two polarisation components of an electric field. The subscripts s- and p- refer to electric field components perpendicular and parallel to the plane of the incident light while N_0 and N_s refer to the complex refractive indices of the ambient media and the substrate respectively.

$$r_p = \frac{E_{rp}}{E_{ip}} = \frac{N_s \cos\theta_i - N_0 \cos\theta_t}{N_s \cos\theta_i + N_0 \cos\theta_t} \tag{3.9}$$

$$t_s = \frac{E_{ts}}{E_{is}} = \frac{2N_0 \cos\theta_i}{N_0 \cos\theta_i + N_s \cos\theta_t} \tag{3.10}$$

$$t_p = \frac{E_{tp}}{E_{ip}} = \frac{2N_0 \cos\theta_i}{N_s \cos\theta_i + N_0 \cos\theta_t} \tag{3.11}$$

Here, these formulas are simplified considering that the reflection angle θ_r is equal to the incident angle θ_i. The above equations can be further simplified based on the Snell's law such that they include only the contribution of the refractive indices (N_0,N_s) and the angle of incidence θ_i. The above reformulation procedure is a unique case of the ambient/ substrate regime. Thus, the ultimate reflection coefficients for s- and p- polarised lights can be expressed as follows:

$$r_s = \frac{\cos\theta_i - (N_{s0}^2 - \sin\theta_i^2)^{1/2}}{\cos\theta_i + (N_{s0}^2 - \sin\theta_i^2)^{1/2}} \tag{3.12}$$

$$r_p = \frac{N_{s0}^2 \cos\theta_i - (N_{s0}^2 - \sin\theta_i^2)^{1/2}}{N_{s0}^2 \cos\theta_i + (N_{so}^2 - \sin\theta_i^2)^{1/2}} \tag{3.13}$$

Here, $N_{s0} = N_s/N_0$. As we mentioned in the previous sections, the ratio between the reflected and the incident intensities is the reflectance while the ratio between the transmitted and the incident light is the transmittance. Therefore, the expression of the reflectance and transmittance can be expressed as follows:

$$R_s = |r_s|^2 \qquad R_p = |r_p|^2 \tag{3.14}$$

$$T_s = \frac{N_s \cos\theta_t}{N_0 \cos\theta_i}.|t_s|^2 \qquad T_p = \frac{N_s \cos\theta_t}{N_0 \cos\theta_i}.|t_p|^2 \tag{3.15}$$

Therefore, the reflection and transmission coefficients are both complex numbers if the refractive index of the substrate is taken as a complex number. Thus, it is more convenient to reproduce Fresnel coefficients in the polar coordinate system.

3.3.3 Transfer Matrix Method

In the previous section, the Fresnel equations convenient for dealing with basic ambient/ substrate regime have been discussed. In fact, such optical regimes are rarely available in practise. In general, Fresnel equations are used to account for reflection and transmission with single interface. Thus, creation of an optical model capable of dealing with various sample structures such as slab, thin films with substrate and multi layered systems is necessary. In order to achieve that, detail understanding of the thin film slab with substrate is required. Generally, the term substrate is used when the wavelength of the incident light is much smaller compared to the material thickness and when such material is relatively absorptive. In this case, the resulting structure is coined as substrate without taking into account the rear interface of the medium. In these limits, the Fresnel equations are convenient to describe and extract all the required optical parameters of the sample since the sample (ambient/substrate) is considered as a thick and highly absorbing medium. This can be achieved using proper simulation of the experimental results as shown in the Figure 3.7.

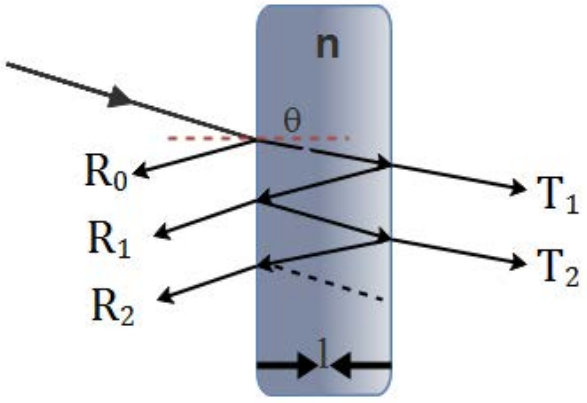

FIGURE 3.8: The light interference, reflection and transmission of the two interfaces of the sample.

In the case of slab samples where the thickness is not large and the incident light is not completely absorbed, there is a possibility of detecting the transmitted light

from the rear interface of the slab as it is illustrated in the Figure 3.8. It should be noted here that the possibility of obtaining optical parameters such as optical constants have been discussed in many reports [120, 122, 125–127]. In the case of single interface between two mediums, The collection of Fresnel equations from 3.8 to 3.11 can be used to describe the reflection and transmission respectively. However, for samples with more than one interface, the situation is different since the contributions of the front and rear surface of the sample should be taken into account when measuring the reflection and transmission intensities as it is illustrated in the Figure 3.8.

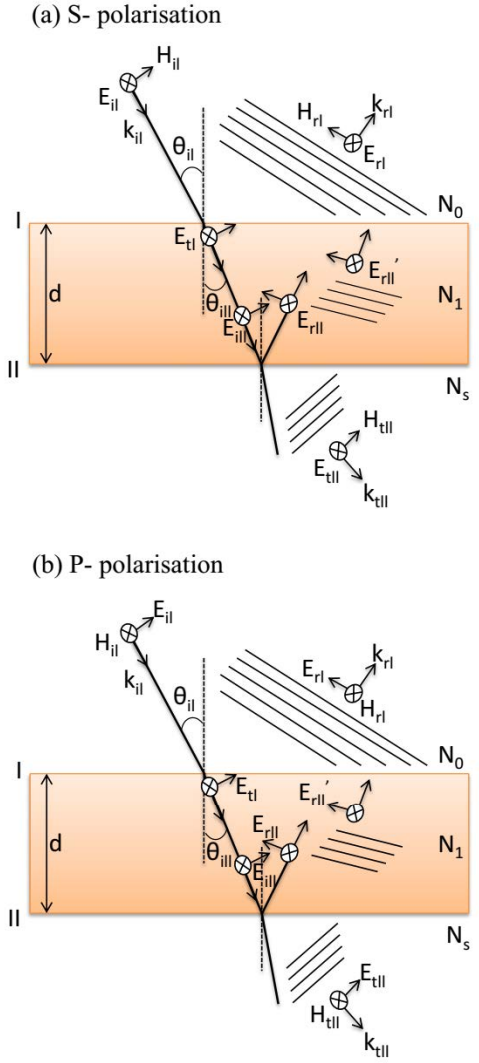

FIGURE 3.9: The the transfer matrix method for ambient/slab/ambient structure for (a)s- polarised light and (b)p- polarised light.

The superposition of the waves between the two interfaces can lead to the observed interference in the reflection and transmission spectra respectively. These interferences can be attributed to the path length difference as well as the wavelength of the incident light at which the constructive and destructive interference of the reflection and transmission occurs. The summation of the infinite number of the reflections transmissions yields the overall reflection and transmission of the slab is hard to calculate. In order to overcome this, the slab can be treated as an optical system with an ambient on film on substrate structure, this is schematically illustrated in the Figure 3.9. In the case of free standing slab in the air, the substrate is considered as air and the slab is modelled as air/slab/air. The basic analyses method is based on the optical system mentioned above and then extended to include more complicated systems. Despite the possibility of improving the Fresnel equations to include complicated systems or even multi-layered systems, the calculation and the method is still hard and complicated. However,by employing the transfer matrix method this can be overcome [96, 128–131]. In this approach, each transfer matrix is associated with optical properties of a single interface allowing complicated systems to be resolved. Further details of this method will be discussed in future sections.

For the simplicity, we will consider an optical system with air/slab/air arrangement as it shown in the Figure.3.8 and treat it mathematically for both s- and p- polarisations respectively. An example of using such approach can be seen in section 3.5.1.

3.3.3.1 Transfer Matrix Method Mathematical treatment

The transfer matrix method is a mathematical approach employed to solve the propagation of the electromagnetic waves across the boundaries or multi-layered structures[119]. It should be noted here that this method is also exploited in the design and fabrication of anti-reflective coatings as well as dielectric materials [118]. The mathematical derivation of this approach is based on the Maxwell equations. Figure 3.9 shows the incidence of the linearly polarised light on free

standing thin dielectric film in the air. The overall structure corresponds to the ambient/ thin film/ substrate. Such kind of regimes might resemble the deposition of a fraction of wavelength thick layer on the surface of a mirror, lens or prism. At the outset of the mathematical treatment, the most important issue that needs to be clarified is that each wave components such as E_{rI}, E'_{rII}, E_{tII} and so forth, represent the overall waves travelling in that direction within medium, see figure 3.9. Therefore, the summation of all the processes is built based on that. Here, the boundary condition that states that all electric and magnetic tangential are continues across the boundaries should be taken in the consideration. In another words, the tangential components should be equal on the both sides of the sample. Here, the mathematical treatment for the p- polarised light shown in the Figure 3.8. at the first boundary (I) are expressed as follows:

$$E_I = E_{iI} \cdot \cos\theta_{iI} - E_{rI} \cdot \cos\theta_{iI} = E_{tI} \cdot \cos\theta_{iII} - E'_{rII} \cdot \cos\theta_{iII} \tag{3.16}$$

and

$$H_I = \sqrt{\frac{\epsilon_0}{\mu_0}} \cdot N_0 \cdot (E_{iI} + E_{rI}) = \sqrt{\frac{\epsilon_0}{\mu_0}} \cdot N_1 \cdot (E_{tI} + E'_{rII}) \tag{3.17}$$

The relation between the electric and magnetics components can be obtained based on the fact that in non-magnetic media, both components are related to each other through the unit propagation vector and the refractive index.

$$H = \sqrt{\frac{\epsilon_0}{\mu_0}} N \cdot \hat{k} \times E \tag{3.18}$$

at the second boundary II

$$E_{11} = E_{iII} \cdot \cos\theta_{iII} - E_{rII} \cdot \cos\theta_{iII} = E_{tII} \cdot \cos\theta_{tII} \tag{3.19}$$

$$H_{II} = \sqrt{\frac{\epsilon_0}{\mu_0}} \cdot N_1 \cdot (E_{iII} + E_{rII}) = \sqrt{\frac{\epsilon_0}{\mu_0}} \cdot N_s \cdot E_{tII} \tag{3.20}$$

Where N_s represents the complex refractive index of the substrate. According to the fact that the wave traversing the film experiences phase shift about $k_0(2N_1 d\cos\theta_{iII})/2$. The resulted phase shift is represented as $k_0 h$ and expressed as follows:

$$k_0 h = k_0 \frac{2N_1 d \cdot \cos\theta_{iII}}{2} \tag{3.21}$$

Here, k_0, d, N_1 and θ_{iII} represent the vacuum wave number $k_0 = 2\pi/\lambda$, the sample thickness, the film refractive index and the angle inside the film respectively. So, the reformulated equations are expressed as follows:

$$E_{iII} = E_{tI} \cdot e^{-ik_0 h} \tag{3.22}$$

$$E_{rII} = E'_{rII} \cdot e^{ik_0 h} \tag{3.23}$$

Based on the equations 3.21 and 3.22 the equations 3.19 and 3.20 can be reformulated as follows:

$$E_{II} = \cos\theta_{iII} \cdot (E_{tI} \cdot e^{ik_0 h} - E'_{rII} \cdot e^{-ik_0 h}) \tag{3.24}$$

Similarly, the magnetic components can be reproduced as follows:

$$H_{II} = \sqrt{\frac{\epsilon_0}{\mu_0}} \cdot N_1 \cdot (E_{tI} \cdot e^{-ik_0 h} + E'_{rII} \cdot e^{ik_0 h}) \tag{3.25}$$

the above two equations can be expressed in terms of E_{tI} and E'_{rII} yielding:

$$E_{tI} = \frac{1}{2} \cdot e^{ik_0 h}\left(\frac{E_{II}}{\cos\theta_{iII}} + \frac{H_{II}}{\sqrt{\frac{\epsilon_0}{\mu_0}} \cdot N_1}\right) \tag{3.26}$$

$$E'_{rII} = \frac{1}{2} \cdot e^{-ik_0 h}\left(\frac{H_{II}}{\sqrt{\frac{\epsilon_0}{\mu_0}} \cdot N_1} - \frac{E_{II}}{\cos\theta_{iII}}\right) \tag{3.27}$$

Then the last two equations are substituted into the equations 3.16 and 3.17 to obtain E_1 and H_I at the boundary I:

$$E_I = E_{II} \cdot \cos k_0 h + \frac{H_{II} \cdot \cos\theta_{iII}}{\sqrt{\frac{\epsilon_0}{\mu_0}} \cdot N_1} \cdot i \sin k_0 h \tag{3.28}$$

$$H_I = E_{II} \cdot \frac{\sqrt{\frac{\epsilon_0}{\mu_0}} \cdot N_1}{\cos\theta_{iII}} \cdot i \sin k_0 h + H_{II} \cdot \cos k_0 h \tag{3.29}$$

and the term Y_1 is introduced to be:

$$Y_1 = \sqrt{\frac{\epsilon_0}{\mu_0}} \cdot \frac{N_1}{\cos\theta_{iII}} \tag{3.30}$$

For the s- polarised light shown in Figure.3.9(a), where E is perpendicular to the plan of incidence, the resulted equations resemble that obtained in the reference[118]. provided that the Y_1 should be substituted as:

$$Y_1 = \sqrt{\frac{\epsilon_0}{\mu_0}} \cdot N_1 \cdot \cos\theta_{iII} \tag{3.31}$$

For p-polarised waves, the above relations can be expressed in the matrix notation:

$$\begin{bmatrix} E_I \\ H_I \end{bmatrix} = \begin{bmatrix} \cos k_0 h & (i \sin k_0 h)/Y_1 \\ Y_1 \sin k_0 h & \cos k_0 h \end{bmatrix} \cdot \begin{bmatrix} E_{II} \\ H_{II} \end{bmatrix} \tag{3.32}$$

or

$$\begin{bmatrix} E_I \\ H_I \end{bmatrix} = M_I \cdot \begin{bmatrix} E_{II} \\ H_{II} \end{bmatrix} \tag{3.33}$$

Here, the characteristic matrix M_I links the fields of the two adjacent interfaces or boundaries. Thus, in the case of two layer deposition on substrate, the over all interfaces or boundaries will be three and the structure of the matrix notation will take the form:

$$\begin{bmatrix} E_{II} \\ H_{II} \end{bmatrix} = M_{II} \begin{bmatrix} E_{III} \\ H_{III} \end{bmatrix} \tag{3.34}$$

The characteristic Matrix M_{II} relates the boundaries II and III respectively. Similarly, the connection between the boundaries I and III can be achieved through multiplying the above matrix by the characteristic matrix M_I as given below:

$$\begin{bmatrix} E_I \\ H_I \end{bmatrix} = M_I \cdot M_{II} \begin{bmatrix} E_{III} \\ H_{III} \end{bmatrix} \tag{3.35}$$

The matrix notation can be generalized to include multi-layered films deposited on the substrate with the specific thickness and complex refractive index for each layer. Considering the number of layers is p, the resultant relation between the first and the last boundary will be introduced as follows:

$$\begin{bmatrix} E_I \\ H_I \end{bmatrix} = M_I \cdot M_{II} ... M_p \begin{bmatrix} E_{(p+1)} \\ H_{(p+1)} \end{bmatrix} \tag{3.36}$$

Here, the proper sequence product of the individual 2×2 matrices yields the characteristic matrix of the entire system, that is:

$$M = M_I \cdot M_{II} ... M_p = \begin{bmatrix} m_{11} & m_{12} \\ m_{21} & m_{22} \end{bmatrix} \tag{3.37}$$

Based on the above scheme, The interconnection between the measurements and the reflection and transmission coefficients can be obtained in the frame of the boundary condition 3.16, 3.17, 3,19 and 3.20 by substituting:

$$Y_0 = \sqrt{\frac{\epsilon_0}{\mu_0}} \cdot \frac{N_0}{\cos\theta_{tII}}$$

$$Y_s = \sqrt{\frac{\epsilon_0}{\mu_0}} \cdot \frac{N_s}{\cos\theta_{tII}}$$

and

$$w = \frac{\cos\theta_{iI}}{\cos\theta_{tII}}$$

In order to relate the refractive and incident angles, Snell's law can be employed and the equation 3.33 can be reformulated to:

$$\begin{aligned} w \cdot (1 - r) &= m_{11} \cdot t + m_{12} \cdot t \cdot Y_s \\ Y_0 \cdot (1 + r) &= m_{21} \cdot t + m_{22} \cdot t \cdot Y_s \end{aligned} \tag{3.38}$$

By employing the definition of reflection and transmission shown in the following equations:

$$r = \frac{E_{rI}}{E_{iI}} \quad t = \frac{E_{tII}}{E_{iI}} \tag{3.39}$$

The reflection and transmission coefficients for the p-polarised waves will take the form of:

$$r_p = \frac{w(m_{21} + m_{22}Y_s) - Y_0(m_{11} + m_{12}Y_s)}{w(m_{21} + m_{22}Y_s) + Y_0(m_{11} + m_{12}Y_s)} \tag{3.40}$$

$$t_p = \frac{2Y_0 w}{Y_0(m_{11} + m_{12}Y_s) + w(m_{21} + m_{22}Y_s)} \tag{3.41}$$

Similarly, the same procedure can be applied to obtain the reflection and transmission coefficients for the s-polarised light with some modification in Y_0 and Y_s forms as is shown in the following equations:

$$r_s = \frac{Y_0 m_{11} + Y_0 Y_s m_{m12} - m_{21} - Y_s m_{22}}{Y_0 m_{11} + Y_0 Y_s m_{12} + m_{21} + Y_s m_{22}} \tag{3.42}$$

$$t_s = \frac{2Y_0}{Y_0 m_{11} + Y_0 Y_s m_{12} + m_{21} + Y_s m_{22}} \tag{3.43}$$

Here

$$\begin{aligned} Y_0 &= \sqrt{\tfrac{\epsilon_0}{\mu_0}} \cdot N_0 \cdot \cos\theta_{iI} \\ Y_s &= \sqrt{\tfrac{\epsilon_0}{\mu_0}} \cdot N_s \cdot \cos\theta_{tII} \end{aligned} \tag{3.44}$$

The above calculations can be employed to calculate polarisation dependence reflection and transmission for any film configuration.In the case of multilayer film, the corresponding matrix for each layer in the film is computed first followed by proper sequence multiplication of each layer matrix. The resulted characteristic matrix can be then substituted in the above relations to calculate the reflection and transmission.

3.3.3.2 Illustration Example

In the previous section, we illustrated the possibility of using transfer matrix method to obtain the reflection and transmission coefficients. Based on that, the equation 3.14 and 3.15 can be employed to calculate reflectance and transmittance

respectively. For the purpose of evaluating the transfer matrix method, the simple ambient/substrate structure of the thick crystalline silicon (C-Si) is assumed. This simple structure is regarded as a sample with two parallel boundaries surrounded with air, as is illustrated in the previous section. Despite the fact that this method has been applied to multilayer structures, it can also be used for the ambient/ substrate configuration. This can be achieved by regarding the sample as an ambient/film/substrate with a film thickness equal to zero. Thus, the resulting configuration can be regarded as ambient/ substrate regime. In this case, the resulting regime would return to the Fresnel configuration used to calculate the reflection and transmission coefficients. Alternatively, the crystalline silicon(C-Si) sample can be assumed to have air/C-Si/air configuration. In this section, the example is introduced relying on the second configuration to obtain the reflectance, transmittance and the absorption coefficient of the sample by applying the transfer matrix method.

The most critical parameter in this calculation is the complex refractive index of the crystalline silicon(C-Si) which has been found to be $N_{c-si} = 3.673 - i.0.005$ at $800nm$ according to Aspnes and Studna [77]. As long as the complex refractive is provided, the transfer matrix method can be applied to calculate the optical properties of this configuration. The imaginary part of the complex refractive index represents the extinction coefficients ($k = 0.005$) at $800nm$ from which the absorption coefficient α can be obtained according to $\alpha = 4\pi k/\lambda = 7.854 \times 10^2 cm^{-1}$. According to the Beer's law $I_t = I_0.e^{-\alpha d}$, the penetration depth is related to the absorption coefficient through $\alpha d_p = 1$ when $I_t/I_o = 1/e \sim 37\%$ and its value is equal to $d_p = 1/\alpha = 13\mu m$. Here, the thickness of the crystalline silicon is taken to be $100\mu m$ which significantly bigger than penetration depth of $800nm$. Based on the sample thickness and complex refractive index, the characteristic matrix for C-Si sample can be obtained from which the optical properties can be extracted. Then, employing the equations 3.40-3.43, the reflection and transmission coefficients for both s- and p- polarized waves can be calculated respectively.

Figure 3.10 shows the reflectance, transmittance and the absorption coefficient for $100\mu m$ thick crystalline silicon(C-Si) as a function of incident angle θ_{iI} ranging

from 0^o to 90^o. Here, R_s, R_p and R_n correspond to the reflectance of the s, p and unpolarized waves respectively as shown in the Figure 3.10(a). It can be seen that the $s-$ polarized reflectance gradually increases with increasing the angle of incidence this reaches maximum around 90^o. For the $p-$ polarized light the reflectance first decreases, reaching the minimum value around the Brewster angle θ_B . Following that the p polarized reflectance dramatically increases and peaks at the end of the incident angle range. The reflectance of unpolarized light is different from that of the $s-$ and $p-$ polarized light, the reflectance steadily decreases and reaches the minimum around Brewster angle θ_B followed by dramatic increase towards the end of the incident angle range.

Figure 3.10(b) shows the transmittance change as a function of incident angle for $s-$, $p-$ and unpolarized waves. It can be seen from the figure the transmittance trend resembles the opposite orientation of the reflected waves. However, the amplitude is not comparable since the transmittance is much smaller (on the order of 10^{-4}) comparing to the reflectance seen from the Figure 3.10(a). This implies that the detection of transmission signal will be significantly harder. In this case the $100\mu m$ thick C-Si can be considered as a substrate and the front surface optical calculation can be easily obtained using Fresnel equations. It should be mentioned here that the absorbance A of the C-Si can be also calculated from the reflectance and transmittance according to the energy conservation principle.

$$A + R + T = 1$$

Moreover, the absorption coefficient can be also extracted using the equation $A = \alpha.l$ for the $s-$, $p-$ and unpolarized wave respectively, where l is the sample thickness, as it is shown in the Figure 3.10(c). The reduction in $p-$ polarized light around the Brewster angle $\theta_B$can be explained in the frame of electric dipole oscillation at which the reflected light disappears when the oscillating direction of the electric dipole is perpendicular to the reflection vibrational direction. However, for the mediums with $k > 0$, where k is the imaginary part of the refractive index ($N = n - ik$), the $p-$ polarized reflection around Brewster angle θ_B will not be

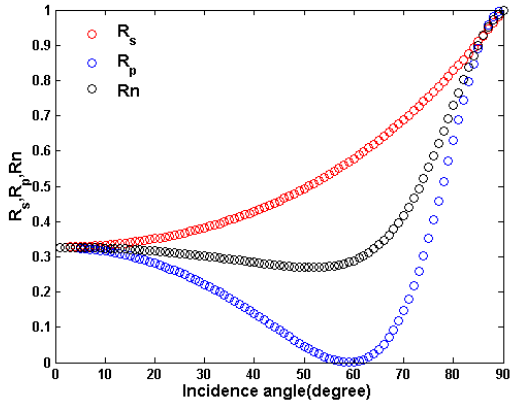

(a)

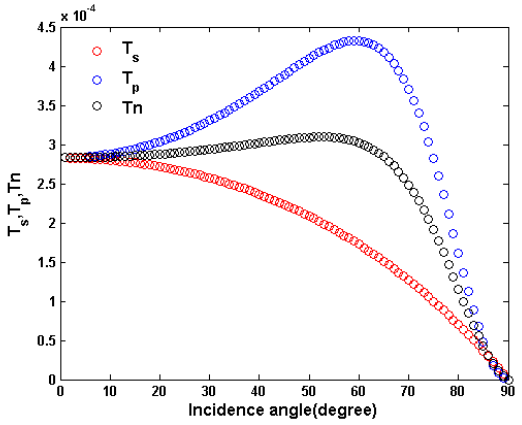

(b)

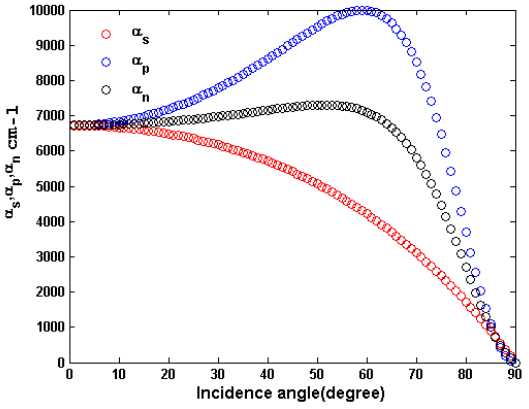

(c)

FIGURE 3.10: Angular dependence (a)Reflectance (b)Transmittance and (c)absorption coefficient for $100\mu m$ thick crystalline silicon (C-Si) for $s-$, $p-$ and unpolarized light respectively.

completely suppressed to zero. It should be also noted that the Brewster angle θ_B changes from one semiconductor to another based on the dielectric constant.

3.3.4 Non-uniform model

This model is basically based on the(WKB)approximation. This approximation, usually associated with the names of Wentzel, Kramer.s, Brillouin, and Jeffreys, is sometimes also known as the phase-integral method. A general discussion of the method together with a critical guide to the related literature can be found in the book by [132]. In optical waveguide theory the method has wide application, although the relevant results are usually able to be obtained by the ray optics approach. These methods are also similar in their range of applicability, both being suitable for use only when the variation of dielectric permittivity is small in distances of the order of the wavelength. However, there are cases where the ray theory may provide a better level of approximation than the usual WKB theory. As we shall see, these anomalies result from problems associated with the phase changes occurring on reflection from a dielectric discontinuity. If these phase changes are correctly accounted for, then the first-order WKB and ray methods yield identical results [133]. In this approximation a smooth nonuniform change of the dielectric properties as a function of depth is assumed [134]. In our case, the change is related to the alteration of the desity of the excited charge carriers as a function of the membrane depth along the coordinate z. Thus, the membrane dielectric function can be expressed as $\epsilon_{membrane}(z) = \epsilon_{si} + \Delta\epsilon_{fcr}(z)$. This expression can be incorporated into Maxwell Garnett and Bruggeman model to extract the effective dielectric function of the sample as well as allow the simulation of the reflection and transmission coefficients under the excitation condition. From simulation, the free carrier contribution $\Delta\epsilon_{fcr}$ to the effective dielectric function can be extracted. It should be mentioned here that the nontrivial oscillation of the diffusively scatterd light is also expected as a function of incident angle. However, this study mainly deals with specular reflection and transmission which is

described well by a model with dielectric function depending only on the perpendicular coordinate [101].

3.3.4.1 Characteristic matrix definition

In order to calculate both reflectance and transmittance of the the membrane, the transfer matrix method is employed. The boundary between two media named i and j is firstly considered as shown in the figure 3.11.

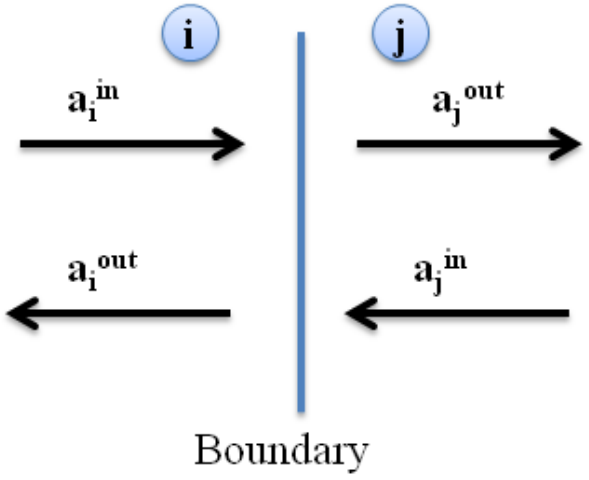

FIGURE 3.11: complex electric field of light amplitudes crossing a boundary.

Here, a_i^{in} and a_j^{in} refers to amplitude of the incoming light from both sides of the sample. The outgoing amplitudes are expressed as a_i^{out} and a_j^{out} respectively. The latter represents the the summation of both transmission part of the left side amplitude a_i^{in} and the reflection part of the right side amplitude a_j^{in}. In contrast, the summation of the reflected amplitude from the left side of the boundary and transmitted amplitude of the right side of the boundary is referred to as a_i^{out} [101]. The cross-polarised scattering is ignored here as the surface roughness is neglected [80]. Thus, the boundary transfer matrix ($\hat{T}_{ij}$)for vertically polarized light(s- polarization) that relates i and j fields can be expressed as follows:

$$\begin{bmatrix} a_i^{in} \\ a_i^{out} \end{bmatrix} = \hat{T}_{ij}. \begin{bmatrix} a_j^{out} \\ a_j^{in} \end{bmatrix} = \begin{bmatrix} T_{ij}^{11} & T_{ij}^{12} \\ T_{ij}^{21} & T_{ij}^{22} \end{bmatrix} . \begin{bmatrix} a_j^{out} \\ a_j^{in} \end{bmatrix} \tag{3.45}$$

It can be seen from the equation that the transfer matrix $\hat{T}_{ij}$ involves four components with i to j directivity. The four transfer matrix elements can be obtained by considering the special cases shown in the figure 3.12(a,b).

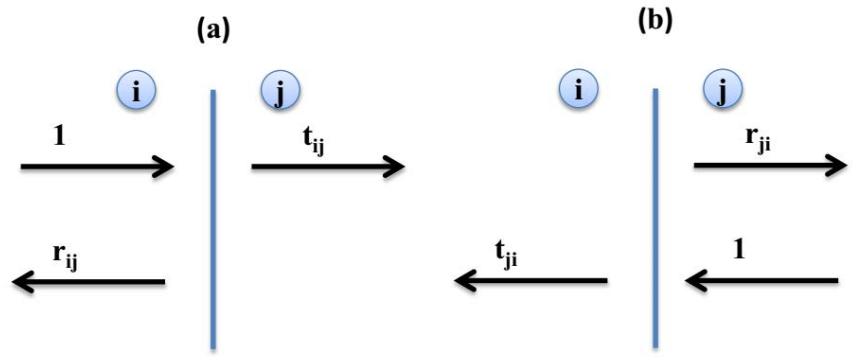

FIGURE 3.12: Amplitude coefficients for (a)light incoming from left to right and (b) light incoming from right to left.

Figure 3.12(a) indicates the case where the unitary field amplitude crosses the boundary from left side of the boundary (i) to the right side of the boundary (j) and r_{ij} represent the reflection of the boundary from media i to j. The direction from left to right is assigned to be positive. Thus, the corresponding equation for this case can be described as follows:

$$\begin{bmatrix} 1 \\ r_{ij} \end{bmatrix} = \hat{T_{ij}}. \begin{bmatrix} t_{ij} \\ 0 \end{bmatrix} \tag{3.46}$$

Following the same procedure, the fields crossing the boundary from j to i in the figure 3.12(b) can be written as follows:

$$\begin{bmatrix} 0 \\ t_{ij} \end{bmatrix} = \hat{T_{ij}}. \begin{bmatrix} r_{ji} \\ 1 \end{bmatrix} \tag{3.47}$$

The equations 3.46 and 3.47 can be expanded by taking into consideration the four elements of the boundary matrix shown in the figure 3.12(b) yielding:

$$\begin{aligned} 1 &= T_{ij}^{11}.t_{ij} \\ r_{ij} &= T_{ij}^{21}.t_{ij} \end{aligned} \tag{3.48}$$

$$\begin{aligned} 0 &= T_{ij}^{11}r_{ji} + T_{ij}^{12} \\ t_{ji} &= T_{ij}^{21}r_{ji} + T_{ij}^{22} \end{aligned} \tag{3.49}$$

The reflection and transmission coefficients from i to j can be obtained from the equation 3.48 and can be expressed as follows:

$$\left.\begin{aligned} t_{ij} &= \frac{1}{T_{ij}^{11}} \\ r_{ij} &= \frac{T_{ij}^{21}}{T_{ij}^{11}} \end{aligned}\right\} \tag{3.50}$$

Thus, the boundary transfer matrix $\hat{T_{ij}}$ can be obtained from the combination of the equations 3.48 and 3.49 as shown below:

$$\hat{T} = \begin{bmatrix} \frac{1}{t_{ij}} & -\frac{r_{ij}}{t_{ij}} \\ \frac{r_{ij}}{t_{ij}} & t_{ji} - \frac{r_{ij}r_{ji}}{t_{ij}} \end{bmatrix} \tag{3.51}$$

By considering that $r_{ij} = -r_{ji}$,$t_{ij} = 1 + r_{ij}$ and $t_{ij} = 1 + r_{ji}$, the boundary matrix can be rather simplified as illustrated in the equation 3.52. Moreover, The directivity of the boundary transfer matrix also confirms the expression $\hat{T}_{ij}^{-1} = \hat{T}_{ji}$.

$$\hat{T}_{ij} = \frac{1}{t_{ij}} . \begin{bmatrix} 1 & r_{ij} \\ r_{ij} & 1 \end{bmatrix} \tag{3.52}$$

It can be seen from the equation 3.52 that the boundary transfer matrix between the i and j mediums depends only on reflection and transmission coefficients r_{ij} and t_{ij} [101].

3.3.4.2 Non−uniform Optical Property

Using the boundary transfer matrix developed in the pervious section, the characteristic matrix based on the WKB method can be derived. The derived matrix can be used to calculate the transmittance and the reflectance of the membrane with spatially nonuniform optical response [101]. Here, the membrane with thickness d is divided into three regions 1, 2, and 3 as shown in the figure 3.13.

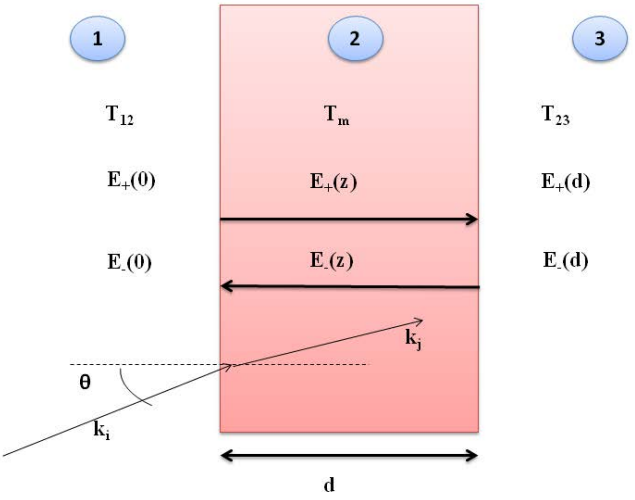

FIGURE 3.13: A membrane cross section where the regions 1 and 3 shows the left and right interfaces while the region 3 is the region of the membrane with non−uniform optical response(non−uniform dielectric function).

The transfer matrices $\hat{T_{12}}$ and $\hat{T_{23}}$ describe the interface separating the regions 1 and 2, as well as the interface 2 and 3 respectively. Based on the equation 3.52, the corresponding matrices can be presented as follows:

$$\hat{T_{12}} = \frac{1}{t_{12}} \begin{bmatrix} 1 & r_{12} \\ r_{12} & 1 \end{bmatrix} ; \hat{T_{23}} = \frac{1}{t_{23}} \begin{bmatrix} 1 & r_{23} \\ r_{23} & 1 \end{bmatrix} \tag{3.53}$$

Here, the transfer matrix of the membrane $\hat{T_m}$can be derived for s- polarised light propagating between the left and right interfaces by assigning the total electric

field between the two interfaces as $E(z) = E_+(z) + E_-(z)$ along the membrane depth between 0 and d. Here, $E_+(z)$ denotes the propagation of light from the left to right while E_{-z} represents the light travelling in the reverse direction. The wave vectors inside and outside membrane are assigned as k_i and k_j respectively.

At any depth z, the electric field is expressed as in the below equation according to WKB approximation [135–138]

$$\begin{aligned} E_\pm = & \frac{a_\pm}{\sqrt{q(z)}}.e^{\pm i\int_0^z dz^{'} q(z^{'})} \\ q(z) = & \sqrt{\frac{\omega^2}{c^2}\epsilon^{'}_{eff}(z) - k_x^2} \end{aligned} \tag{3.54}$$

At any membrane depth, the total wave vectors $k_j(z)$ is presented as:

$$k_j(z)^2 = \frac{\omega^2}{c^2}\epsilon^{'}_{eff}(z) = \frac{\omega^2}{c^2}\left[\Re(\epsilon^{'}_{eff}(z)) + i\Im(\epsilon^{'}_{eff}(z))\right] \tag{3.55}$$

where, k_x, θ, $\epsilon^{'}_{eff}(z)$,$q(z)$ represent the tangential component (parallel to the membrane surface)of the wave vector, the incident angle, the depth dependence dielectric function and the vertical component of wave vector inside the medium at any depth position respectively. The expression $k_i sin\theta_i = k_j sin\theta_j$ can be obtained by multiplying the Snell's law by $\frac{\omega}{c}$ and set the probing frequency $\omega = \omega_i = \omega_j$. As a result, at any depth position (z)of the membrane, the tangential component $k_x = \frac{\omega}{c}\sin\theta$ is always constant as the tangential component $k_i \sin\theta_i = \frac{\omega_i}{c}\sin\theta_i$.

At any arbitrary depth within the membrane between 0 and d, the electric field $E_\pm(z)$ can be formulated based on WKB approximation. The magnitude of the electric field is assigned as $a_\pm/\sqrt{q(z)}$ at any depth position inside the medium. The exponential in the equation 3.54 involves real and imaginary components. The real component attenuates electric field magnitude while the imaginary describes the absorption at any depth inside membrane.

Consequently, the matrix $\hat{T_m}$ relating the fields inside the membrane can be written as follows:

$$\begin{bmatrix} E_+(0) \\ E_-(0) \end{bmatrix} = \hat{T_1}\hat{T_2}\hat{T_3}...\hat{T_n} \begin{bmatrix} E_+(d) \\ E_-(d) \end{bmatrix} = \hat{T_m} \begin{bmatrix} E_+(d) \\ E_-(d) \end{bmatrix} \tag{3.56}$$

Here, the matrices $\hat{T_1}\hat{T_2}\hat{T_3}...\hat{T_n}$ represents the corresponding boundary matrices at each membrane depth position between the front 0 and rear d interfaces respectively. In another words, the membrane can be considered as a medium with infinite boundaries between the front and rear interfaces and each boundary recognised by a specific transfer matrix. The multiplication of the yielded matrices represents the transfer matrix for the membrane $\hat{T_m}$ which also connects between the front side electric field $(E_+(0), E_-(0))$ and the rear side electric field $E_+(d), E_-(d)$, respectively. Following the equation 3.54, the electric field on both sides can be expressed as:

$$\begin{aligned} E_+(0) = &\ \tfrac{a_+}{\sqrt{q(0)}}.e^{i\int^0 dz^{'}q(z^{'})} \\ E_-(0) = &\ \tfrac{a_-}{\sqrt{q(0)}}.e^{-i\int^0 dz^{'}q(z^{'})} \\ E_+(d) = &\ \tfrac{a_+}{\sqrt{q(d)}}.e^{i\int^d dz^{'}q(z^{'})} \\ E_-(d) = &\ \tfrac{a_-}{\sqrt{q(d)}}.e^{-i\int^d dz^{'}q(z^{'})} \end{aligned} \tag{3.57}$$

Substituting the equation above into the equation 3.56 yields the transfer matrix $\hat{T_m}$ for whole membrane as:

$$\begin{aligned} \hat{T_m} &= \sqrt{\tfrac{q(d)}{q(0)}} \begin{bmatrix} e^{-i\psi} & 0 \\ 0 & e^{i\psi} \end{bmatrix} \\ \psi(z,\lambda,\theta) &= \textstyle\int_0^d dz q(z) = \tfrac{\omega}{c}\int_0^d dz\sqrt{\epsilon^{'}_{eff} - sin^2\theta} \end{aligned} \tag{3.58}$$

Here, $\psi(z,\lambda,\theta)$ represents the phase which depends on the depth (z), wavelength and the angle of incident θ respectively. Therefore, the characteristic transfer matrix for the whole membrane shown in the figure 3.13 can be obtained from the multiplication of the front interface matrix $\hat{T_{12}}$, medium matrix $\hat{T_m}$ and rear

interface matrix $\hat{T_{23}}$, which can be expressed as follows:

$$\begin{aligned}\hat{T} &= \hat{T_{12}}.\hat{T_m}.\hat{T_{23}} \\ &= \tfrac{1}{t_{12}}\begin{bmatrix}1 & r_{12}\\ r_{12} & 1\end{bmatrix}\cdot\sqrt{\tfrac{q(d)}{q(0)}}\begin{bmatrix}e^{-i\psi} & 0\\ 0 & e^{i\psi}\end{bmatrix}\cdot\tfrac{1}{t_{23}}\begin{bmatrix}1 & r_{23}\\ r_{23} & 1\end{bmatrix} \\ &= \tfrac{1}{t_{12}t_{23}}\sqrt{\tfrac{q(d)}{q(0)}}\cdot\begin{bmatrix}e^{-i\psi}+r_{12}r_{23}e^{i\psi} & e^{i\psi}r_{12}+e^{-i\psi}r_{23}\\ e^{-i\psi}r_{12}+e^{i\psi}r_{23} & e^{i\psi}+r_{12}r_{23}e^{-i\psi}\end{bmatrix}\end{aligned} \tag{3.59}$$

Based on the equation above, the corresponding reflection and transmission coefficients given in the equation 3.50 can be obtained and can be written as:

$$t = \frac{1}{\sqrt{\frac{q(d)}{q(0)}}}\cdot\frac{t_{12}t_{23}}{e^{-i\psi}+r_{12}r_{23}e^{i\psi}} \quad , \quad r = \frac{e^{-i\psi}r_{12}+e^{i\psi}r_{23}}{e^{-i\psi}+r_{12}r_{23}e^{i\psi}} \tag{3.60}$$

According to Fresnel equation 3.12 and 3.13, the coefficients r_{12} and r_{23} for s-polarised light are as follows:

$$r_{12} = r_0 = \frac{\cos\theta-\sqrt{\epsilon'_{eff}(0)-\sin^2\theta}}{\cos\theta+\sqrt{\epsilon'_{eff}(0)-\sin^2\theta}} \quad , \quad r_{23} = -r_d = -\frac{\cos\theta-\sqrt{\epsilon'_{eff}(d)-\sin^2\theta}}{\cos\theta+\sqrt{\epsilon'_{eff}(d)-\sin^2\theta}} \tag{3.61}$$

Moreover, using the definition of $q(z)$ in equation 3.54 and the wave vector $k_z = \frac{\omega}{c}cos\theta$, the reflection coefficients r_0 and r_d can be expressed as follows:

$$r_0 = \frac{k_z-q(0)}{k_z+q(0)} \quad , \quad r_d = \frac{k_z-q(d)}{k_z+q(d)} \tag{3.62}$$

Therefore, the corresponding reflection and transmission coefficients for whole membrane can be obtained by substituting the equations above into the equation 3.60 and combining the expressions $t_{12} = 1 + r_{12}$ and $t_{23} = 1 + r_{23}$ as follows:

$$r = \frac{r_0e^{-i\psi}-r_de^{i\psi}}{e^{-i\psi}-r_0r_de^{i\psi}} \quad , \quad t = \frac{1}{\sqrt{\frac{q(d)}{q(0)}}}\cdot\frac{(1+r_0)(1-r_d)}{e^{-i\psi}-r_0r_de^{i\psi}} \tag{3.63}$$

By defining $E = e^{i\psi}$, the equations above can be more simplified as given below:

$$r = \frac{E^{-2}r_0 - r_d}{E^{-2} - r_0 r_d} \quad , \quad t = \frac{1}{\sqrt{\frac{q(d)}{q(0)}}} \frac{(1+r_0)(1-r_d)E^{-1}}{E^{-2} - r_0 r_d} \tag{3.64}$$

Then, the definitions $R_t = |r|^2$ and $T_t = |t|^2$ can be used to calculate the reflectance and transmittance for the excited membrane. Once the incident angle θ and the effective dielectric function $\epsilon'_{eff}(z, \lambda)$ of the excited membrane is realised, both R_t and T_t can be calculated and as a result the reflectance $\Delta R/R_o$ and transmittance $\Delta T/T_0$ can be simultaneously fitted. In this case the incident angle can be set from the experimental setup while the background dielectric constant can be obtained from from background reflection and transmission of the unexcited sample. Following that, the contribution of the free generated carriers taken into consideration through incorporating the expression $\Delta\epsilon_{fcr}(z, \lambda)$ into the effective medium approximation used in the model. As it can be seen the from expression $\epsilon_{membrane}(z) = \epsilon_{si} + \Delta\epsilon_{fcr}(z)$ that the only unknown parameter is the contribution of the free carriers $\Delta\epsilon_{fcr}(z, \lambda)$ which can be used as a fitting parameter. By iteratively changing the above parameter, the best fit to the reflection and transmission of the excited sample can be extracted. More details about the fitting process can be found elsewhere [101].

3.4 Optical Model and Mixing Roles

The starting point for each optical model is based on the definition of the layer structure of the sample under investigation. Based on the various diagnostic technique such as X-ray diffraction, Raman spectroscopy, scanning electron microscopy and many others, the fine structure of the material can be described. Moreover, these techniques also provide the ability to distinguish the chemical elements and the phases of the composition as well as the material surface. As we will see in the next section, the volume fraction is an important parameter in effective medium theories, this can be also obtained using the techniques mentioned above. The mathematical description most commonly used to deal with different optical measurements such as absorption, transmission and reflection are discussed

in previous section. The optical model relies on obtaining the complex refractive index of the samples to extract further optical properties. In general, the complex refractive index of any material, at any spectral wavelength can be extracted by fitting the experimental data using properly designed optical model. From the best fit the complex refractive index can be evaluated and used to obtain other optical parameters. The refractive index primarily depends on the generated dielectric polarisation within the medium. This phenomenon arises from the spatial separation of the electric charge in the medium due to applied external electric field [139]. The macroscopic response of the externally distorted material can also be described using optical constants. It is important to note that the chemical bonding holds the charges during the opposite disturbance of positive and negative charges within the material. Thus, the external and internal forces result in the vibrations. Accordingly, the response of the material can be changed by changing the wavelength or the frequency of the applied electric field. Generally, the material structure and the frequency of the external electric field are the most important parameters for obtaining the optical constants of a material. Based on the above discussion, the proper dispersion relation can be used in in simulation to calculate optical properties at a specific spectral range. In the following sections, various optical models related to our primary optical model and used to obtain the dielectric function of different materials will be introduced.

3.4.1 Effective Medium Theories

In the case of a porous semiconductor such as porous silicon, the formation process includes of inter twining of the nano wires c-Si together with empty voids yielding the porous and branched layers. For the purpose of estimating the effective dielectric constant of the whole material, the microstructure impact on the macroscopic dielectric response must be taken into consideration. In the case where the wavelength is long compared to the typical feature size of the topology, the retardation effect can be neglected and the system can be regarded as an effective medium with two component mixed system. This provides the possibility of applying an

effective medium theory to estimate the effective dielectric function ϵ_{eff} of the mixture [140]. In the case of a shorter probing wavelength than the characterising feature size, it is possible to accurately observe and determine the characteristics of the structure. Therefore, various critical parameters such as the spatial correlation length of the dielectric function and the size of the inclusions in the mixture with respect to the probing wavelength need to be carefully considered [141]. The effective medium theories can be generally employed to estimate and determine the dielectric response of the materials with different mixtures. Different algebraic formulas can be used together with mixing rules to calculate the effective dielectric response of a material depending on the volume fraction, constituent dielectric functions and other related parameters. However, in the case of unknown sample mixtures, an approximated form of the mixing rules can be used to predict the effective dielectric response of the medium. It should be noted that computation of the relation between inclusion geometry and the specific mixing rule can not be achieved in the realistic cases even if the average inclusion structure is obtained [140]. For the sake of simplicity, the sample is considered as a medium with two mixed components. These two components are assigned as the host(matrix) and embedded material(or inclusion) with complex dielectric functions ϵ_M and ϵ respectively. The factor $f = NV$ represents the volume fraction of the inclusion and N,V represent the number of inclusions and the volume of the specific inclusion respectively. Both the volume fraction of the inclusions and the average volume fraction of the host material are related through $f = 1 - p$ which allows extraction one of from another and vice versa.

3.4.1.1 Bergman Representation

Bergman established a general representation for obtaining the effective dielectric constant of the media with two phases [142–144]. The representation includes two important parameters, the spectral density g which is the normalised distribution function for the geometrical resonances, and the matrix volume fraction quantity p. The various electric interactions of different material constituents as well as

the microstructure can be characterised based on these geometrical resonances [145–147]. The Bergman effective medium approximation is expressed as follows:

$$\epsilon_{eff} = \epsilon_M[1 - (1-p)\int_0^1 \frac{g(n,p)}{\frac{\epsilon_M}{(\epsilon_M - \epsilon)} - n} dn] \tag{3.65}$$

In the above equation, the effect of the inclusion on the effective dielectric function ϵ_{eff} is expressed through the spectral density g and the volume fraction p. The range of n varies from 0 to 1. Apart from the material properties, the term $g(n,p)$ has been shown to depend only on the geometry which in turn describes the contribution of the microstructure. According to J. Sturm work [148–150] there is no explicit relation established between the function g(n,p) and the inclussion related geometry, the spectral density can only be adjusted experminatally. This effective medium approximation has been also used by D. Sturm to investigate the geometrical structure as well as the dielectric permittivity of the brine-saturated rocks. A three parameter formula for controlling the shape of the spectral density has also been proposed by W. Theiss [140] in the case of porous media. This approach has been regarded as a simple way to handle the general Bergman approximation. The three parameters included in this approach are the percolation strength, porosity, and the broadening resonance parameter d for nearly isolated particles. The approach is expressed as follows:

$$\begin{aligned} g(n,p) &= g_o\delta(n) + \tfrac{3\sqrt{3g_o}}{2\pi n(1-p)^2}[p^2|\tfrac{1-p}{n}|^{1/3}] + p(1-p)|\tfrac{1-n}{n}|^{2/3} \\ &+(1 - \tfrac{g_o}{(1-p)^2})[-\tfrac{3}{4d^3}(n - \tfrac{p}{3})^2 + \tfrac{3}{4d}]\theta(\tfrac{p}{3} - d + n)\theta(\tfrac{p}{3} + d - n) \end{aligned} \tag{3.66}$$

The spectral density g(n,p) comprises of three parts, the percolation of the particles (represented by a delta function), a broad distribution of resonances which can be used to describe a dense particle system, a representation of the weak isolated particle interaction. The later term generates inverted parabola peaking at $p/3$ with flexible width d. The parabola intersects the $n - axis$ at $n = p/3 - d$ and $n = p/3 + d$ respectively. θ represents the heaviside step function.

For inhomogeneous systems, various expressions of the effective dielectric function have been introduced by Maxwell [151], Bruggeman [152, 153]and Looyenga [154]. In most cases, the topology is assumed to be represented by a collection of spheres interacting in a mean local field. Therefore, the formula included in the models above can be regarded as a special cases of the Bergman expression with a typical spectral density for each case [150]. The following sections introduce various models which can be employed in evaluation of the dielectric function of composite materials.

3.4.1.2 Maxwell – Garnett

The Maxwell−Granett mixing rule or the Maxwell − Garnett effective medium expression can be derived based on the Clausius-Mossotti relation[151]. The difference is that in the Clausius-Mossotti the medium was assumed to be a composition of particles and vacuum, while in Maxwell−Garnett relation the medium was assumed to be a spheres embedded in a matrix. The theoretical expression of Maxwell−Garnett model is given as follows:

$$\frac{\epsilon_{eff} - \epsilon_M}{\epsilon_{eff} + 2\epsilon_M} = f\frac{\epsilon - \epsilon_M}{\epsilon + 2\epsilon_M} \tag{3.67}$$

Here, ϵ represents the dielectric function of the spheres and f is the volume fraction of the spheres which can be extracted by multiplying the number of spheres by the volume of the sphere $f = NV$. The three dimensional Maxwell−Garnett relation can be expressed as follows[155, 156]:

$$\epsilon_{eff} = \epsilon_M.\frac{\epsilon(1+2f) - \epsilon_M(2f-2)}{\epsilon_M(2+f) + \epsilon(1-f)} \tag{3.68}$$

This corresponds to a spectral density with distinct sharp resonance as follows:

$$g(n,f) = \delta(n - \frac{1-f}{3}) \tag{3.69}$$

The equation above indicates the possibility of applying the Maxwell − Garnett rule on the media with a low inclusions volume fraction, which in this case are sparsely dispersed spherical particles inside the host matrix. It should be mentioned that the possibility of forming an infinite connected network is not allowed since the particles are separated with large distances. It should be also noted here that there is no existence of the percolation threshold due to micro structure related restrictions [157]. Therefore, Maxwell − Garnett relation can be considered as an ideal model to deal with dilute inclusion embedded in the matrix.

3.4.1.3 Bruggeman Model

For heterogeneous materials, Bruggeman effective medium approximation is usually employed to simulate the effective dielectric constant [158, 159]. The Bruggeman relation can be expressed as follow:

$$(1-f)\frac{\epsilon_M - \epsilon_{eff}}{\epsilon_M + 2\epsilon_{eff}} + f\frac{\epsilon - \epsilon_{eff}}{\epsilon + 2\epsilon_{eff}} = 0 \tag{3.70}$$

The self consistency assumption is taken into account in the derivation of the effective dielectric constant, which implies that the matrix surrounding the embedded inclusion is considered as homogeneous material. The Bruggeman model is widely used for various types of mixed phased materials due to its simplicity as well as its ability to account the percolation phenomena. It should be noted that the above equation provides the possibility of symmetric interchange between the the matrix component and inclusion component. The resultant effective dielectric constant equation can be written as follows:

$$\epsilon_{eff} = \frac{1}{4}\{\epsilon_M(2-3f) + \epsilon(3f-1) + \sqrt{[\epsilon_M(2-3f) + \epsilon(3f-1)]^2 + 8\epsilon_M.\epsilon}\} \tag{3.71}$$

The corresponding spectral density for the Bruggeman effective medium approximation can be described as follows:

$$g(n,f) = \frac{3f-1}{2f}\theta(3f-1)\delta_{+}(n) + \frac{3}{4\pi f n}\sqrt{(n-n_L)(n_R-n)} \tag{3.72}$$

with

$$n_{R/L} = \frac{1}{3}(1+f \pm \sqrt{2f-2f^2}) \tag{3.73}$$

In the above equations, both the continuous distribution of resonance and the sharp resonance associated with the volume fraction of the inclusion f can be observed in the spectral density. The contribution of the two resonances in the above model is rather realistic compared to the single resonance observed in Maxwell Garnett model, especially for the media with high volume fraction and irregularly shaped inclusions. Furthermore, the model can predict the behaviour of the percolation if the volume fraction f of the inclusions is sufficient to produce a continuous network. The infinite continuous network can be established by inclusions once the condition of $f > 1/3$ is fulfilled while the matrix is in state of continuous network for $f < 2/3$. The inclusions and the matrix are connected in symmetric micro structure when $f > 1/3$ but $< 2/3$, unlike the dispersion micro structure, generally there is no contribution of the anomalous dispersion. Hence, it can be concluded that the Bruggeman effective medium approximation not only explains the sparsely dispersed micro structure assumed in the Maxwell−Garnett model but also it provides the ability to account for a mixture of aggregated micro structures. Further comparisonn between the Bruggeman and Maxwell−Garnett effective medium approximations have been detailed by Niklasson[159] and Hongro Ma[157]. The Bruggeman model accuracy for predicting the effective dielectric function of the materials and why its efficient compared to other models has been summrized by Goncharenko [160].

3.4.1.4 Looyenga model

Looyenga model was proposed by H.Looyenga [154] and can be used to determine the effective response in electromagnetic field based on only the volume fraction parameter f. The theoretical formula can be expressed as follows:

$$\epsilon_{eff}^{1/3} = (1-f)\epsilon_M^{1/3} + f\epsilon^{1/3} \tag{3.74}$$

The corresponding spectral density includes a wide range of continuum resonances and can be expressed as:

$$\begin{aligned} g(n,f) = f^2\delta_+(n) + \tfrac{3\sqrt{3}}{2\pi}[(1-f)^2|(n-1)/n|^{1/3} \\ +f(1-f)|(n-1)/n|^{2/3}](1-\delta_{0,n}) \end{aligned} \tag{3.75}$$

considering the above equations, the model can be regarded as an effective solution to describe densely packed composites, however this is less valid in the case of dilute particles systems.

All the models introduced previously have advantages and disadvantages depending on the spectral density and percolation behaviour of the simulated system. The Bergman relation is rather complex compared to the other models described above. The Maxwell−Garnett model is effective for the determination of effective dielectric functions for media with low volume fractions. Meaning systems with dilute particles separated by large distances, as such the percolation threshold is not considered in this model. Therefore, the Maxwell−Garnett model can be considered as the best choice for dealing with dilute particles embedded in the matrix. The Bruggeman model takes into account both the spectral density and percolation threshold. Hence, both dilute and dense systems can be treated effectively using the Bruggeman model. However, this model can not predict the plasmon resonance, which is a significant drawback.

3.4.1.5 Free Carrier Contribution To the Dielectric Function

The optical properties of the free electron gases or metals with dense free electron have generally been investigated using the Drude model. With presence of the probe electric field, the free electron in such systems do not undergo any restoring force. However, in the case of excited semiconductor materials the electron and

hole movements in the valence and conduction band need to be taken in to consideration. By assuming the electrons as a particles and replacing the free electron mass m_e by the effective mass m^* the restoring force issue can be resolved. To describe the dielectric function of free electron systems, the Lorentz oscillator model with no contribution of restoring force term is used to derive the Drude model. By applying the probe signal as an AC electric field $E(t) = E_0 e^{i\omega t}$, the oscillation of the induced free electrons can be described using the following equation:

$$m_e \frac{d^2x}{dt^2} + m_e \Gamma \frac{dx}{dt} = -eE(t) = -eE_0 e^{i\omega t} \tag{3.76}$$

Here, ω and E_0 refers to the angular frequency and the amplitude of the probe light respectively and Γ represents the damping rate. The first term in the equation indicates the electron acceleration while the second term is the medium fractional damping force. The term in the right hand side represents the force exerted by the probe beam. Substituting the velocity of the electron $v = dx/dt$, the above can be rewritten as follows:

$$m_e \frac{dv}{dt} + m_e \Gamma v = -eE(t) \tag{3.77}$$

Replacing $m_e v$ by the momentum p, the rearrangements of the equation yields:

$$\frac{dp}{dt} = -\frac{p}{\tau} - eE(t) \tag{3.78}$$

where, $\tau = 1/\Gamma$ is the damping time or the momentum scattering time, indicating the electron momentum loss over time. Assuming $x = x_0 e^{i\omega t}$ and $v = v_0 e^{i\omega t}$ as solutions of the motion [161], we can find:

$$x = \frac{eE_0}{m_e(\omega^2 - i\Gamma\omega)} \qquad \text{and} \qquad v(t) = \frac{-e\tau}{m_e} \frac{1}{1 + i\omega\tau} E(t) \tag{3.79}$$

As it is mentioned previously, the electron mass m_e shown in the above equation should be replaced by m^* when dealing with semiconductors. Moreover, the contribution of the inter band transition together with the absorption due to lattice vibration and their background relative permittivity should be also taken into account. Since the polarisation due to free carriers is given as $P_{fcr} = -N_{e-h}ex$ where N_{e-h} refers to the number of carriers per unit volume, the electric displacement including all the contribution is expressed as follows [161]:

$$\left.\begin{aligned} D &= \epsilon\epsilon_0 E \\ &= \epsilon_0 E + P_{back} + P_{fcr} \\ &= \epsilon_{back}\epsilon_0 E - \frac{N_{e-h}e^2 E}{m^*(\omega^2 - i\Gamma\omega)} \end{aligned}\right\} \tag{3.80}$$

Where, P_{back} and P_{fcr} are the bounded electron background polarisability and the polarisability due to the free carrier respectively. The effect of the semiconductor band structure on the free carriers is also incorporated in the equation through including the effective mass $\frac{1}{m^*} = (\frac{1}{m_e^*} + \frac{1}{m_h^*})$, where m_e^* and m_h^* represent electrons and holes effective masses respectively. The term N_{e-h} refers to the number of electron-hole created by the pump beam. Thus, the dielectric function of the semiconductor excited by the external source can be expressed as follows:

$$\epsilon = \epsilon_{back} - \frac{N_{e-h}e^2}{m^*\epsilon_0}\frac{1}{\omega^2 - i\Gamma\omega} \tag{3.81}$$

It can be seen from the above equation that the dielectric constant also depends on the angular frequency of the probe beam. Another parameter is the plasma frequency ω_p which is defined as follows

$$\omega_p^2 = \frac{N_{e-h}e^2}{m^*\epsilon_0} \tag{3.82}$$

By considering all the parameters of the excited semiconductor, the final dielectric constant can be given as

$$\epsilon = \epsilon_{back} + \Delta\epsilon_{fcr} = \epsilon_{back} - \frac{\omega_p^2}{\omega^2 - i\Gamma\omega} \tag{3.83}$$

Based on the obtained dielectric constant, the parameters related to the ultrafast dynamics of photo excited plasma such as the plasma frequency ω_p as well as the scattering rate Γ can be realised. Here, ω_p provides information about the band structure through including the effective mass as well as the photo excited carrier concentration, while the information about the scattering processes such as carrier - carrier and carrier-phonon scattering can be derived from the scattering rate Γ. The change in the complex dielectric constant that arises from free carrier absorption can be defined as $\Delta\epsilon_{fcr} = \Delta\epsilon' - i.\Delta\epsilon''$ where ϵ' and ϵ'' are the real and imaginary parts of the dielectric constant and their corresponding formulas can be expressed as follows:

$$\Delta\epsilon' = -\frac{\omega_p^2}{\Gamma^2 + \omega^2} \qquad \text{and} \qquad \Delta\epsilon'' = \frac{\omega_p^2\Gamma}{\omega(\Gamma^2 + \omega^2)} \tag{3.84}$$

It can be seen from the equations above that the change in the real and imaginary parts of the complex dielectric constant are significantly influenced by the change in the plasma frequency ω_p as well as the scattering rate Γ. The term ω in the above equation refers to the probe angular frequency used in this study which is in the Mid-infrared range (MIR). The damping time $\tau = 1/\Gamma$ depends on the photo generated carriers as well as the lattice temperature. It has been shown that the carrier relaxation is dominated by the carrier-phonon collisions ($\tau = 10^{-13}s$) at low carrier carrier concentrations [76], while at high carrier concentration, where the total momentum is conserved, carrier-carrier collision is dominant and the resulted damping time is on the range of femtosecond time scale ($\tau = 10^{-15}$) [162]. In the following sections the fitting procedures of the various spectroscopic pump-probe geometries such as reflection and transmission for excited and unexcited samples based on the models and equations mentioned previously. From the simulation process the plasma frequency ω_p as well damping rate Γ can be extracted which provides important information about the ultrafast process in the sample under investigation. Detailed information about the simulation process and obtaining Drude parameters (N and Γ) will be introduced in the later sections.

3.5 Time Resolved Spectroscopy

The optical spectroscopy is widely used to reveal valuable information related to electronic dynamics, optical properties of the surfaces and interfaces of the semiconductor. This can be carried out using optical spectroscopic methods such as reflection, transmission and ellipsometry. In fact, the information about non-linear, non-equilibrium and relaxation and transport dynamics of semiconductor can be also explored if the ultrafast laser systems are employed in the measurements [163]. In this section, an overview of the ultrafast time resolved approach used in this thesis will be provided.

For the purpose of studying the quantum mechanical and ultrafast microscopic processes in the materials, the ultrafast laser pulses has been regarded as an effective tool for the excitation and stop-action measurements. The process involves using a femtosecond laser pulses to study the time evolution of the various dynamical processes in the solid state materials. Time resolved measurements are widely implemented in association with the pump-probe technique.

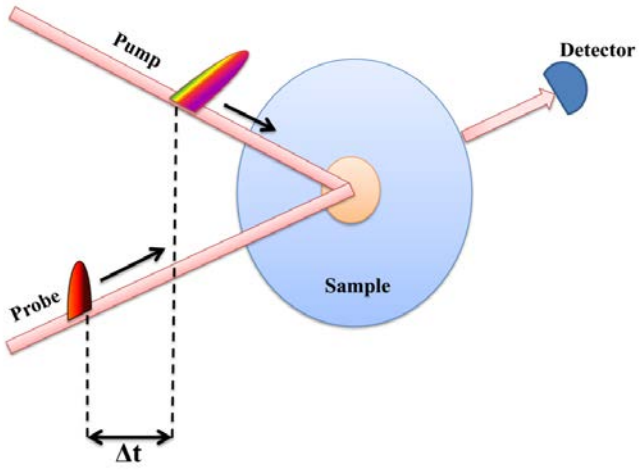

FIGURE 3.14: A schematic representation of the pump-probe technique. The high intensity pump excites the sample to a non-equilibrium state while the weaker probe is guided to excited area after time delay, Δt, to detect the variation in the optical properties of the sample

In this process, the main beam is split into two parts with different intensities using a beamsplitter. The first part with high intensity is termed as the pump

and used to optically excite the sample under investigation. While the second part with lower intensity is employed to evaluate the optical properties of the sample following the optical excitation. The time evolution of the ultrafast dynamical processes induced by the pump beam can then be evaluated by controlling the time delay between the pump and probe beams. This can be regarded as high speed electronic snapshot of various macroscopic related mechanical motions [164]. Figure.3.14 shows a schematic representation of the pump probe technique. As mentioned, a non-equilibrium state is generated using an intense pump pulse. Generally, exciting semiconductors with photon energy greater than the band gap energy generates a high density of free carriers through the absorption of the pump energy. In addition, the generated carriers can also result in a change of the lattice temperature, band gap amongst other changes. After the excitation, The excited states of the medium can then be evaluated using the weak probe beam yielding valuable information regarding the dielectric constant as well as the dipoles polarisation induced by the pump. Thus, the deconvolution of the estimated dielectric function provides important information about all the phenomena that occurs in the excited states. This can be further clarified through representing the optical property of the excited state by $\epsilon(t)$ and the corresponding formula can be given as follows:

$$\epsilon(t) \rightarrow \epsilon_{t<t_0} + \Delta\epsilon(t - t_0) \tag{3.85}$$

Where, ϵ_{t-t_0} represents the optical property of unperturbed medium while $\Delta\epsilon(t - t_0)$ indicates the change of the optical properties at specific time t following the excitation time t_0. The probe beam can be varied relative to the pump allowing the investigation of the time dependent optical properties of the excited state. In Figure 3.14, Δt refers to the time difference between the probe arriving (detection time t), and the time of the excitation t_0. The probe intensity is normally rather low compared to the pump intensity to prevent further medium perturbation. Hence, the transient change in optical properties $\epsilon(\Delta t)$ can be obtained

as a function of time delay through precise control of the optical path difference between the pump and probe pulses.

It should be noted that various optical spectroscopic geometries such as transmission and reflection of the probe beam can be measured to reveal the time dependence dielectric function following the optical excitation. The time dependent optical properties $\epsilon(\Delta t)$ depend primarily on the carrier-carrier scattering rate and the concentration of the excited carrier.e.t.c. To reveal the physics underpinning $\epsilon(\Delta t)$ values, a detailed theoretical model is required to describe the time resolved data as well as the related dynamical processes [165].

In this study, various spectroscopic geometries such as reflection and transmission based on the time resolved pump-probe technique are applied to realise the ultrafast dynamic processes of micro and nano structured silicon membranes. It has been shown that the pump-probe reflection is highly sensitive to absorption changes as well as the changes of the refractive index while pump-probe transmission has been usually employed to realise the time resolved absorption [164]. Once the complex dielectric function $\epsilon = \epsilon_r - i.\epsilon_i$ of the excited medium is obtained, the dynamic processes of the excited carriers and the related steps following the excitation can be revealed.

3.5.0.1 Simulation Procedures and Example

The dielectric function illustrated in the equation 3.83 encompasses two important contributions. The first one ϵ_{back} is the dielectric constant without any sample perturbation (without excitation) including lattice vibration as well as interband transition, while the second term ϵ_{fcr} is the contribution of photo excited free carriers to the dielectric constant. The dielectric function of the unexcited nano or micro porous siliconϵ_b can be revealed by simulating the reflection and transmission spectra of the unexcited sample.

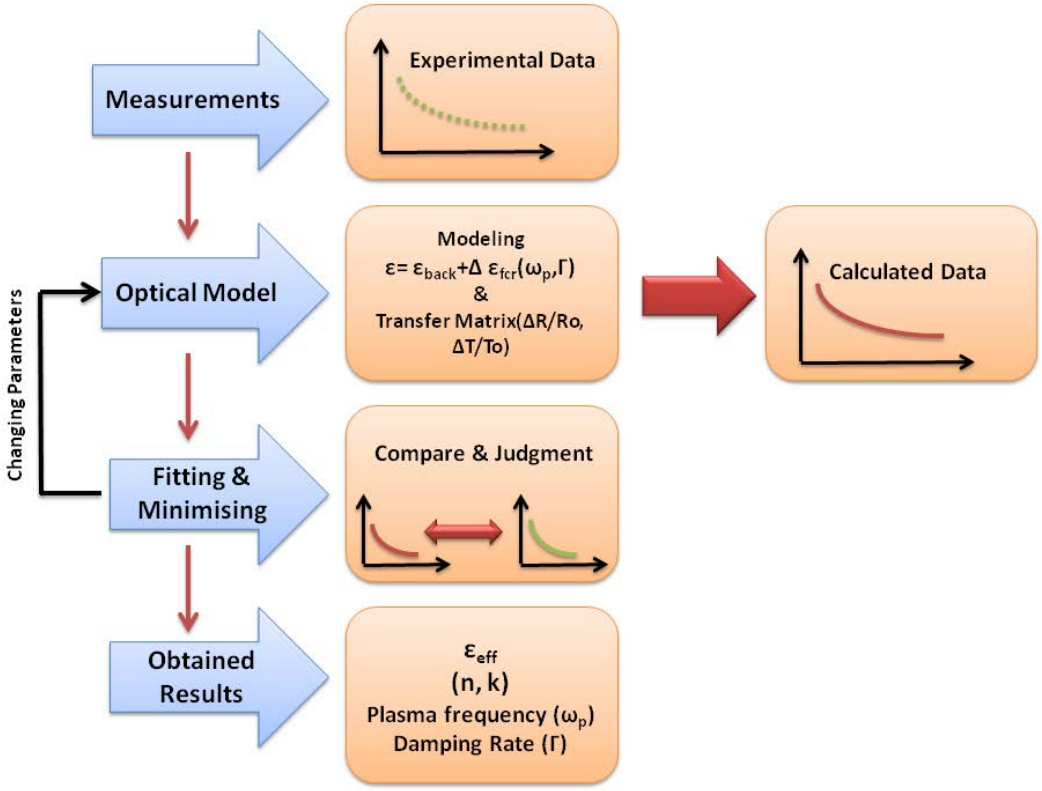

FIGURE 3.15: Flowchart describing the data fitting procedure for the pump - probe approach. Both the background dielectric constant and the free carrier response to the dielectric constant are included in the optical model of the excited semiconductor. Combining the transfer matrix method with the optical model provides the possibility of calculating the reflection R and transmission T in the steady state. The reflectance $\Delta R/R_0$ and the transmittance $\Delta T/T_0$ changes can be also calculated and fitted to the experimental data by changing the fitting parameters (ω_p, Γ) and minimising the fitting errors

.

This can be achieved by taking into account the structure of the sample in the selected model, e.g. the porosity and the shape of the pores. By combining the chosen optical model (discussed in the previous section) with the transfer matrix model the dielectric constant at the steady state can be extracted from the best fit of the experimental data. The best fit can be realised through changing the fitting parameters, in this case is the dielectric constant.The fitting procedure is shown in the flowchart figure above. The figure shows the fitting procedure applied to both the excited and unexcited sample with minor adjustment. For the excited sample some fitting modification is required since the contribution of the photo

excited free carriers needs to be incorporated. Thus, the overall dielectric constant includes the background dielectric function of the sample and the contribution of the free carrier response and can be defined as $\epsilon = \epsilon_{back} + \Delta\epsilon_{fcr}(\omega_p, \Gamma)$. The background dielectric constant can be extracted by simply fitting the experimental data. The contribution of the pump excited electrons to the dielectric constant of the excited sample can be determined by incorporating Drude model with dielectric function of the excited sample as is shown in the equation 3.84. The best fitting of the experimental data can be obtained by iteratively changing the values of the plasma frequency ω_p as well as the damping rate Γ. Taking into account the angle of incidence as well as the sample structure together with transfer matrix method, the reflectance and transmittance can be calculated.

The time resolved reflectance and transmittance of the sample under investigation is defined as $\Delta R/R_0 = (R(t) - R(0))/R(0)$ and $\Delta T/T_0 = (T(t) - T(0))/T(0)$ where $R(0)$ and $T(0)$ represent the reflection and transmission of sample without excitation. There are two ways to obtain $R(0)$ and $T(0)$, the first way is through using the transfer matrix method and the second approach is through direct measurement using simple spectroscopic methods such as FTIR or the pump probe setup without excitation. The $R(t)$ and $T(t)$ represent the reflection and transmission of the excited sample and can be detected by changing the time delay between the pump and probe using rotoreflector mirrors mounted on a one dimensional transitional stage. Incorporating the free carrier response ϵ_{fcr} together with the background dielectric constant ϵ_{back} into the effective dielectric constants provides the capability of calculating the the reflection $R(t)$ and transmission $T(t)$ at each time delay after the excitation. As a result, the corresponding reflectance $\Delta R/R_0$ and transmittance $\Delta T/T_0$ can be also calculated. The calculated reflectance and transmittance changes can be then fitted to the experimental measurements through iterative change of the Drude parameters to minimise the fitting error. By obtaining the best fit, the values of the effective dielectric function, plasma frequency and the damping rate can be retrieved. This procedure provides the possibility of extracting the both components of the Drude model as well as the effective dielectric function as a function of the time delay between the

pump and probe. In the case of a poor fit, some modification on the optical model is required before repeating the same fitting process including iterative change of the Drude parameters to minimise the fitting errors, this case is illustrated in the judgement section of the flowchart.

3.5.1 Example

In order to evaluate the constructed optical model, the fitting procedure shown in the the previous section was followed.

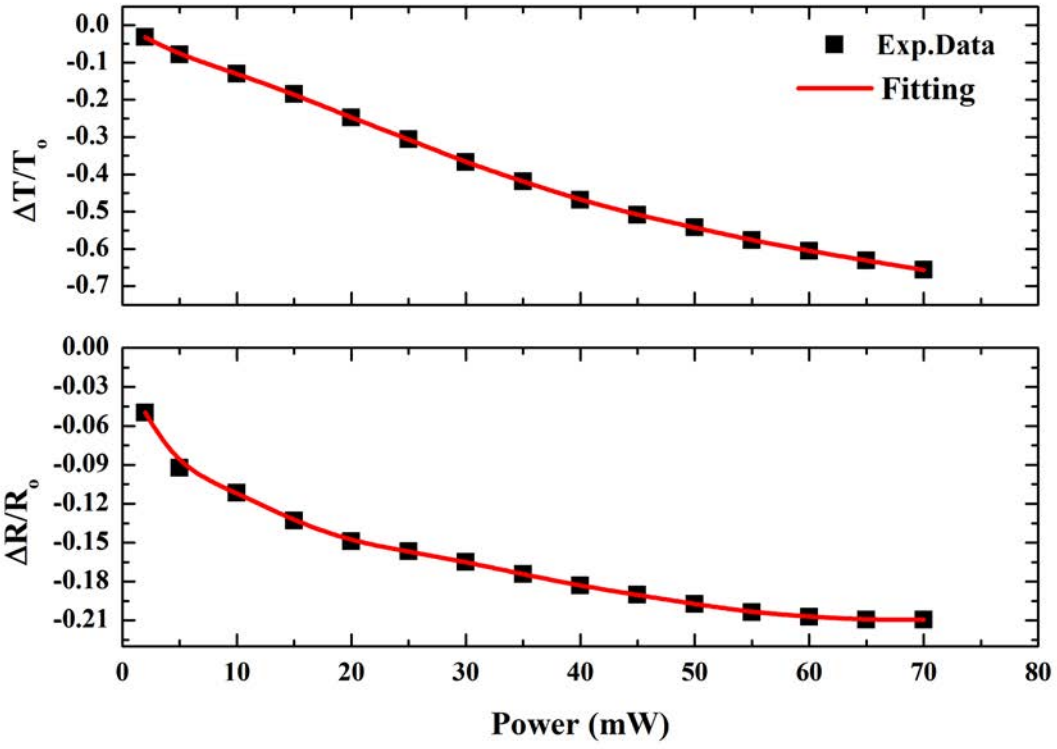

FIGURE 3.16: The reflectance (upper panel)and transmittance (lower panel)changes of 26μm-thick microporous silicon (mpSi) as function of pump power at 4μm probe wavelength. The black squared points represents the experimental data while the solid red line represents the the fitting obtained from Maxwell−Garnett model together with transfer matrix method.

Here, the optical model based on the Maxwell−Garnett effective medium approximation, modified to include a Drude like contribution, was used. The Drude

parameters including the pump induced carrier concentration N as well as the scattering rate Γ are used as fitting parameters. By combining the transfer matrix method illustrated previously, the reflectance and transmittance changes can be fitted. The process is based on minimising the difference between the experimental data and the model. This can be achieved by iteratively changing Drude parameters and obtain best fitting. Figure 3.16 shows the reflectance and transmittance changes for $26\mu m$-thick microporous silicon (mpSi) with pore diameter of $2.5\mu m$ and 40% porousity separated by $4.2\mu m$ pitch as a function of pumping power at $4\mu m$ probe wavelength. It can be seen From the figure that the model is able to fit both the reflectance and transmittance changes simultaneously with good agreement.

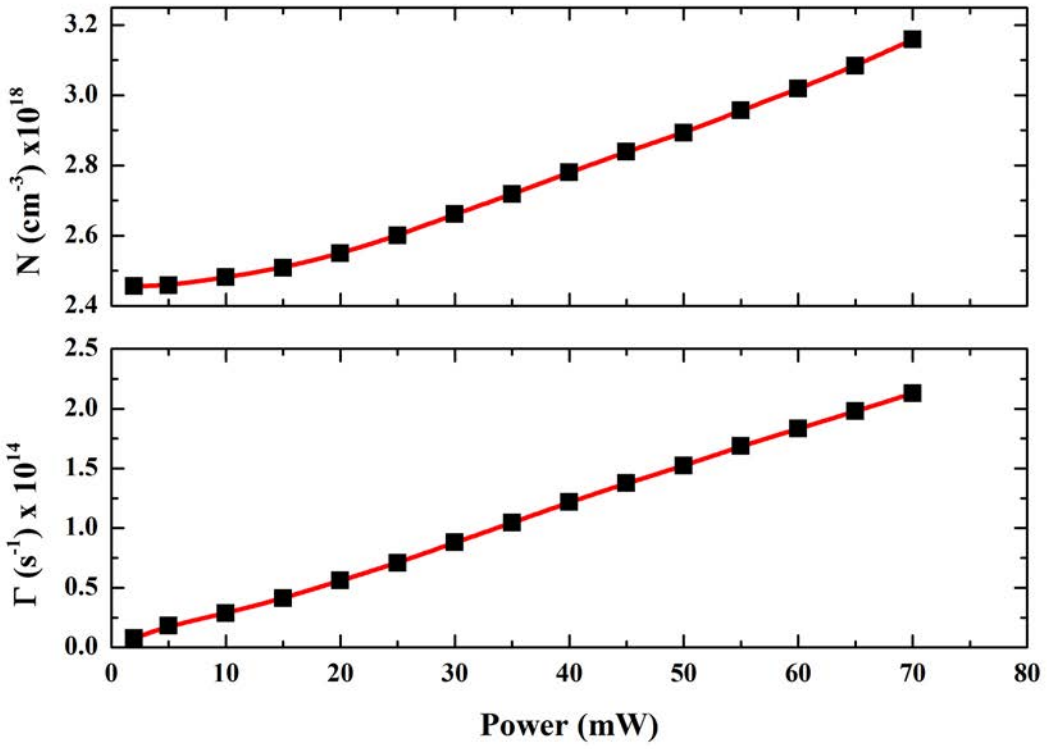

FIGURE 3.17: The photo-generated carrier concentration N (upper panel),as well as, the scattering rate Γ (lower panel)for $26\mu m$-thick $mpSi$ extracted from the reflectance and transmittance changes shown in the figure 3.16 as a function of pumping power at $4\mu m$ probe wavelengths.

Figure 3.17 shows the Drude parameters N (upper panel)and Γ (lower panel)

retrieved form the fitting of the reflectance and transmittance changes shown in the figure 3.16 as a function of the pump power with a probe wavelength of $4\mu m$. It can be seen from the figure that both generated carriers N and the scattering increase with the increasing the excitation fluence. The model also provides the possibility of evaluating the optical properties of the sample through extracting the effective dielectric function of the excited sample.

Figure 3.18 shows the real and imaginary parts of the effective dielectric function as a function of pumping power. It can be seen from the figure that the real part of the effective dielectric function gradually drops with increasing the excitation fluence followed by saturation for powers greater than $40mW$. The imaginary part however linearly increases with excitation power. This indicates that the sample becomes more absorptive with increasing pumping power due to the absorption of the probe by the photo-generated carriers.

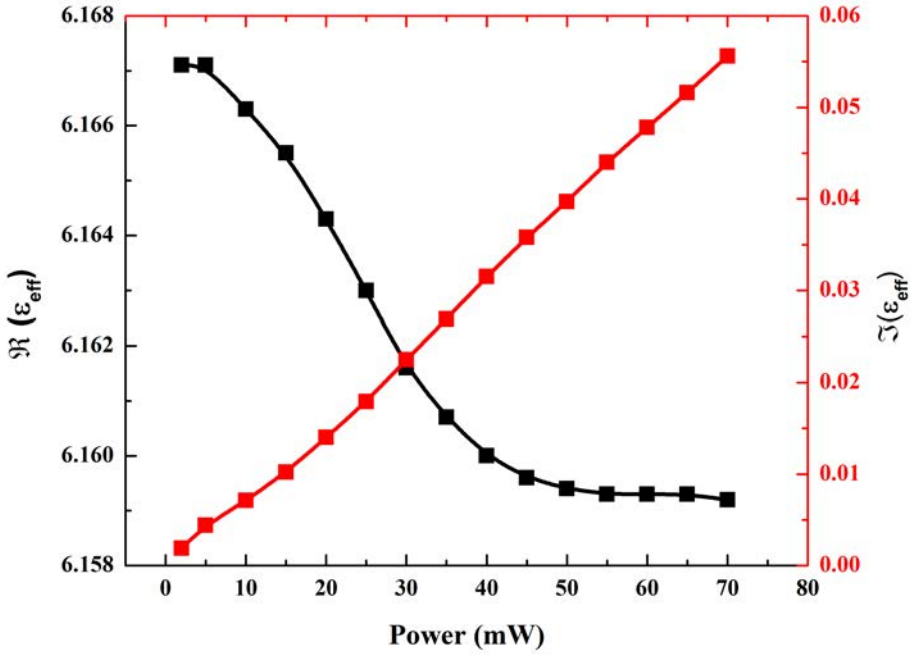

FIGURE 3.18: The pump induced change in the real (black dotted)and the imaginary (red dotted) of the effective dielectric function of the $26\mu m$-thick (mpSi)at $4\mu m$ probe wavelength.

From these results, it can be concluded that the procedure followed to simulate the experimental data is valid to evaluate and extract the optical properties of the excited semiconductors. Moreover, the model can be also used with Bruggeman effective medium approximation depending on the sample structure.

3.6 Summary

The chapter introduced the ultrafast laser system used to investigate the optical modulation and the carrier dynamics in nano and microporous silicon samples based on pump-probe technique. In order to build the optical model that can be used to analyse the reflection and transmission of both samples, the basic review of the reflection and transmission at normal and arbitrary incident angle was presented. The transfer matrix method has also been described here in the manner in which it will be applied to simulate the reflection and transmission based on the constructed optical model. The structure of the semiconductor is also taken into consideration through incorporating the effective medium theory in the optical model. In order to simulate the reflection and transmission without excitation, the effective medium theory has been combined with transfer matrix method can be employed. For the excited semiconductor, the contribution of Drude model should be also incorporated into effective medium approximation. The fitting procedure using the constructed optical model has also been introduced which illustrates the steps followed to obtain the ultrafast parameters such as N, Γ and the effective dielectric function of the sample. Finally, the optical model was evaluated through analysing the $26\mu m$-thick $mpSi$ sample with 40% porosity separated by $4.2\mu m$ pitch and retrieving the complex dielectric function as well as Drude parameters.

Chapter 4

Optical modulation in structured silicon membranes

In this chapter, we investigate and compare the possibility of using nano and micro porous silicon (ordered hole arrays) as optically controlled modulators operating at wavelengths between 3.3μm and 5μm of the Mid Wave infrared (MWIR)spectrum. The pump- probe technique is used to measure the spectral, fluence and transient reflection and transmission for different sample thicknesses. **The main results and discussions included in this chapter are also published in two separate papers titled as follows:"All-optical modulation in Mid-Wavelength Infrared using porous Si membranes." Scientific Reports 6 (2016)**[44] **and "MWIR optical modulation using structured silicon membranes." SPIE Security+ Defence. International Society for Optics and Photonics, 2016** [166]**. This chapter also includes text and figures taken from these papers.**

4.1 Introduction

Although some researches have been carried out on optical modulation in semiconductors, the electro-optical modulators covering the range between 3.5 and

$6\mu m$ of the Mid-Wavelength Infrared (MWIR) are not available commercially despite acute market interest. Such optical modulators are considered a critical components in thermal imaging devices for military and civilian applications as well as optical telecommunications technologies. New capabilities such as rapidly activated sensor protection, time of flight and hyperspectral imaging and ultrafast non uniformity correction can be accomplished and the drawbacks of traditional electro-mechanical modulators can be overcome by realising an effective fast electro-optical modulator.

Many optical modulation approaches including thermo-optical and electro-optical [37, 167–169]and their feasibility in the practical world have been suggested previously. Among these approaches, optical modulation arising from the electron-hole plasma has attracted enormous intrest since it provides sharper spectral modulation depth as well as faster response time [37]. The free electrons in this case are generated by either applying an electric field (Franz-Keldsh effect), or by exposing the silicon to an external light source which in turn induces changes in the optical properties of the silicon. The Franz-Keldsh effect is ignored in the case of silicon as it is relatively weak in this material [37]. The importance of the optical modulation approach arises from the fact that it avoids signal conversion from electrical to optical providing less noise with a faster switching speed. Various technological fields such as dual- band filtering of infrared broad band imaging systems [170–172], optical communications and network interconnects [173, 174] rely on the afore-mentioned features to develop effective components in these fields. Despite the advances that have been achieved so far, the components operating at longer wavelengths are still out of technological reach as they cover spectral bands of visible and near infrared (NIR) [175–178].

Optical modulators operating at longer wavelengths have attracted considerable attention recently due to their potential benefits in different technological fields such as multi-spectral infrared imaging and free space optical communications. Moreover, the motivation for focusing on such research rises from the fact that

these optical components have relatively higher performances in inconvenient atmospheric conditions. Theoretical studies have demonstrated the feasibility of using crystalline silicon as an optical modulator operating at MWIR and the longer wavelengths, particularly the wavelength range between 1 and 14μm [45]. This study indicated that the change in the refractive index induced by free carrier excitation enhances when moving towards the longer wavelengths. The optical modulation of a quantum cascade laser with wavelength of 4.72μm used as an optical source for free space optical communication has also been studied, at which two IR beams with wavelengths 1.38 and 1.95μm were used to directly modulate the source[179]. It has been also shown that optical modulation based on the plasma dispersion effect of crystalline silicon in the wavelength range $2 - 2.5\mu m$ is rather prominent compared to that shown for optical communication wavelengths [180], which is also theoretically predicted [45]. Recently, a novel silicon-on-lithium-niobate platform demonstrated a modulation frequency for $23kHz$ at $3.39\mu m$ using the Pockels effect [181], while germanium-on-silicon waveguides demonstrate an optical modulation frequency of $50MHz$ for wavelengths spanning $2 - 3.8\mu m$ due to the free carrier absorption [182]. In most previously implemented studies, optical modulation has been investigated either on a limited spectral band or at a few discrete wavelengths while optical modulation over the MWIR range remains unevaluated. In this chapter, we evaluate and compare all-optical modulation in sub-wavelength structured silicon membranes and their performance in the MWIR range. Particularly, we assess and compare the possibility of using microporous silicon (mpSi) and nanoporous silicon (npSi) as optical modulators in the MWIR wavelengths range. This chapter comprises three sections, the first section provides information about spectral measurements measured using Fourier Transform Infrared spectroscopy (FTIR),while the second section compares the modulation contrast(the change in transmittance) of optically excited samples at specific pump power over the MWIR range. The third section presents the transient response of the sample as a function of the delay time between the pump and probe signals. This is very important, as it enables us to estimate the switching speed of the

sample under investigation. We also focus on the transient reflectance of microporous silicon (mpSi) and its distinct behaviour over various pump excitation. We show that both samples are worthy of study since they demonstrate promising qualities which can be exploited in the development of electro-optical modulators and circuits. However, the response of the samples under optical excitation are dissimilar in terms of spectra, contrast and the transient feedback. For instance, the optical modulation of the microporous silicon (mpSi) is efficient at shorter wavelengths while the the transient response of nanoporous silicon is almost three orders of magnitude faster compared to that of microporous silicon (mpSi). Furthermore, the difference in the optical properties of these samples might be useful in the design and development of future optical devices as it can be changed by controlling the porosity of the samples.

4.2 Spectral Characterisation

This section presents transmission (without pump excitation) spectra for nano porous silicon membrane with thicknesses of $13\mu m$, $27\mu m$ and $111\mu m$ as well as the transmission of micro porous silicon (ordered hole arrays) with thicknesses of $16\mu m$ and $50\mu m$. The spectra in Figure 4.1 are measured using a Bruker FTIR Hyperion spectroscope with unpolarized light. Figure 4.1(a) shows the transmittance, T_0, in the range between 2 and $10\mu m$ measured with(FTIR)for $111\mu m$ thick nanoporous silicon membrane $npSi$ with 71% porosity. It is apparent that the transmittance in this materials strongly dependant on wavelength. In this work our main concern lies in the MWIR range, especially 3.5 to $4.4\mu m$, marked as a shaded area in Figure 4.1, Here, there is a high transmission window of about 84%, centred around 4.0μm. Both sides of this window are framed by peaks of strong absorption at 3.0, 4.4 and $4.7\mu m$. This unique spectral feature of great optical contrast in transmittance creates an optical window transparent for MWIR, while nearby shorter and longer wavelength are blocked due to absorbance. We note that other samples of diferent thickness and porosity were also tested. However, the $111\mu m$ thick $npSi$ membranes with 71% porosity showed nearly

optimal spectral features−high contrast ratio between the transmission around $4.0\mu m$ and strong absorption due to surface adsorbates. It is well-known that the transmittance decreases, on either side of the transparent window can be attributed to the absorption of impurities associated with the molecular vibration modes of Si-OH, Si-H, and O-Si-H [81, 84, 183, 184] found on the surface.

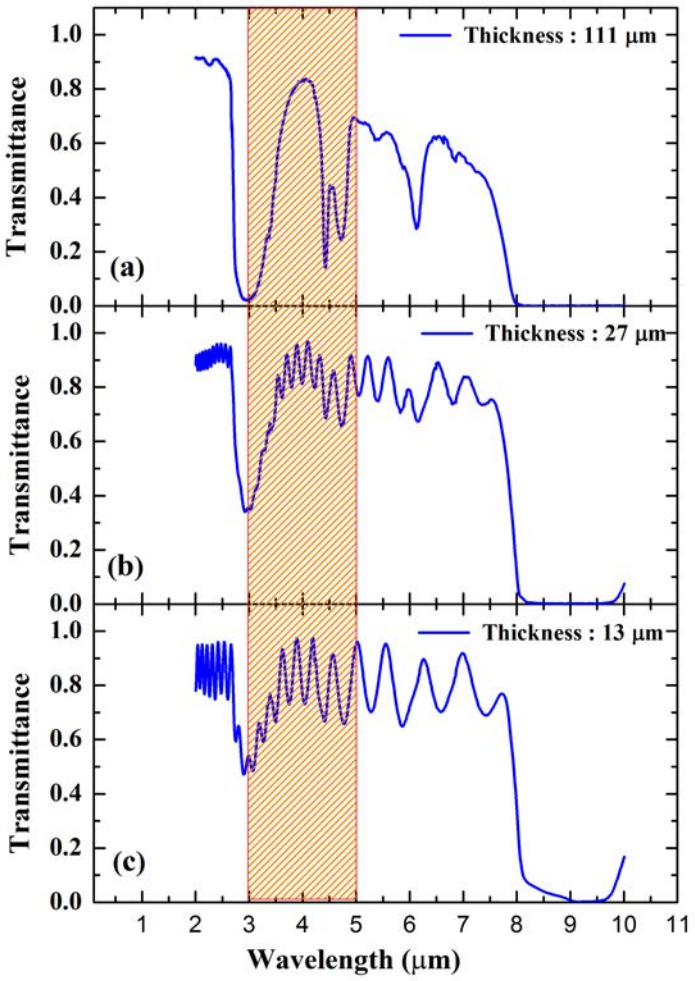

FIGURE 4.1: The transmittance T_0 for (a) $111\mu m$ thick nanoporous membrane(b) $27\mu m$ thick nanoporous membrane (c)$13\mu m$ nanoporous membrane measured using FTIR spectroscopy and the dashed area indicates the MWIR wavelength range between $(3-5\mu m)$. The porosity of the samples used here ranging from $64-71\%$.

While in the bulk material these transitions are usually not observed because of

Vibrational mode	**Absorption peak position in μm (cm^{-1})**
O_1SiH_3	$4.63\mu m(2160cm^{-1})$
O_2SiH_2	$4.52\mu m(2210cm^{-1})$
O_3SiH_1	$4.41\mu m(2270cm^{1})$
SiH	$4.79\mu m(2087cm^{1})$
SiH_2	$4.74\mu m(2108cm^{1})$
SiH_3	$4.67\mu m(2142cm^{1})$
$Si-OH$	$3\mu m(3330cm^{1})$

TABLE 4.1: Assigned absorption peaks over the wavelength range from $3\mu m$ to $5\mu m$ of the MWIR [81, 84, 183, 184].

their low optical density; in $npSi$ they are strong and stable due to its high surface-to-volume ratio. The absorption wavenumbers from the FTIR results around the transparent window are detailed in Table 1. It can be seen from the Table 4.1 that arrangement of the absorption peak positions in the 111μm-thick $npSi$ sample makes it the preferable candidate in the development and design of passive band for MWIR filters.

Figure 4.1(b,c) shows the ground state transmission of $27\mu m$ and $13\mu m$ thick nanoporous silicon membranes. Both thicknesses show fairly similar interference fringes arising due to the multiple light reflections within the samples. It can be also seen that both samples exhibit two absorption peaks at $3\mu m$ and $9\mu m$ corresponding to the molecular vibration of the $Si-OH$ at $3\mu m(3330cm^{1})$ and of $Si-O-Si$ at $9\mu m$ $(1111.11cm^{1})$ stretching modes respectively [81, 84, 183, 184]. Both samples show relatively strong and stable absorption peaks due their high surface area to volume ratio. The thinner samples showed Fabry−Perot interference fringes which can be attributed to the reflections of the probe beam between the front and rear interfaces of the sample, while no fringes observed for the thicker sample.

Following the same procedure above, the ground state transmittance, T_0 of two micro porous silicon samples ($mpSi$) with thicknesses $16\mu m$ and $50\mu m$ were measured as shown in Figure 4.2. It can be seen that both samples show interference fringes similar to those in $13\mu m$ and $27\mu m$ $npSi$-thick samples which attributed to the multiple reflection of light inside the samples. Dissimilar to the $npSi$ samples, the absorption arising from molecular vibrations are either absent or too

weak to measure in the *mpSi* samples. However, both samples show monotonic transmission increase in the wavelength range from $2\mu m$ and $5\mu m$ which is in turn attributed to the diminishing contribution of Rayleigh scattering at longer wavelengths [43].

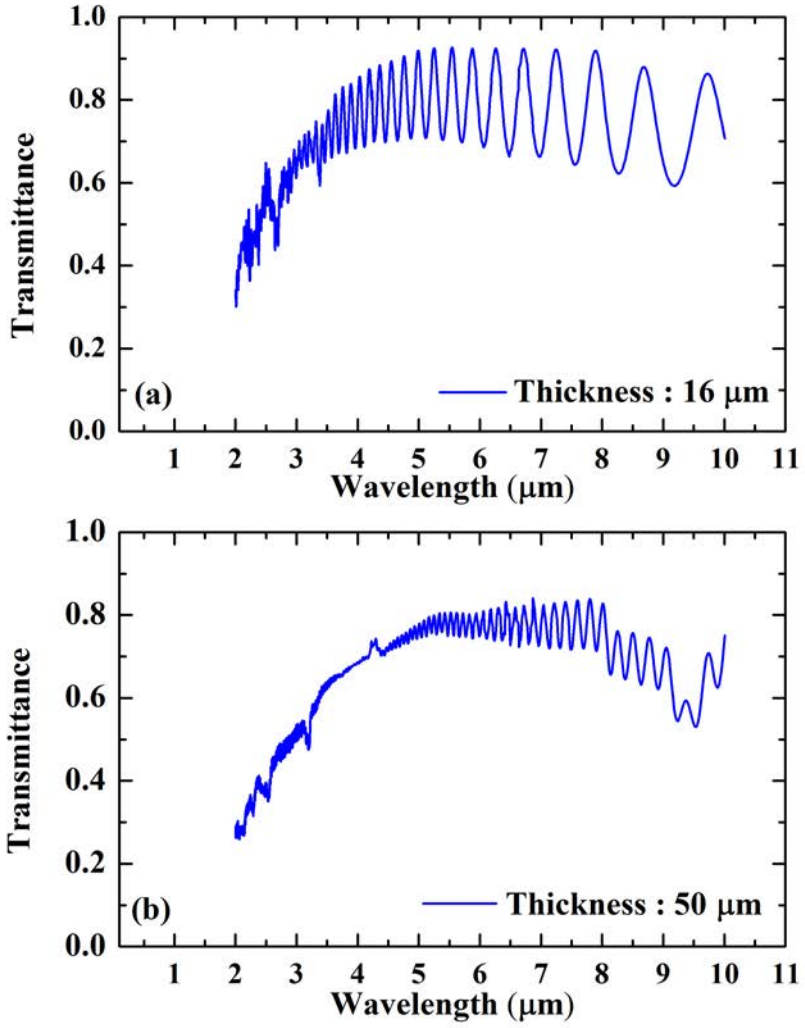

FIGURE 4.2: Background transmittance T_0 for (a) a $16\mu m$ thick *mpSi* membrane(b) a $50\mu m$ thick *mpSi* membrane measured using FTIR spectroscopy. The porosity of both samples is 40%.

In contrast, no transmission increase is seen in *npSi* samples since the pores are much smaller than the wavelengths used here. Both *npSi* and *mpSi* samples show

their highest transmittance windows centered around $4\mu m$. This observation indicates that porosity can be exploited in the design of optical components spectral responses. For example, $mpSi$ attenuates the shorter wave lengths and passes the longer which makes it a potential candidate for long pass filters and optically controlled attenuators [185].

The transparent window of these samples can be modulated based on the generation of the free carriers using an external light source. Here, we discuss the results of these experiments.

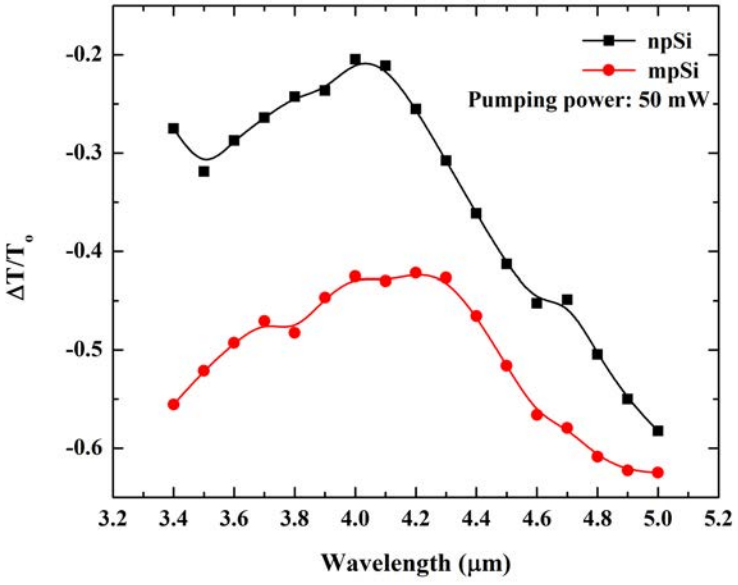

FIGURE 4.3: The transmittance contrast for the 13μm thick npSi (black squares) and for the 16μm-thick mpSi (red circles) as a function of the probe wavelength at the fixed pump power of 50 mW.

To determine the modulation efficiency, the transmittance over the spectral range between 3.4 and $5\mu m$ was recorded at the fixed pump power of $50mW$ and zero delay between the pump and probe, as shown in the Figure 4.3. These results are presented as a modulation contrast, $\Delta T/T_0$, where ΔT is the absolute transmittance change given by $\Delta T = T_p - T_o$, where T_p denotes the transient transmittance at a specific pump power and a fixed delay time. The $mpSi$ samples show stronger modulation at shorter wavelengths, but at wavelengths longer than

$4.4\mu m$ the response of $mpSi$ and $npSi$ converges with reduction in transmission of almost 60%. The enhancement of modulation at longer wavelengths is a well known phenomenon related to the quadratic dependence of free carrier absorption at wavelengths longer than $5\mu m$ [186, 187]. The stronger modulation of the transmission efficiency of $mpSi$ silicon at shorter wavelengths can be attributed to the fact that these samples have lower porosity and, therefore, higher optical density. It has been also shown that the enhancement of the modulation at shorter wavelengths could be due to strong absorption of some vibrational modes such as silicon dioxide (SiO_2)around 3.5μm [188].

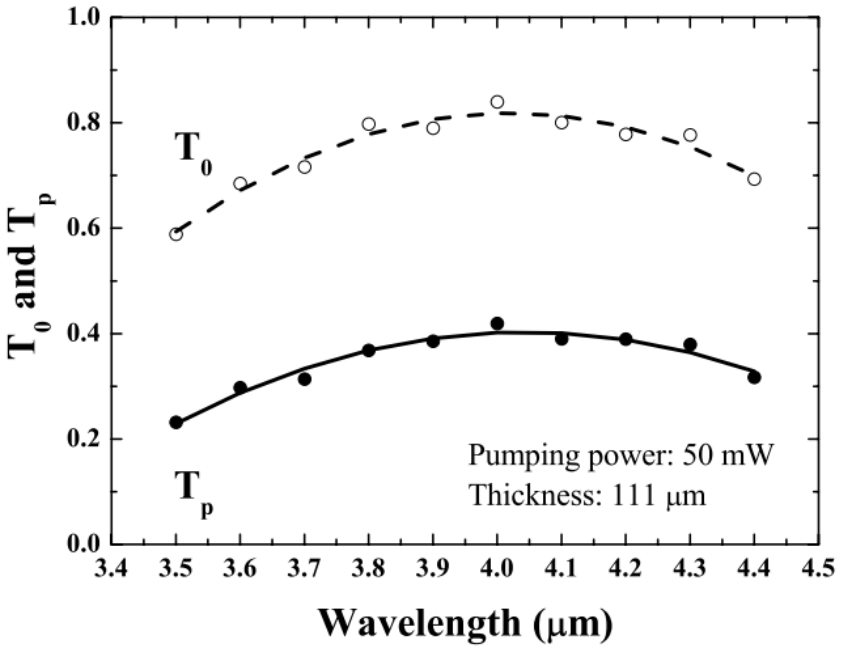

FIGURE 4.4: T_p is the transmittance of the $111\mu m$ thick sample under excitation by the $50mW$ pump as a function of wavelength, measured by the tunable probe beam. The dashed and solid lines are a guide to the eye. T_0 is the transmittance of the probe beam without the pump.

The transmittance spectrum of $npSi$ with thicknes of $111\mu m$ induced by the pump is also measured, as it determines the efficiency of modulation as a function of wavelength. Figure 4.4 shows the spectral dependence of the transmittance at a pump power of $50mW$, covering the wavelength range from 3.5 to $4.4\mu m$, where the transmission fractional change of 50% was observed. Surprisingly, a nearly flat

response of T_p as a function of the wavelength resembles the free carrier absorption spectrum in this wavelength range in doped bulk Si. It is well known that a sharp increase of the absorbance, with nearly quadratic dependence, occurs at the wavelengths longer than $5\mu m$. The sharp absorption mentioned above is preceded by an almost wavelength independant region [186].

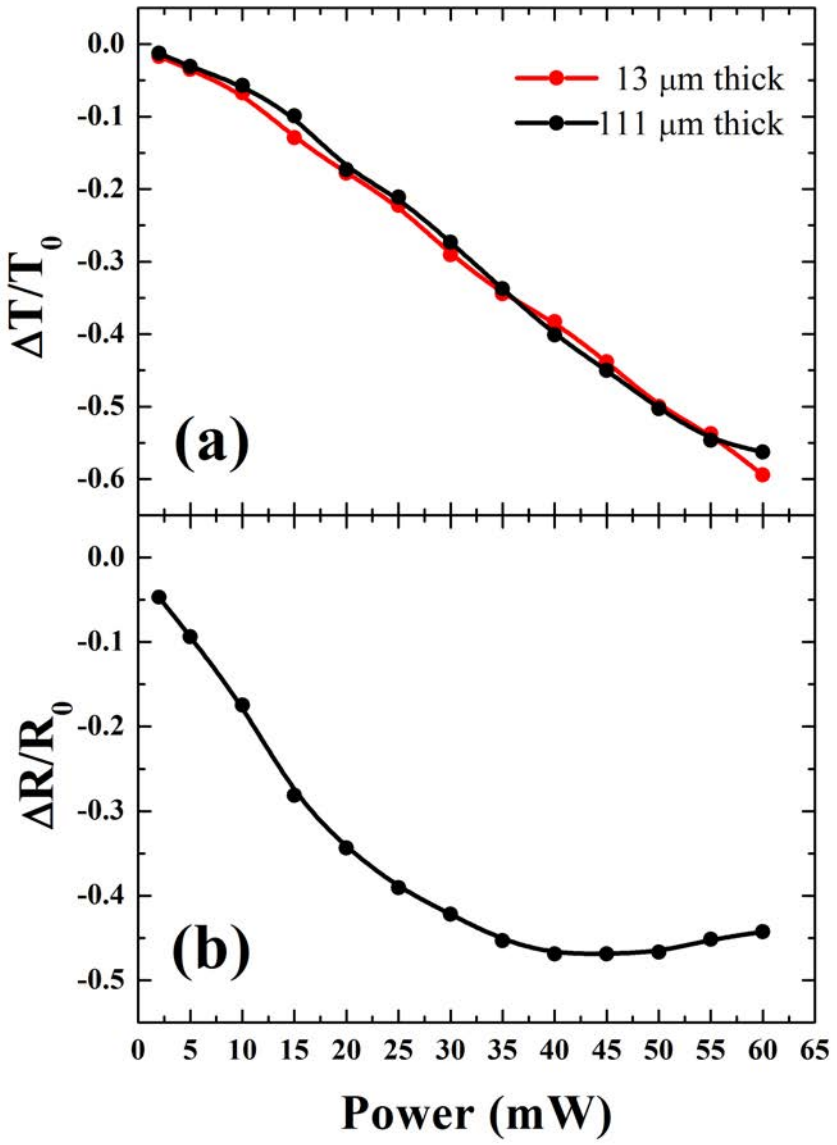

FIGURE 4.5: (a) Transmittance change, $\Delta T/T_0$, for the $4\mu m$ probe measured on the 13 and $111\mu m$ thick nanoporous silicon $npSi$ membranes as a function of the pump beam power. (b) The reflectance change, $\Delta R/R_0$, as a function of the pump beam power at $4\mu m$ probe for the $111\mu m$ thick sample.

4.3 Power Dependence

In this section, we present the fluence dependent reflection and transmission as well as the optical properties of the $npSi$ and $mpSi$ samples. We also present some significant optical parameters related to the afore mentioned samples that were obtained using the optical model. Figure.4.5(a) shows the fractional transmittance change (modulation contrast), $\Delta T/T_0$ (ΔT represents absolute change of the transmittance given by $T_p - T_0$, where T_p is the transient transmittance after the pump excitation), for the 13 and 111μm -thick $npSi$ membranes as a function of the pump power in the range between 2 and 60mW, at a probing wavelength of 4μm , corresponding to the centre of the transparency window, and the 800nm pump. These two thicknesses were chosen to compare the modulation contrast between relatively thin and thick samples. The measurements are obtained just after the zero delay between the pump and probe beams. The change in transmittance shows 1.3% at 2mW and monotonically increases up to nearly 60% at 60mW, corresponding to the range from 0.16 to 4.8mJ/cm^2. Although it was not experimentally tested, the observed trend suggests that even higher modulation could be achieved at higher pumping powers. It is noteworthy that the transmittance change is independent of sample thickness. This observation implies that the active region responsible for the transmittance change induced by the optical excitation occurs at or near the surface region. Indeed, it is known from the previous studies of pSi optical properties that the 800nm pump beam intensity decays by a factor of $1/e$ within the distance of $\sim$ 4.6μm from the surface, which is thinner than both samples [101]. On the other hand, Figure.4.5(b) shows the fractional change of the reflectance, $\Delta R/R_0$, recorded simultaneously with $\Delta T/T_0$ and measured for the thicker membrane. Here we observed an initial strong decrease followed by saturation. This combination of negative changes for both reflectance and transmittance implies that the optically excited membrane became strongly absorptive. The most likely mechanism of 4μm probe signal absorption is interaction with the charge carriers excited by the pump. To examine this suggestion, we derived the experimental optical density, $\alpha_{probe}d$, (where α_{probe} is the absorption coefficient of

the $4\mu m$ probe and d is the sample thickness), using data shown in Figure.4.5(a,b) and separately measured values of the transmittance, T_0, and the reflectance, R_0. The pump -probe reflectance and transmittance are measured using the experimental setup explained in the chapter 3. Here, we give details about the modelling procedures followed to obtain the change in the real and imaginary parts of the dielectric constant. The dielectric function given below by Equation.4.1 is based on the Maxwell-Garnett effective medium approximation modified to include the Drude − optical response of the pump excited charge carriers [187].

$$\epsilon(\omega, N_{eh}) = \epsilon_{Si} + 2p\epsilon_{Si}\frac{1-\epsilon_{Si}}{1+\epsilon_{Si}-p(1-\epsilon_{Si})} - \frac{\omega_{peff}^2}{\omega^2 - \omega_{0eff}^2 - i\omega\Gamma}, \tag{4.1}$$

where

$$\omega_{peff} = \sqrt{1-p}\frac{2\epsilon_{Si}}{\epsilon_{Si}(1+(1-p))+(1-(1-p))}\omega_p, \tag{4.2}$$

and

$$\omega_{0eff}^2 = \frac{1+p}{\epsilon_{Si}(1+p)+(1-p)}, \tag{4.3}$$

$$\omega_p^2 = \frac{N_{eh}e}{m^*\epsilon_0} \tag{4.4}$$

where ϵ_{Si} is the dielectric function of the bulk Si at the ground state, p is the membrane porosity, Γ is the carrier damping rate, ω is the frequency of the probe radiation, ω_{0eff} and ω_{0peff} are the effective resonant and plasma frequencies, respectively, ω_p is the plasma frequency of the free space, N_{eh} is the concentration of the free-carriers on the surface, ϵ_0 is vacuum permittivity, e is electron charge, and m^* is the optical effective mass of 0.17. N_{eh} is assumed to decay along the membrane depth coordinate, z, as $exp(-\alpha_{pump}z)$, where α_{pump} is absorption coefficient of the $800nm$ pump given in the literature [101].

The dielectric function in Equation.4.1 and the frequencies in Equations.4.2 and 4.3 were obtained by following the derivation of equations given by Sihvola [141] which describes the case of isolated metallic particles in a non-conducting medium. Here we investigate an inverse case of non-conductive cavities embedded in a conductive medium. The validity of the obtained expressions was checked at the limits of $p = 0$ and $p = 1$ corresponding to the cases for bulk silicon and air, respectively. The Drude term of in Equation.4.1 includes the damping rate $\Gamma = 3 \times 10^{14} s^1$ which is assumed to be constant as a function of the carrier concentration and the coordinate z. using a linear approximation, the concentration on the surface, at $z = 0$, was calculated according to $N_{eh} = \alpha_{pump} \frac{(1-R_0)F\lambda_{pump}}{\hbar c}$, where F and λ are the pump fluence and the wavelength respectively. The second order process in $npSi$ has a two-photon absorption coefficient of less than $1 cm/GW$. Thus, it can be neglected because over the range of investigated intensities the pump generates through this process almost an order of magnitude lower carrier concentration than in the linear one [189]. However, for the higher pump intensities it needs to be included. With the set of the aforementioned parameters we used Equation.4.1 to calculate the dielectric function and to work out the imaginary part of the refractive index, k, and the absorption coefficient, α_{probe}, given below by Equations.4.5 and 4.6 respectively.

$$k = \frac{1}{\sqrt{2}} \sqrt{\sqrt{(\Re(\epsilon))^2 + (\Im(\epsilon))^2} - \Re(\epsilon)} \tag{4.5}$$

and

$$\alpha_{probe} = \frac{4\pi k}{\lambda_{probe}}, \tag{4.6}$$

The obtained results were iteratively ftted to the experimental data of the optical density gained from the measurements of the reflectance, R, and transmittance, T, using the following relation:

$$T = \frac{(1-R)^2 \exp(-\alpha_{probe} d^*)}{1 - R^2 \exp(-2\alpha_{probe} d^*)} \tag{4.7}$$

where $d^* = d/cos\theta_i$, with θ_i representing the angle of incidence of the probe beam. T and R were determined from the measurements of $T_0 = 0.80$ and $R_0 = 0.13$, and with $\Delta R/R_0$ and $\Delta T/T_0$ obtained in the pump probe measurements.

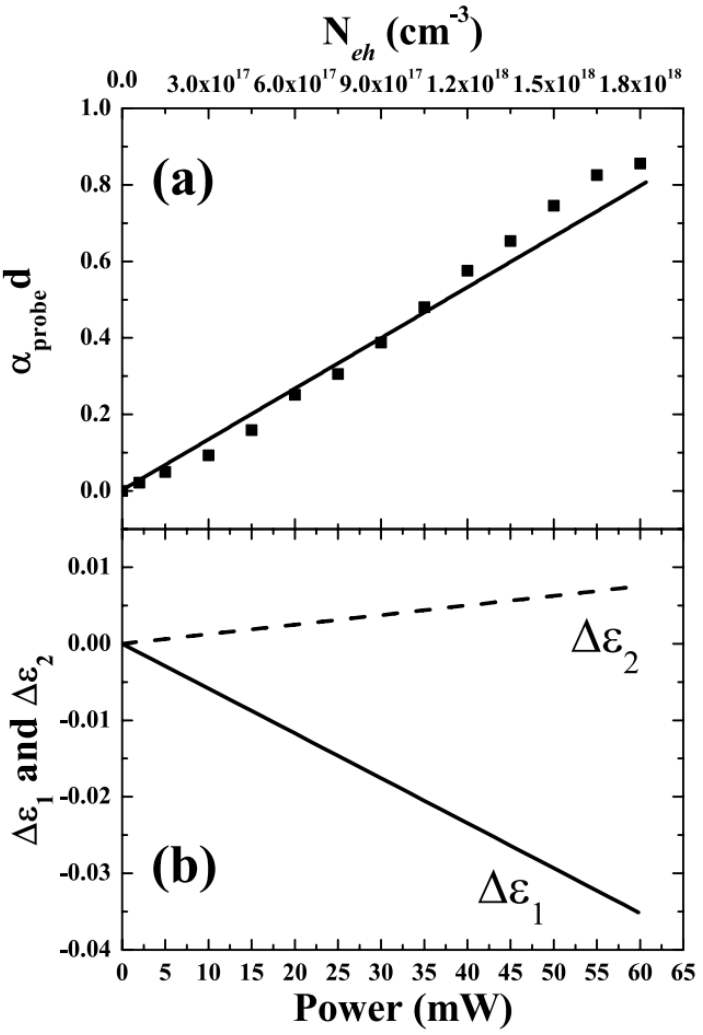

FIGURE 4.6: (a) The experimentally determined (black squares) and calculated (solid line) optical density, $\alpha_{probe}d$, of the $4\mu m$ probe as a function of the pump power. (b) The real and imaginary parts, $\Delta\epsilon_1$ and $\Delta\epsilon_2$, respectively, of the dielectric function changes as a function of the pump power. The corresponding excited carrier concentration, N_{eh}, is also displayed on the upper x-axis on the top panel.

The experimentally estimated optical density (dotted data) is shown in Fig. 6(a). To get more insight into the physics underlying the observed modulation and to retrieve quantitative information about the excited charge carriers, we modelled the optical response of the $111\mu m$ thick $npSi$ membrane, namely its real and imaginary parts of the dielectric function, using the Maxwell-Garnett model, modifed to include optical response of the excited charge carrier described by the Drude theory as illustrated in the above equations. The estimated changes in the dielectric function are presented in Figure.4.6(b) as a function of the pump power. It has been shown previously [101] that the Drude theory provides a good approximation and can be used to estimate the excited charge carrier concentration, N_{eh}, and the damping rate, Γ. We note that the estimate of phenomenological Γ does not directly reveal the nature of the charge carrier scattering process and we have left this out of the arguments in this work. Our purpose here is to provide an acceptable estimate of the carrier concentration, N_{eh}, and the damping rate, Γ. Under assumption that the number of the excited free carriers linearly depend on the pumping power, the excited carrier concentration, was calculated using the fluence, F, corresponding to the each pump power at $4\mu m$ probe beam wavelength (see Methods illustrated in the previous sections), and is also displayed on the upper x-axis on the top panel. Figure.4.6(a) shows that calculations assuming the linear dependence on pumping power, and keeping the damping rate, Γ, constant at the value of $3 \times 10^{14} s^1$, provide a reasonable agreement with the experimentally determined optical density.

The calculated free-carrier density on the samples surface spans between 6×10^{16} and $1.8 \times 10^{18} cm^3$ for the average pulse power range covering values from 2 to $60mW$. This procedure confirms that, immediately after the excitation, the change of optical response in band around $4\mu m$ can be explained by the contribution from the excited free charge carriers.

Using the same experimental setup, the transmittance (upper panel)and reflectance (lower panel)changes of the $27\mu m$- thick $npSi$ as a function of the excitation power ranging from $2 - 50mW$ are also measured and compared with $13\mu m$-thick $npSi$

membranes at probe wavelength of $4\mu m$, and the related experimental data are shown in the Figure 4.7.

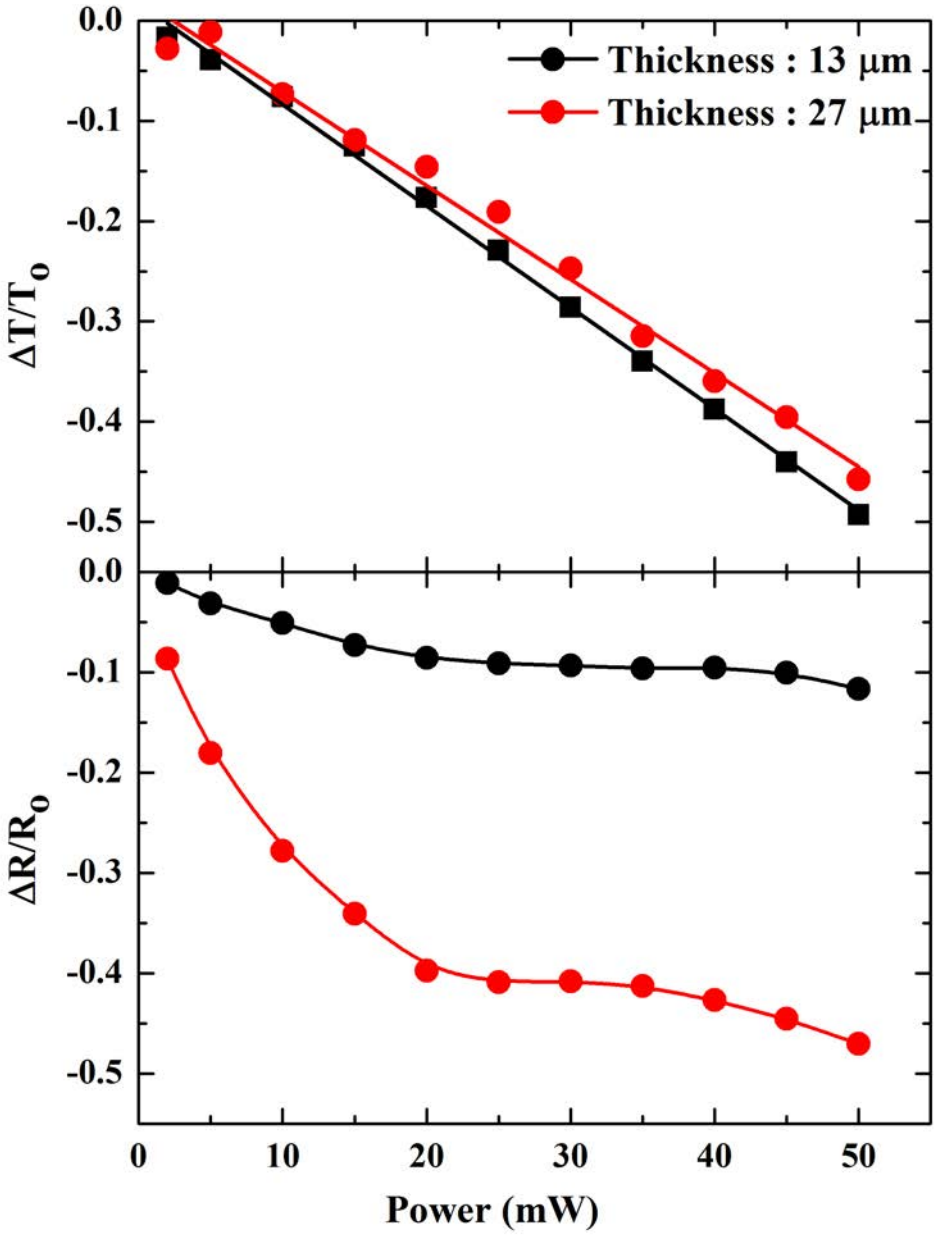

FIGURE 4.7: The transmittance change of $13\mu m$-thick (black squares) and $27\mu m$-thick (red circles)$npSi$ membranes as function of excitation power ranging from $2-50mW$ at probe wavelength of $4\mu m$ corresponding to the center of the transparent window shown in the $FTIR$ section.

It can be seen from the figure that the transmittance change for all $npSi$ thicknesses shown in the Figures.4.5 and 4.7 are almost comparable with each others. Both samples in this figure showed low modulation depth at powers less than $5mW$ with monotonic increase up to 50% at $50mW$ pump power. Similar to what we observed in the Figure.4.5, the observed transmittance responses are thickness independent parameter, which implies that the absorption of the probe signal $4\mu m$ occurs at excited region near the sample surface. This can be also explained via the penetration depth of our pump pulse $800nm$ which is around $4.6\mu m$ where the pump intensity decays by $1/e$. The transmittance change of $13\mu m$ is plotted in the figure above for the sake of change comparison between both thicknesses. The lower panel of the figure 4.7 shows the reflectance change of both $13\mu m$ and $27\mu m$ $npSi$ as a function of pump power ranging from 2 to $50mW$ corresponding to fluence range from 0.16 to $4.01mJ/cm^2$. It has been shown that the reflectance change $\Delta R/R_0$ is proportional to the total number of the carriers near the excited region of the surface, which in this case corresponds to the penetration depth of the pump beam of $4.6\mu m$ expressed as $= \lambda/4\pi|n|$, where n is the complex refractive index of the sample. Thus, monitoring the reflectance change provides a good insight regrading the evolution of the carriers near the sample surface [80, 190]. It can be clearly seen from the figure that the reflectance change for both samples are different from each other where the $27\mu m$ membrane showed bigger change comparing to the thin sample. The thinner sample showed strong drop from 2% at $2mW$ to around 8% at excitation power of $20mW$ followed by saturation and relatively small drop at pump powers exceeding $40mW$. On the other hand, the $27\mu m$- thick membrane showed 8% reflectance change at $2mW$ power while at higher pump powers of $20mW$ the reflectance changes reaches 40% followed by saturation in the pump power range from 20 to $40mW$ and relative drop at powers greater than $40mW$. The significant difference between the reflectance change for both thicknesses compared to that shown with transmittance change indicates that the excited region near the surface of the sample is responsible for induced change in both thicknesses.

For the purpose of comparison between the $npSi$ and $mpSi$, the capability of controlling the transmittance change (contrast depth) for $mpSi$ at different pump excitations is also assessed. Figure.4.8. shows transmittance changes for $16\mu m$-thick $mpSi$ membrane as function of pump power ranging from 2 to $70mW$ corresponding to fluence range from 0.16 to $5.6mJ/cm^2$ at $4\mu m$ and $5\mu m$ probe wavelengths respectively. It can be seen from the figure that the transmittance change at $4\mu m$ probe wavelength gradually decreases with increasing the excitation power reaching modulation depth of about 30% at $40mW$ excitation power, while at $5\mu m$ probe wavelength the $mpSi$ sample shows almost linear drop at pump powers less than $40mW$ corresponding to modulation depth of about 70% followed by saturation at higher pump powers.

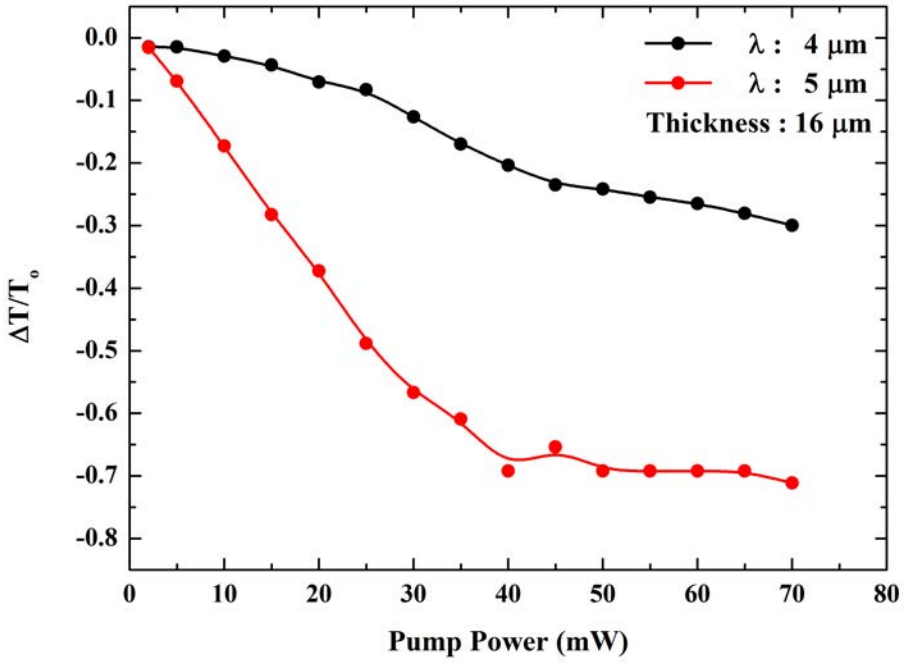

FIGURE 4.8: The modulation contrast (transmittance change) for $16\mu m$ microporous silicon ($mpSi$) sample as a function pump excitation at $4\mu m$ and $5\mu m$ probe wavelengths respectively.

Likewise, the modulation contrast of the $50\mu m$-thick $mpSi$ is also evaluated as a function of optical excitation and different probe wavelengths as it shown in the Figure.4.9. It can be clearly seen that the modulation contrast enhances at longer

probe wavelength where at $5\mu m$ the greater transmittance change is observed. Similar to the thinner $mpSi$ sample, the transmittance change also saturates at higher pump powers. In general, both $16\mu m$ and $50\mu m$ $mpSi$ samples have shown the same trends where the transmittance change drops at lower pump powers and flatten or saturates at higher excitations. The deeper modulation depth observed at longer probe wavelengths for both thicknesses can be attributed to the well known fact related to the nearly quadratic dependence of free carrier absorption at probe wavelengths longer than $5\mu m$ [186, 187].

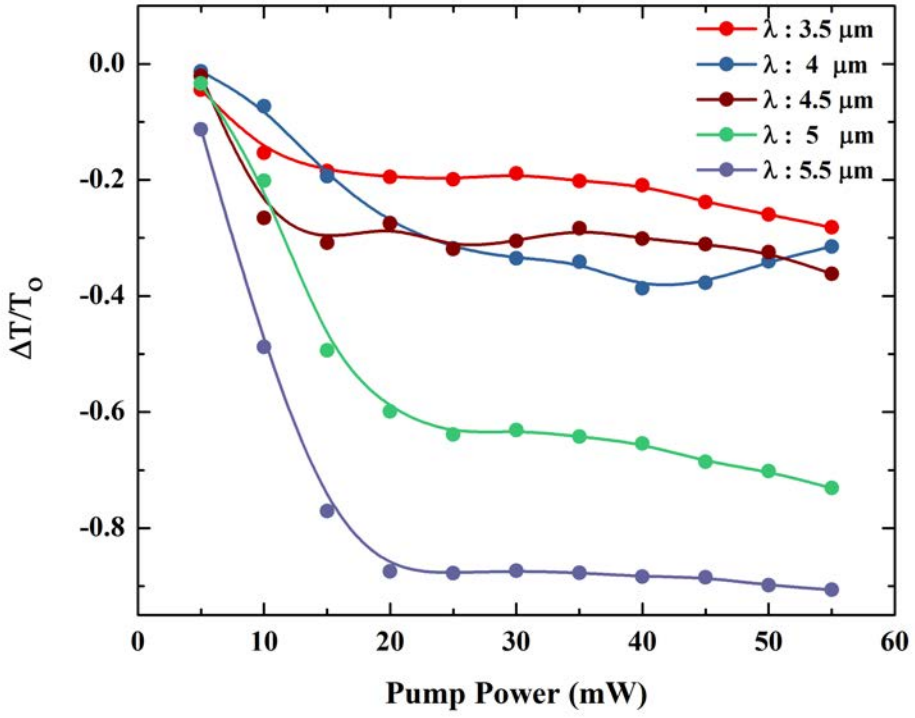

FIGURE 4.9: The reflectance change for $50\mu m$ microporous silicon ($mpSi$) sample as a function pump excitation at $4\mu m$ and $5\mu m$ probe wavelengths respectively.

Following the same procedures, the reflectance change of the $16\mu m$- thick $mpSi$ sample is also measured as it can be seen from the Figure.4.10. The measurements are obtained simultaneously with the transmittance change shown in the Figure.4.8 and the data recorded over the same range of the excitation powers and at the same probe wavelengths. It can be seen from the figure that the $16\mu m$

sample shows bipolar reflectivity modulation which can be attributed to the transient dynamic of the electron-hole plasma and its related interband and intraband contributions to the dielectric function. The reflectance change gradually drops at lower excitation power and shows a dip around $25mW$ excitation power followed by gradual reflectance increase towards the reverse reflectance polarity. In general, The $16\mu m$ $mpSi$ sample shows deeper modulation at probe wavelength of $5\mu m$ compared to that shown for $4\mu m$ probe wavelength. In particular, the reflectivity dip observed for both wavelengths can be attributed to the optically driven semiconductor to conductor (metal like) transition at which the bulk electron -hole plasma frequency passes over the frequency of the probing MWIR signal. The subsequent reflectance increase following the dip can be attributed to intraband electronic transition for highly ionized materials.

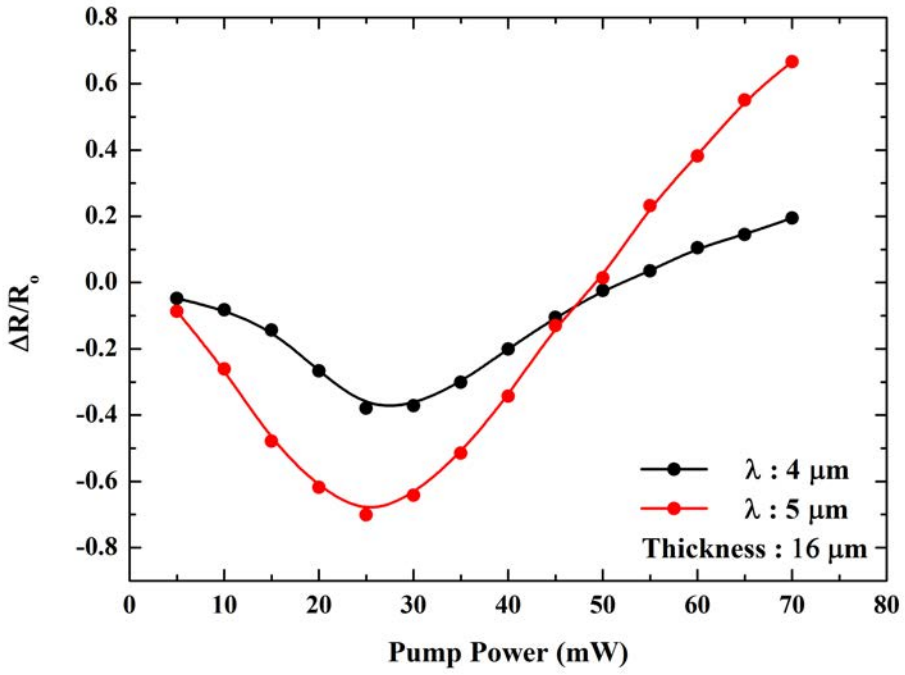

FIGURE 4.10: The reflectance change for $16\mu m$ microporous silicon ($mpSi$) sample as a function pump excitation at $4\mu m$ and $5\mu m$ probe wavelengths respectively.

In the case of silicon and other materials [63, 76, 162, 191–194], many previous studies related the same reflectivity trend to the isotropic renormalisation of their

direct band gap driven by strong prompt electron-hole plasma, leading to strong enhancement of the interband transition.

4.4 Modulation Speed

In order to evaluate and compare the modulation speed the rise and decay times for each structure ($npSi$ and $mpSi$) needs to be examined. Figure 4.11. shows the transmittance change for $111\mu m$- thick nano-porous silicon structures as a function of time delay between the pump and probe at the fixed $4.0\mu m$ probe wavelength and $50mW$ pump power. It can be seen that the rise time is as fast as the sub-picosecond resolution of the measurements. Such a fast response provides additional support to our suggestion that the optical response is governed by the free carriers excitation.

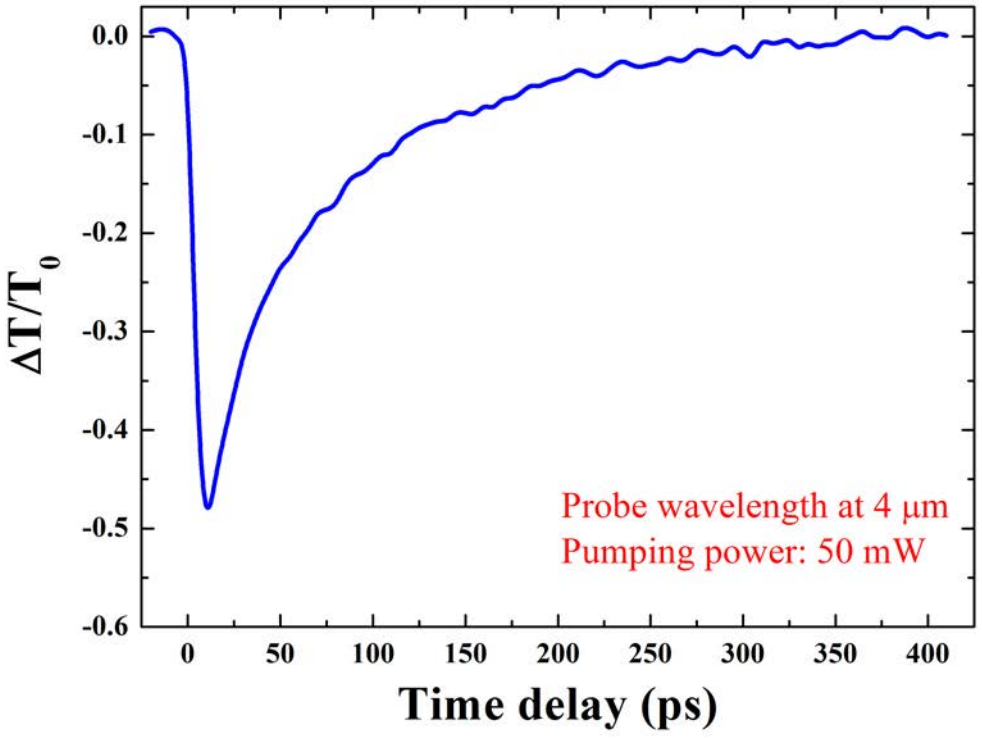

FIGURE 4.11: Time-resolved transmission change, $\Delta T/T_o$, at the probe beam wavelength of $4\mu m$ and the pump power of $50mW$.

On the other hand, the decay time at which the intensity of the transmission change drops by a factor of 1/e was 66ps. Thus, $npSi$ has the potential to operate at 15GHz modulation speed in spectrum filtering devices. Although the exact mechanism of the carrier concentration decay remains debatable, we compare our result to those ultrafast measurements published previously. It should mentioned here that the carrier dynamics and the related recombination dynmics will be introduced in the next chapter. Our findings are rather similar to the works which estimated a fast component of 100ps attributed to the bimolecular recombination [195, 196]. Yet, an additional slow microsecond long component observed there and attributed to the radiative recombination involving surface states is absent in our work, because its excitation requires a pump with the wavelength shorter than 800 nm.

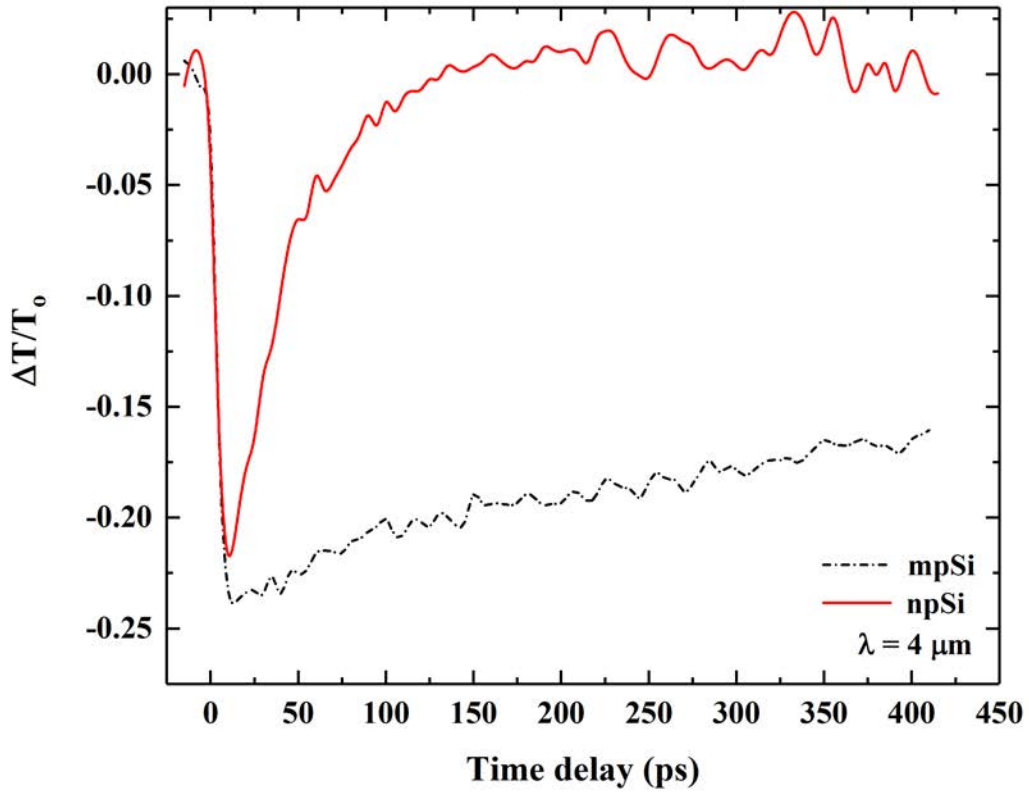

FIGURE 4.12: Transmittance change, $\Delta T/T_o$, as a function of delay time between the pump and probe for 13μm-thick $npSi$ (red solid line) and 16μm-thick $mpSi$ (black dash dotted) at the fixed probe wavelength wavelength of 4μm and the pump pulse excitation power of 50mW.

On the other hand, the fast decay of $1ps$ shown elsewhere [8, 197] was not present in any of our measurement. In cited works the fast component was attributed to the carrier trapping by dangling bond states. In our work the dangling bonds are not likely to have such important impact as the samples are passivated by oxides and hydroxides molecules. Most of the data in this section are transmittance related measurements as a function of time delay between the pump and probe signal at fixed pump power as it is significantly important in optical modulators investigation.

In order to evaluate and compare the modulation speed, the rise and decay times for each structure ($npSi$ and $mpSi$) need to be examined. The comparison is made here between the above mentioned samples as they are close to each other in terms of sample thickness. Figure. 4.12. shows the transmittance change for micro- and nano-porous silicon structures as a function of time delay between the pump and probe at the fixed $4\mu m$ probe wavelength and $50mW$ pump power. It is apparent that the rise time for both types of structures is nearly immediate from the time of application of the pump pulse, which supports our assumption that the main optical response is dominated by free carriers excitation. The decay time, determined by the transmission intensity drop by a factor of $1/e$, is as short as a few tens of picoseconds for $npSi$ allowing to use it for modulators with GHz modulation frequency. On the other hand, $mpSi$ shows a much slower rate of recovery which can be as slow as tens of nanoseconds. While the observed decay for $mpSi$ is quite typical, strongly resembling the bulk, the process in $npSi$ is much faster than one would expect for a silicon derivative material. Yet, it is known that in silicon crystals approaching nanometric dimensions, the recombination process of the free carriers at concentration higher than $10^{18}cm^3$ is governed by Auger recombination which can be as fast as just a few picoseconds. In porous silicon samples the surface-to-volume ratio is rather large and the vast amount of surface states may participate in the recombination via impurity assisted Auger process [198].

4.5 Summary

The performance of nanopororous and microporous silicon membrane samples for use as an active component for electro-optical light modulators in MWIR range is compared and evaluated. The measurements revealed that the spectral features of the membranes depend on the porosity, pores and skeleton dimensions. We demonstrated that microporous silicon with submicron size of the pores affects light transmission at the shorter wavelengths because of scattering, while nanoporous silicon shows distinctive absorption bands corresponding to impurities at surface of the pores. The pump-probe time-resolved experiments demonstrated that the response of npSi fast enough to allow its use in fast modulators operating in GHz range. Nevertheless, both forms of device are almost 90% transparent in the ground state, but can block 60% of incident light in the infrared when optically pumped at fluences of less than 5mJ/cm2. In addition, we observe the phenomenon of the electron-hole plasma resonance at which the sample of mpSi becomes optically similar to a metal. At the resonance the sample became more reflective as its dielectric function becomes negative. We envisage that the plasma resonance can be used in the design of all optical modulators made of semiconducting materials.

Chapter 5

Transient Optical properties of the Structured Silicon Membranes

5.1 Introduction

The decay dynamics of the photo-excited electrons in semiconductors have been of a great interest for an improvement in optoelectronic performance of photovoltaic and photo-emission devices. For photovoltaic devices, the photo-excited electrons should be extracted into the electrode before recombination, so slow decay is essential for high efficiency [199–201], whereas conversely, fast relaxation into the conduction band minimum is important for photoemission devices to achieve a narrow emission band [202, 203]. In general, the relaxation procees in semiconductors encompasses various overlapped temporal stages ranging from fraction of picosecond to around millisecond for indirect semiconductors such as silicon. These relaxation process can be revealed based on recent femtosecond laser technology which provides a deep understanding of the carrier generation and related relaxation process of the excited semiconductor [53]. The quantum confinement effects in a nanoscale regime induce different electron decay mechanisms from the

bulk counterpart, e.g., phonon bottleneck effect [204–206]. The reduction of the semiconductor dimensions also causes the increase not only in the band gap but also in the surface-to-volume ratio, which can induce the surface-trap states within the band gap acting as another decay channel.

Therefore, it is required to understand these decay mechanisms to realize the high performance of optoelectronic devices. Since the observation of visible photoluminescence (PL) in porous silicon [89], it has been considered as a material for optoelectronics even though the indirect band gap of bulk Si causes inefficient emission and absorption of photons. It is known that porous Si contains oxygen-related passivation on a large surface area, which affects the electronic structure and the decay mechanism of the photo-excited electron [81, 207, 208]. So, the control capability of the decay mechanism in porous Si is essential to achieve high performance of Si-based optoelectronics. In fact, the origin of the visible photoluminescence still remains debatable due to the lack in the information about carrier relaxation at early stages following the excitation.

In this chapter, we present the experimentally obtained data for both microporous ($mpSi$) and nanoporous ($npSi$) silicon respectively. The transient optical reflectance and transmittance changes of the $16\mu m$-thick $mpSi$ as a function of the time delay between the pump and probe signals at different excitation levels are presented at $4\mu m$ probe wavelengths. Following this, we introduce some calculation regarding the recombination process of the $16\mu m$-thick $mpSi$ at different excitations. On the other hand, same optical setup is used to measure the reflectance and transmittance changes of the $npSi$ sample with thickness of $111\mu m$ as a function of the pump power and different probe wavelengths. The recombination time based fitting is applied to extract the recombination times of the different processes following the excitation of $npSi$ sample which provides an insight about the carrier recombination dynamics.

5.2 Transient optical properties of the Microporous Silicon (mpSi)

In order to evaluate the carrier dynamics of the 16μm-thick $mpSi$ and how the generated carriers evolve in time, we used the optical pump-mid IR probe technique to monitor the reflectance and transmittance changes as a function of the time delay between the pump and probe signals at 4μm probe wavelength and different excitation levels. The data obtained provide information about the possibility of controlling the transmittance contrast of $mpSi$ which is significantly important in the fabrication and design of the optically modulated devices.

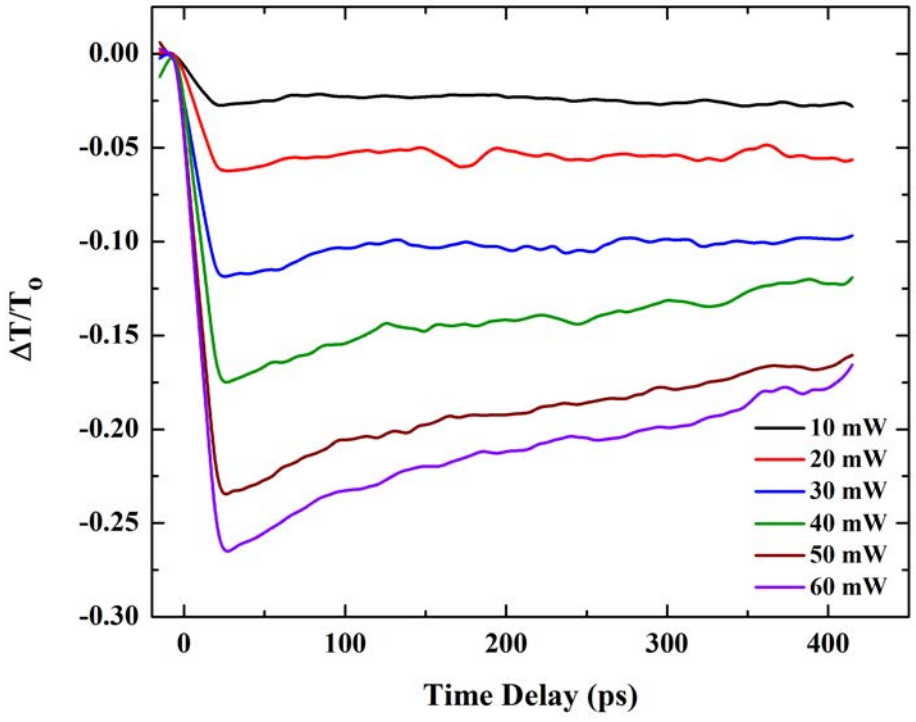

FIGURE 5.1: The transient transmittance change for 16μm- thick microporous silicon membrane $mpSi$ as a function of delay time between pump and probe signals at different pump levels and 4μm probe wavelength.

Figure.5.1 shows the transmittance change for $mpSi$ membrane as a function of the delay time between the pump and probe signals and pump power in the range

between 10 and $60mW$ (corresponding to the fluence range of $0.8-4.8mJ/cm^2$). It can be clearly seen that the transmittance contrast is a power dependant parameter that increases with excitation fluence. It can be seen from the figure that the transmittance contrast increases with pump fluence which indicates the possibility of changing modulation depth by controlling the pump fluence. It can be also seen that there is a weak dependence of the recovery time on the pump fluence. The recombination is slower at lower excitation levels while it gets faster at the higher pump fluencies. This observation indicates that the Auger process is present in mpSi as well, but it is much weaker and less significant to achieve the fast recombination times observed in *npSi* and discussed in chapter 4.

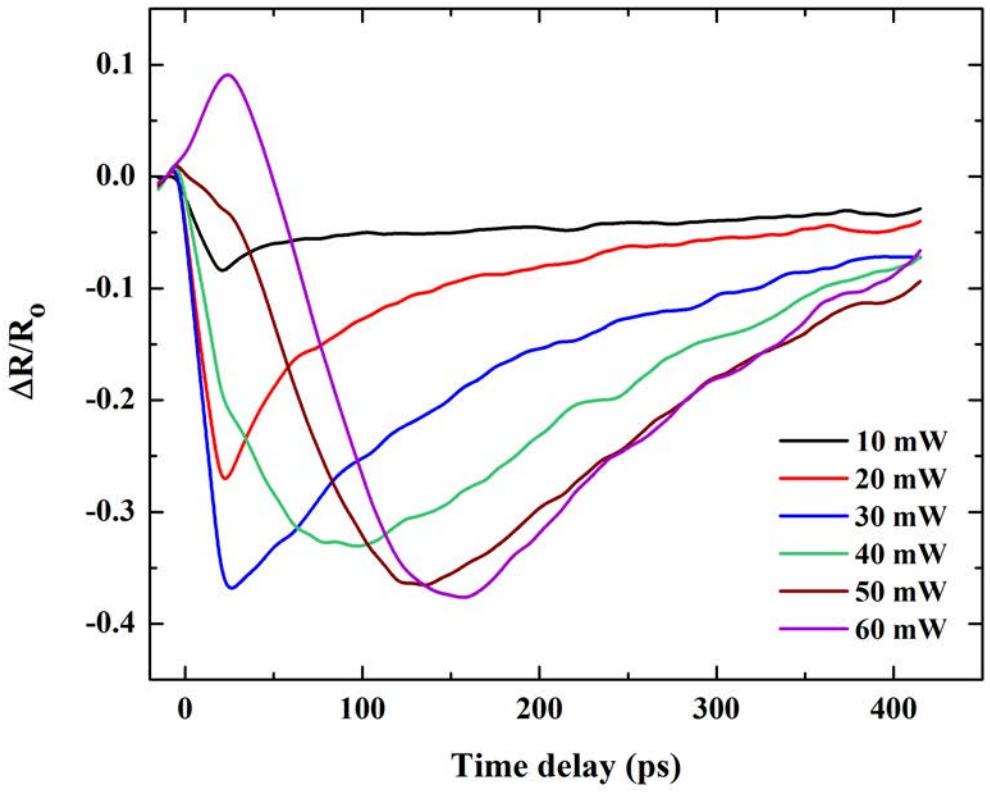

FIGURE 5.2: The transient reflectance change for $16\mu m$- thick microporous silicon membrane *mpSi* as a function of delay time between pump and probe signals at different pump levels and $4\mu m$ probe wavelength.

Similarly, the reflectance change of the same sample thickness is also measured as

a function of the delay time between the pump and probe signal covering the same pump fluences at $4\mu m$ probe wavelength as it shown in the Figure.5.2. Although the transmittance decay is rather monotonic and is roughly proportional to the carrier concentration decay, the reflectance response is more complex. It can be seen from the figure that at the lower pump powers, the reflectance drops and slowly recovers back. As the intensity increases the drop intensifies, but at higher pump levels, above $50mW$, the reflectance initial increases followed by the drop. This peculiar pattern indicates that the carrier concentration is sufficient to achieve the electron-hole plasma resonance condition. Here, the presence of the charge carriers excited by the pump modify the dielectric function of the silicon skeleton to such an extent that it becomes negative and its absolute value is similar to that of the holes, i.e air.[187].

5.3 Recombination dynamics of the Micro-porous Silicon (mpSi)

In order to understand the dynamic of the photo generated carriers and related recombination processes in the microporous silicon sample $mpSi$, the decay rate based on the initial carrier concentration method is used. As mentioned in the previous section that the carrier recombination is slow at early excitation levels while gets faster at higher excitations. In order to reveal the underpinning dynamic, the simple decay rate equation is employed as follows:

$$-\frac{dN_{eh}(t)}{dt} = aN_{eh}(t) + bN_{eh}^2(t) + cN_{eh}^3 \tag{5.1}$$

$$-\frac{dN_{eh}(t)}{dt} = -\frac{dN_{eh}(t)}{d(\Delta T/T)}\frac{d(\Delta T/T)}{dt} \tag{5.2}$$

The first linear term on the right hand side of the equation 5.1 represents the ShockleyReadHall (SRH)which can be attributed to deep energy level recombination or defects[209]. The localized state in this type of recombination process involves not only energy absorption but also takes the differences in momentum [209]. This process can be considered as a quite dominant recombination process in the indirect semiconductors. The bimolecular term (the second term in the equation)is either band to band or trap assisted Auger ionization[210]. The band to band recombination could be either radiative or non-radiative type. The radiative recombination is ignored here since there is no luminescence observed, while in the non-radiative case the electrons in the silicon and silicon derivative materials take much longer time to fully recombine. The third term in the equation refers to the Auger recombination process where energy released from the electron hole recombination is given to another electron. Based on the above equation, both the type of recombination as well as the recombination coefficient can be obtained. Here, equation 5.2 is employed to calculate the decay rate from the experimental data. To begin with, the term $d(\Delta T/T_o)/dt$ can be extracted from fitting the transmittance changes shown in the Figure.5.1. The fitting covers few tens of picoseconds after the zero delay between the pump and probe signals. The slope of the fitted line represent the second part of the equation 5.2. While the first part can be extracted from the model which will be introduced in the later paragraphs. The first step involves obtaining the transient carrier concentration at different pumping powers. The Maxwell Garnett model together with transfer matrix method are used to simulate the transmittance change as a function of the time delay between the pump and probe beams at different pumping powers. The extracted carrier concentrations as a function of time delay obtained from the model are presented in the figure 5.3.

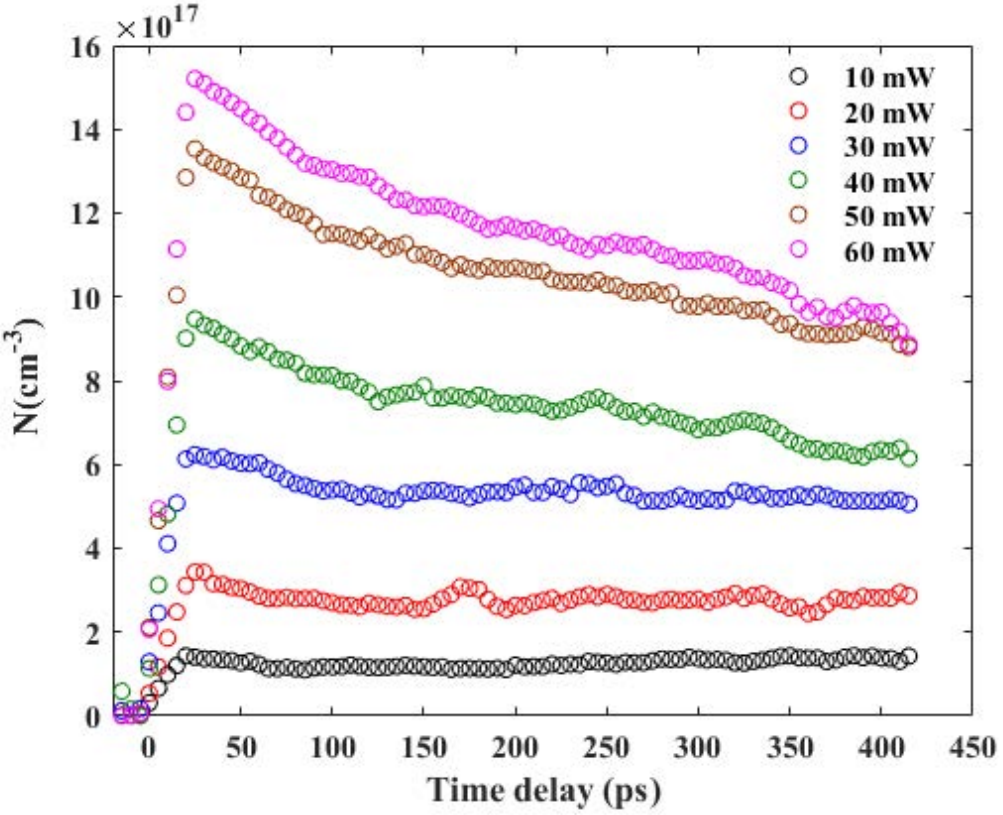

FIGURE 5.3: The transient carrier concentration for $16\mu m$- thick microporous silicon membrane $mpSi$ as a function of delay time between pump and probe signals at different pump levels and $4\mu m$ probe wavelength. The figure is simulated using Maxwell Garnett model modified to include Drude like contribution.

The model used to simulate the data (Maxwell Garnett model) is modified to include the contribution of the free carriers by incorporating Drude model which is expressed as follows:

$$\epsilon = \epsilon^0_{eff} - \frac{\omega_p^2}{\omega^2 + i\Gamma\omega} \tag{5.3}$$

Here, ω is the probing frequency, ω_p is the plasma frequency and Γ is scattering rate. The plasma frequency is expressed as follows:

$$\omega_p^2 = \frac{e^2 N^2}{\epsilon_0 m^* m_e} \tag{5.4}$$

Where,N is the carrier concentration, m^* and m_e are the effective and electron masses and e is the electron charge. It can be seen from the equation above that the change in the plasma frequency ω_p and the scattering rate can significantly influence the effective dielectric function of the sample. This procedure allows the influence of the excitation to be taken in the consideration through incorporating the plasma frequency and carrier concentration. In our simulation, plasma frequency is employed as fitting parameters to obtain the corresponding carrier concentration from the transmittance change.

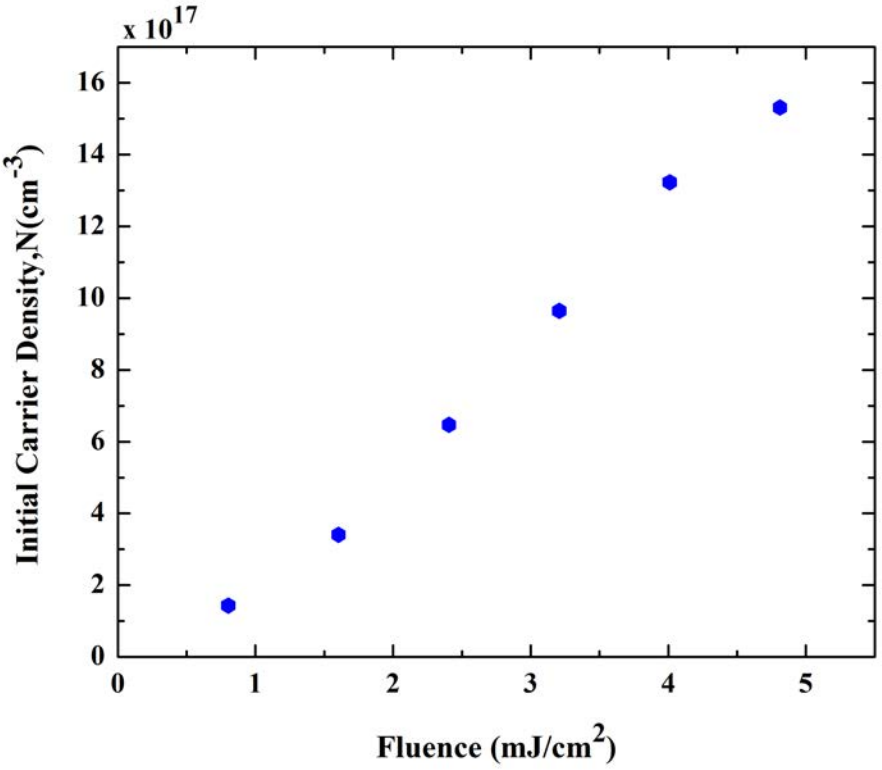

FIGURE 5.4: The power dependence carrier concentration extracted from the Figure.5.3 which corresponds to the maximum transmittance change observed in the Figure.5.1 in the previous section.

The effective scattering rate was fixed at $100fs$ which is taken over a time scale of interest from the ref [211]. Figure.5.3 shows the transient carrier concentration for $16\mu m$- thick microporous silicon membrane $mpSi$ as a function of delay time between pump and probe signals at different pump levels and $4\mu m$ probe wavelength. It can be seen from the figure that the population of generated carriers

almost linearly increases with increasing the excitation fluence. It can be also seen that the carrier recombination time is fluence independent parameter.

Figure.5.4 shows the fluence dependence carrier concentrations extracted from the Figure.5.3 which corresponds to the maximum transmittance change observed in the Figure.5.1. It can be seen from the figure that the carrier concentration is almost in linear relation with pump fluence. The carrier concentration is plotted in such way for the purpose of extracting the first term of the equation 5.1. Moreover, the same carrier concentration is used to extract the second term of the middle part of the same equation. The procedure related to the both parts of the equation 5.2 is explained in details in following paragraphs.

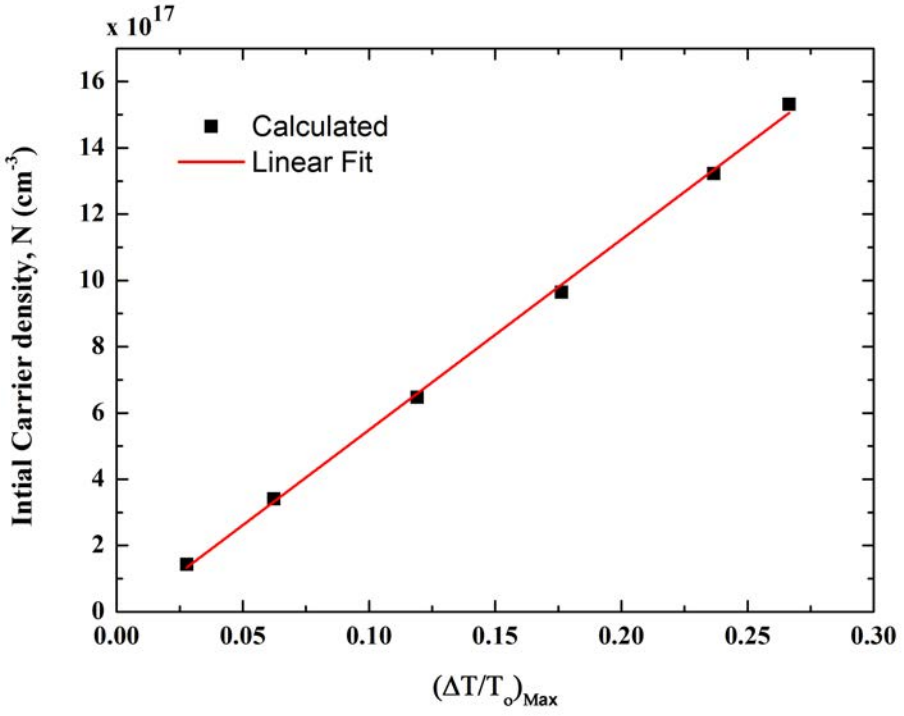

FIGURE 5.5: The initial carrier concentration as a function of maximum transmittance change. The resulted slope of the plot represents the first term in the middle part of the equation 5.1.

In order to obtain the first term of the equation 5.2, the initial carrier concentration is plotted against the maximum transmittance change as it is shown the Figure.5.5. It can be seen from the figure that the carrier concentrations linearly increase with

increasing the transmittance change indicating the proportional relation between the transmittance change and generated carriers. The slope of the resulted plot represents the first term of the equation 5.2.

The second term of the equation 5.2 can be extracted from the time resolved measurements shown in the Figure.5.1. As it mentioned previously, this can be done by taking the slop of the transmittance change around the zero delay for a few tens of time delays between the pump and probe signals.

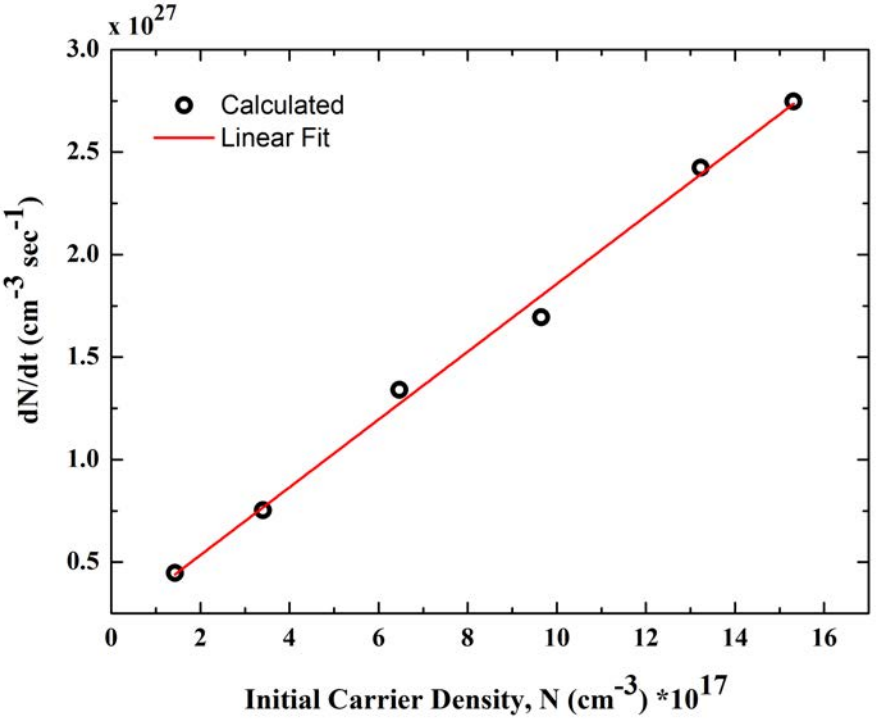

FIGURE 5.6: The recombination rate as a function of initial carrier concentration. The black circles represent the data calculated from the experimental measurements while the red line refers to the linear fit to determine the recombination coefficient.

Figure.5.6. shows the recombination rate as a function of initial carrier concentration. The black circles represent the data calculated from the experimental measurements while the red line refers to the linear fit to determine the recombination coefficient. It can be seen from the figure that the recombination rate exhibits linear relation with the initial carrier concentration. This indicates that the generated carriers by the pump in the $16\mu m$ thick $mpSi$ sample follow ShockleyReadHall

(SRH) type recombination. This type of of recombination is mainly attributed to the recombination via deep energy levels which is in fact dominant recombination process in silicon and other indirect bandgap semiconductor materials as it absorbs the difference in the carriers momentum [209]. The linear relation also indicates that the one order rate equation is sufficient to describe the recombination process in the sample. The (SRH) recombination coeffecient of the sample was found to be $1.65 \times 10^9\ s^{-1}$ corressponding to the carrier life time of about $606ps$. The life time obtained here is relatevily longer that obtained in other published works[212]. In our previous publication [198], the SRH coefficient, for nanocrystalline silicon embedded in hydrogenated amorphous silicon, is significantly higher compared to the coefficient obtained here. The later study attributed the higher SRH coefficient to the high density of defects and as a results higher corresponding states occupying the Urbach tail of the host material.

5.4 Transient optical properties of the Nano-porous Silicon

This section, evaluates the carrier recombination dynamics of 111μm-thick $npSi$ following the optical excitation. Here, The time resolved optical pump-Mid IR probe have been used to measure the reflectance and transmittance changes as a function of time delay between the pump and probe signals. The $npSi$ sample used in this section is $111\mu m$ thick with porosity of 71% estimated using gravimetric analysis. Since the $npSi$ samples shows much faster recombination time comparing to $mpSi$, the time resolved reflection and transmission changes as a function of time delay between the pump and probe signals at different probe fluences ranging from 0 to $2.5mJ/cm^2$ is measured first. The measurements were obtained at $4mJ/cm^2$ excitation power as it is shown in the Figure.5.7(a,b). It can be seen from the figure that the change in both reflectance and the transmittance is immediate reaching the minimum within a few picoseconds.This can be attributed to the absorption

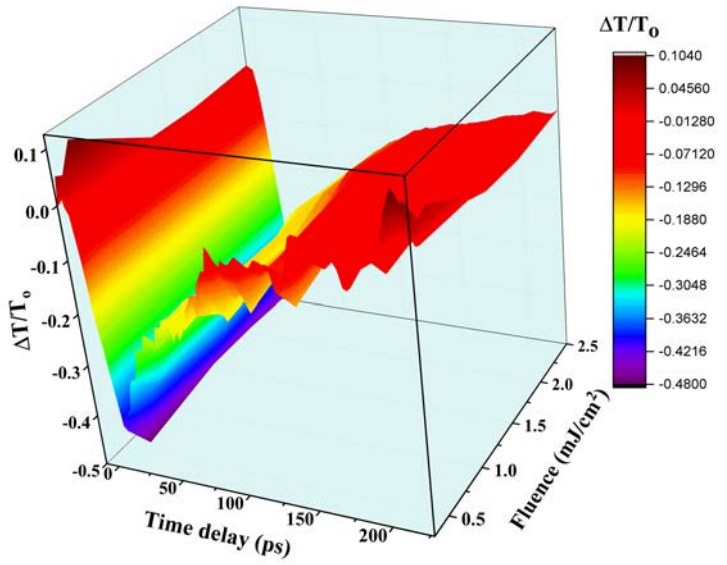

(a)

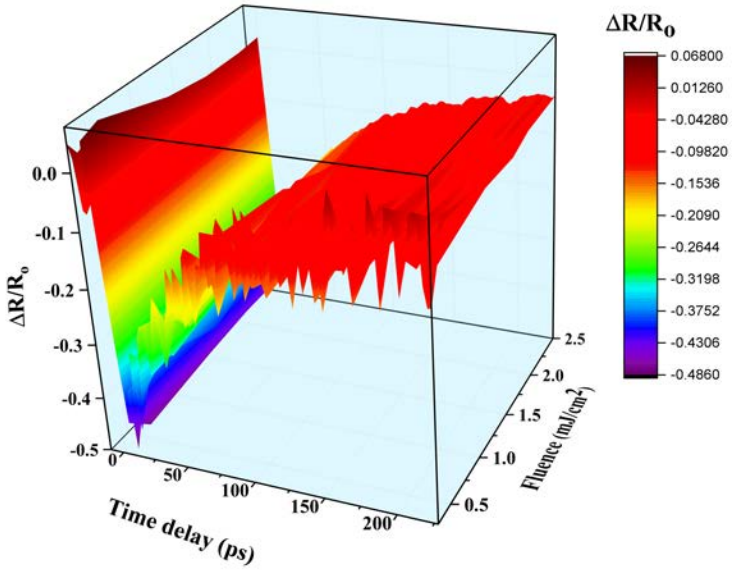

(b)

FIGURE 5.7: (a) the transmittance change and (b)the reflectance change as a function of time delay between the pump and probe signals measured at $4mJ/cm^2$ excitation power over the probe fluence range from $0.5 - 2.5mJ/cm^2$ and $4\mu m$ probe wavelength.

of the probe signal by the free electrons generated by the pump beam. The figure also shows that the generated carriers evolve in time and recombine within $100ps$.

It should be noted here that there is no significant impact of changing the probe fluence on the recombination dynamics of the $npSi$ membrane. To verify that, the

reflection, transmission and the absorbance is plotted against the probe fluence as it is shown in the Figure.5.8. It can be seen from the figure that the the reflection, transmission and as a result absorption have peaks at the same modulation contrast over the range of the probe fluences. This indicates that the change in the fluence intensity of the probe has no contribution to the carrier recombination process of the nanporous silicon.

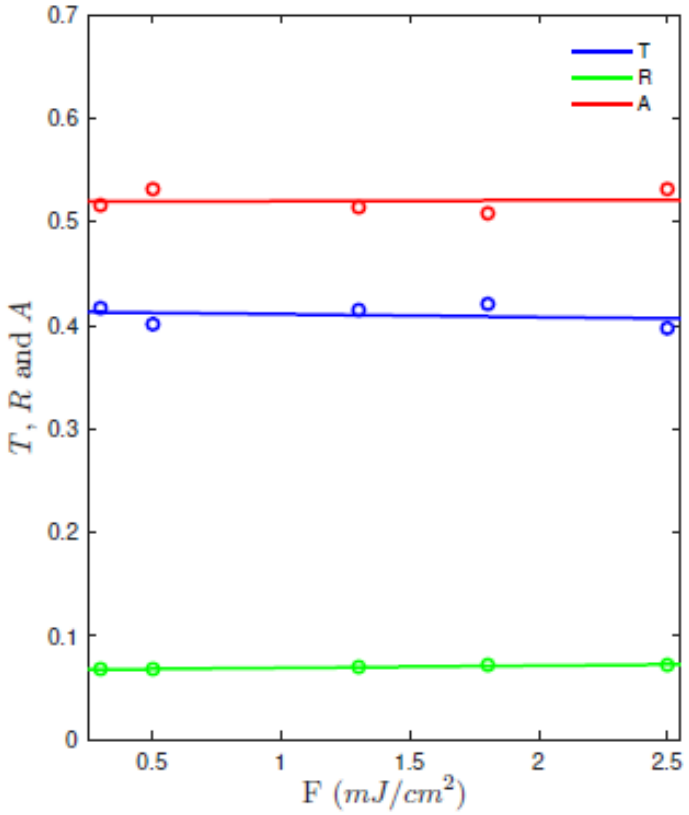

FIGURE 5.8: the reflection, transmission and the absorption of $111\mu m$ thick nanoporous silicon sample as a function of probe fluence at $4mJ/cm^2$ excitation fluence.

In order to evaluate the carrier recombination process of the sample mentioned above, the time resolved transmittance and reflectance changes were simultaneously measured as a function of pump fluence at $3.5\mu m$, $4\mu m$, $4.5\mu m$ and $5\mu m$ probe wavelengths respectively, as shown in the Figures 5.9 and 5.10. It can be

seen from the figures that both the transmittance and reflectance changes initially drop around zero delay between the pump and probe signals and reach the maximum change within sub-picoseconds time scale.

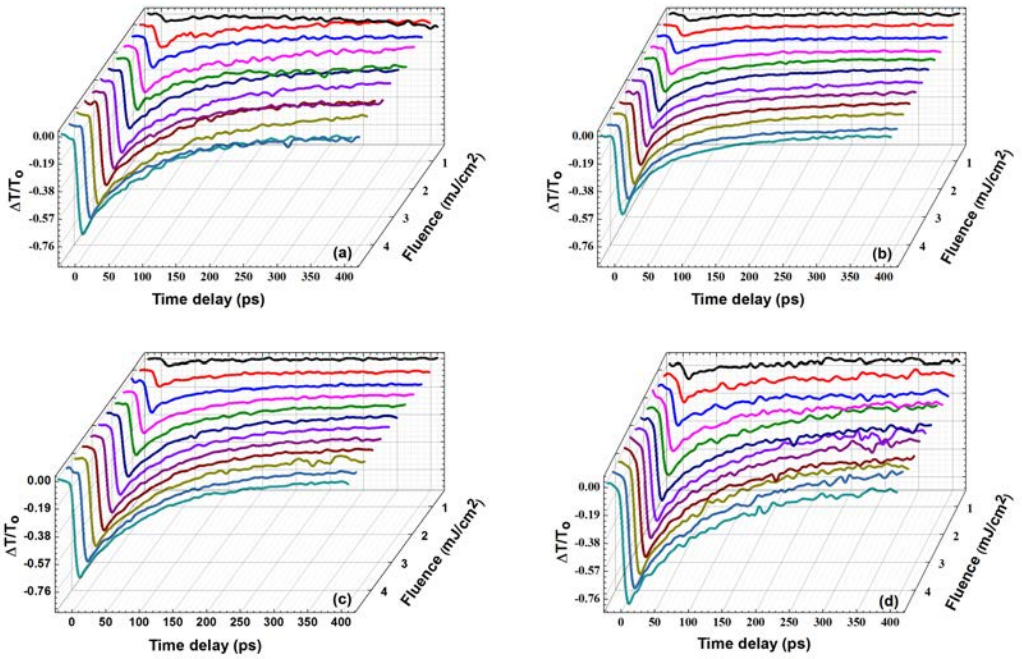

FIGURE 5.9: The time resolved transmittance change as a function of excitation fluence for $111\mu m$ thick nanporous silicon sample $npSi$ at (a) $3.5\mu m$ (b) $4\mu m$ (c)$4.5\mu m$ and (d)$5\mu m$ probe wavelengths.

The initial drop is attributed to the pump induced excitation of the free carriers. The carrier recovery process following the excitation, in the time scale of several hundreds of picoseconds, is due to the electron recombination process. It can be indicated that the carrier recombination rate of the $npSi$ is different at each probe wavelengths as well each excitation fluence. The transmittance and reflectance results shown in the Figures 5.9 and 5.10 are used to obtain the corresponding carrier concentration. The related approach used to obtain carrier concentration is based on the 2D Maxwell Garnett model and Wentzel-Kramers-Brillouin(WKB) approximation. More details about the simulation procedure and WKB approximation can be found in the chapter 3.

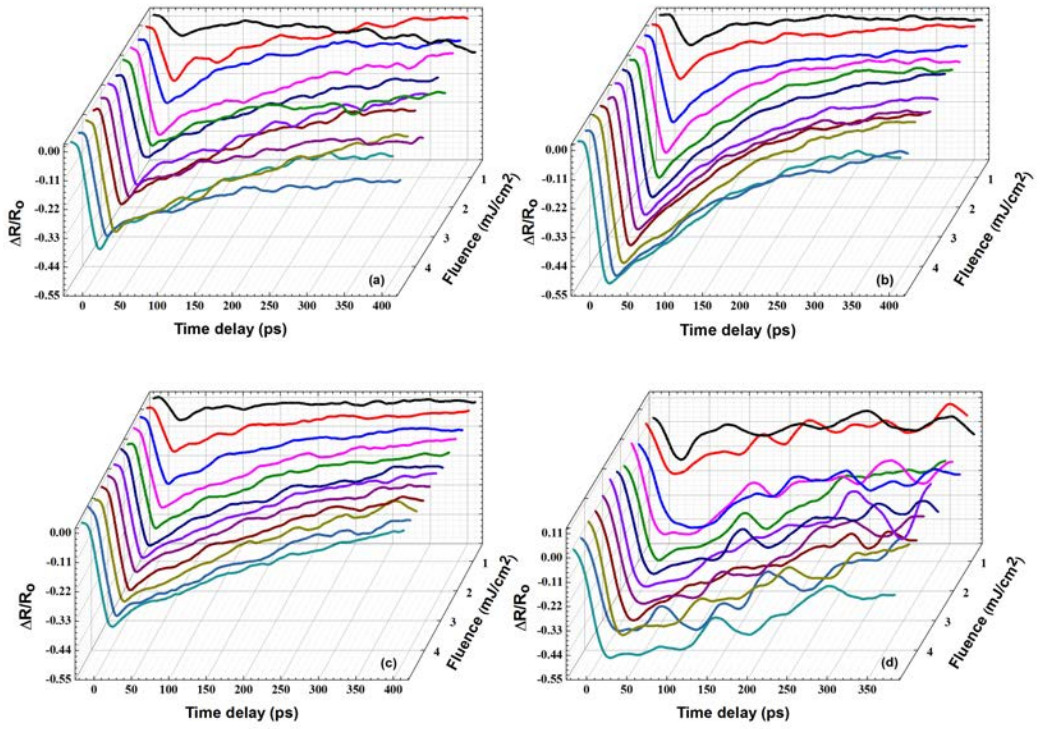

FIGURE 5.10: The time resolved reflectance change as a function excitation fluence for $111\mu m$ thick nanporous silicon sample $npSi$ at (a) $3.5\mu m$ (b) $4\mu m$ (c)$4.5\mu m$ and (d)$5\mu m$ probe wavelengths.

5.5 Recombination dynamics of the Nano-porous Silicon

In order to evaluate the carrier dynamics of the $111\mu m$-thick $npSi$, the recombination rate as well as the recombination time should be considered. The carrier concentrations can be extracted using 2D Maxwell Garnett model modified to include Drude like contribution, while the recombination time can be obtained based on the rate equation. As mentioned in Chapter 2, the decay time determined by the probe signal drops exponentially (by factor of $1/e$) depending on the penetration depth of the wavelength used.

The probe absorption coefficient can be also determined from the time resolved reflection and transmission. The absorption coefficient at the maximum excitation corresponds to $\alpha = ln(\frac{1-R_e}{T_e})/d$, where R_e and T_e represent the reflection and transmission of the probe signal respectively and d is the thickness of the sample.

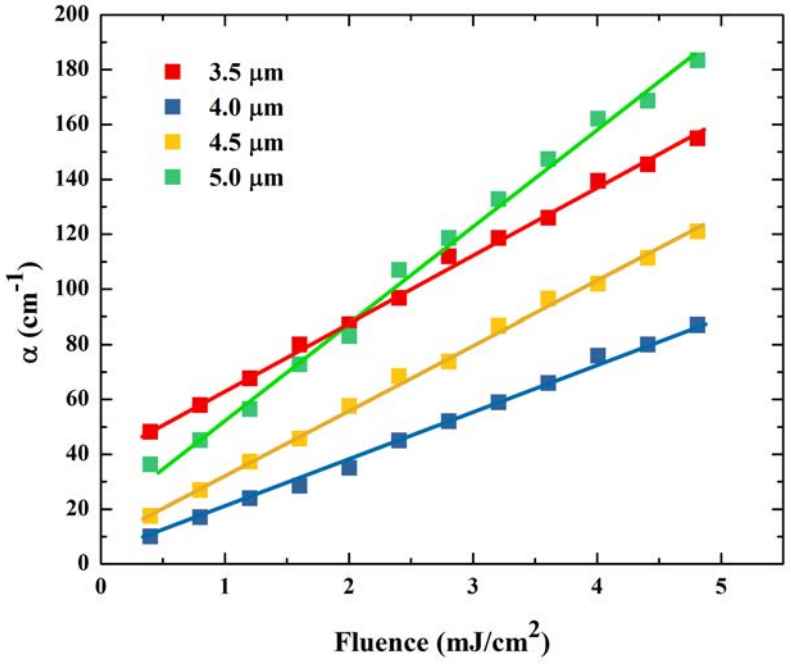

FIGURE 5.11: The absorption coefficient of the probe signal determined from the time resolved reflection and transmission at the maximum excitation. The absorption coefficient determined at $3.5\mu m$, $4\mu m$, $4.5\mu m$ and $5\mu m$ probe wavelengths respectively.

Figure.5.11 shows the absorption coefficient of the probe signal determined from the reflection and transmission signals at maximum reflectance and transmittance changes at different probe wavelengths. It can be seen from the figure that the sample becomes strongly absorptive with increasing the excitation fluence with distinctive probe absorption coefficient at each probe wavelengths. It can be also seen that the absorption coefficient at $4\mu m$ probe wavelength is lower compared to that shown for 5μm. The absorption coefficient of the rest of the probe wavelengths fall somewhere between the values mentioned above.

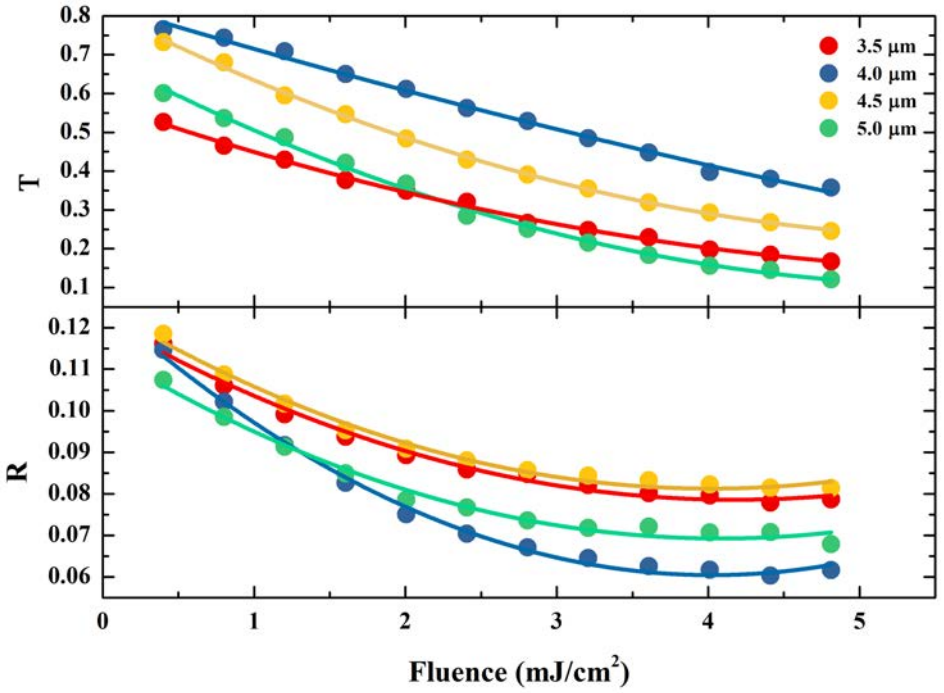

FIGURE 5.12: The reflection and transmission as a function of the pump fluence and different probe wavelengths. The data in this figure correspond to the maximum reflection and transmission of the time resolved measurements at maximum excitation

.

In order to reveal the dynamics of the carriers at different probe wavelengths, the Wentzel-Kramers-Brillouin(WKB) approximation is employed to simulate the reflection and transmission of the 111μm-thick $npSi$ at different probe wavelengths. The mathematical treatment of the above model is explained in details in the chapter 3. The reflection and transmission data were fitted at each time delay between the pump and probe signals at the maximum drops of the reflection and transmission respectively. The contribution of the excitation (generated carriers)is taken into account through modifying Maxwell Garnett effective medium theory (EMT)to include Drude like contribution to the effective dielectric constant.

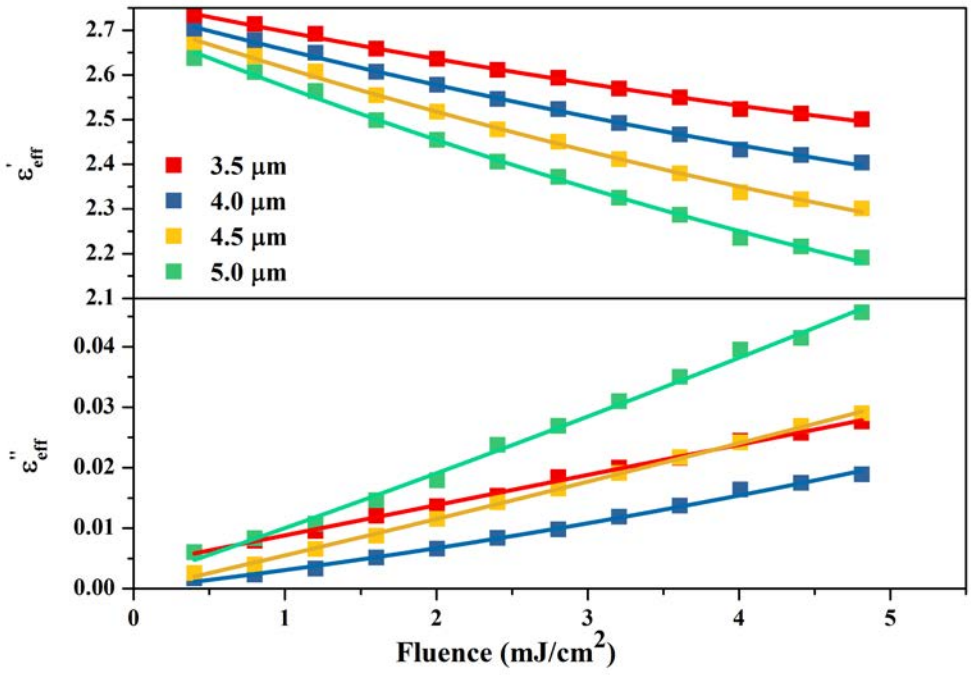

FIGURE 5.13: The real (upper panel) and the imaginary (lower panel) for the $111\mu m$-thick $npSi$ sample as a function of the excitation fluence and different probe wavelengths. The non-uniform WKB model is used together with Maxwell Garnett effective medioum approximation to simulate the reflection and transmission signals and extract the complex dielectric function of the sample

.

To extract the change in the optical properties of the $npSi$ sample such as the dielectric function and the Drude parameters, the reflection and transmission data at maximum pump fluence were analysed at 3.5, 4.0, 4.5 and $5.0\mu m$ respectively. Figure 5.12 shows the reflection and transmission for $npSi$ as a function of the excitation fluence at different probe wavelengths. The result shows that both reflection and transmission for all the probe wavelengths drop with increasing excitation fluence. It can be also seen that the transmission drop at probe wavelengths 3.5 and 5.0 are almost comparable while lower transmission change observed for the rest of the probe wavelengths. The reflection from the sample initially drops followed by the saturation at excitation fluences greater than $2.5mJ/cm^2$. The WKB model is used to simulate the reflection in which the nonuniform change of the dielectric function is taken in the consideration as a function of depth[**?**]. This non-uniform

change in our case is associated with the change of the carrier density along the sample depth. The model is used together with the Maxwell Garnett effective medium approximation modified to include Drude like contribution to extract the real and the imaginary parts of the dielectric function, as shown in the figure 5.13. The figure shows the real (upper panel) and the imaginary parts of the dielectric function of the $111\mu m$- thick $npSi$ as a function of pump fluence at different probing wavelengths. It can be seen from figure that the real part of the dielectric function is strongly dropped from nearly 2.7 to around 2.15 with increasing the excitation fluence which can be attributed to the change in the optical properties of the sample induced by the photo-excitation. In contrast, the imaginary part of the dielectric function is increasing with increasing the excitation fluence.

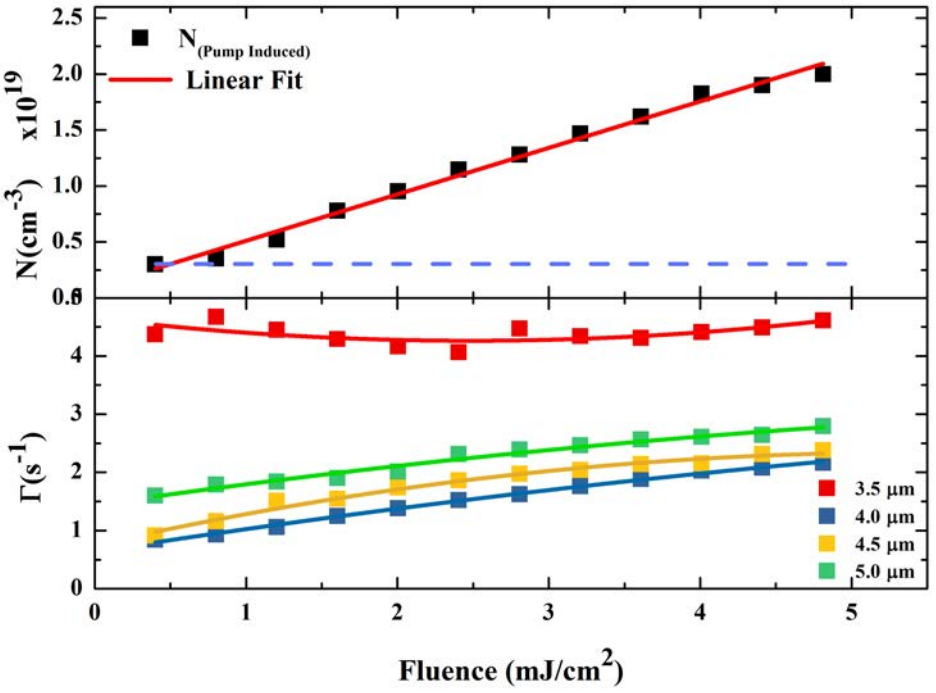

FIGURE 5.14: Carrier concentration $N(cm^{-1})$(upperpanel) as well as the scattering rate Γ as a function of excitation fluence and different probe wavelengths. The result shown in the figure were extracted based on the same model mentioned earlier.

.

The results indicated that the $npSi$ sample is highly absorptive at $5\mu m$ probe wavelength compared to $4\mu m$ probing wavelength at which the sample is highly

transparent(see FTIR measurement figure 4.1(a)). The results also showed that the imaginary part of the dielectric function for both 3.5 and 4.0μm wavelengths are nearly same over all excitation fluences.

Since the Drude contribution is also incorporated in the model, the carrier concentration N as well as the scattering rate Γ can be also extracted as shown in the figure 5.14. The figure shows that the pump induced carriers linearly increases with increasing the excitation fluence. The carrier concentration of the unexcited *npSi* only has the contribution from doping which is indicated by the blue line in the above figure. However, for the excited state N = Ndop + Npump which includes the contribution of both doping as well as the photo-excited electron density respectively.

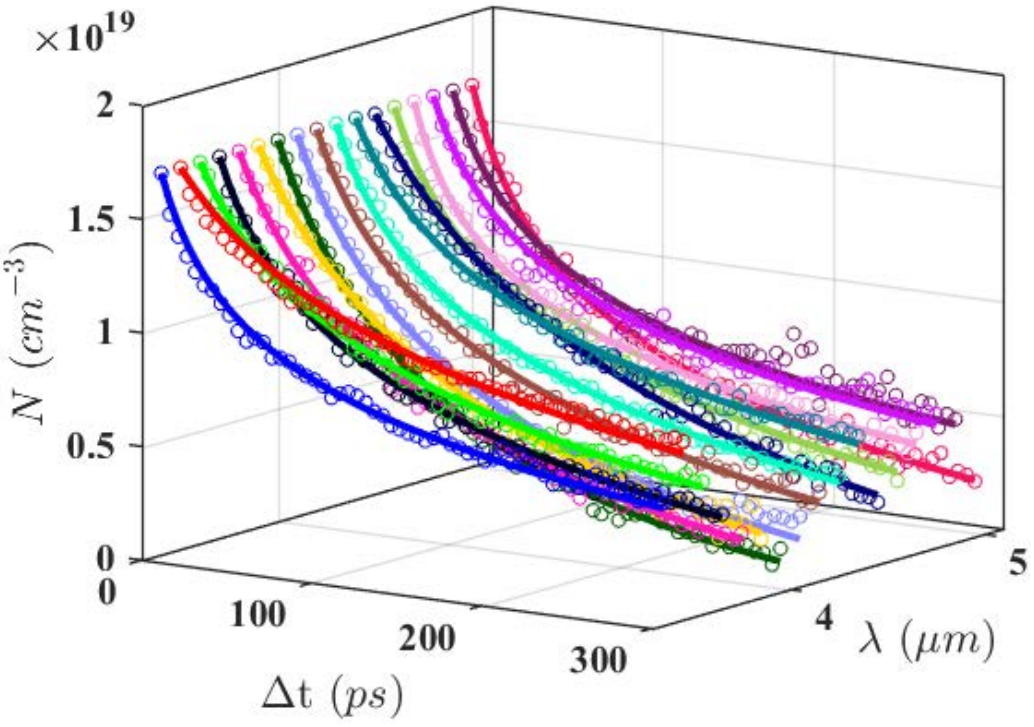

FIGURE 5.15: Carrier concentration for 111μm-thick *npSi* as a function of the time delay between the pump and probe signals at different probe wavelengths and 50mW pump power. The Wentzel-Kramers-Brillouin(WKB) approximation together with 2D Maxwell Garnett model is used to obtain the concentration while the rate equation is used to extract the recombination time at each wavelength.

The figure also shows that the scattering rate at probe wavelengths 4.0, 4.5 and $5.0\mu m$ also increase with increasing excitation flueence with relatively higher scattering rate observed at $5\mu m$ probe wavelength. However, the scattering rate at $3.5\mu m$ probe wavelengths is almost flat over all of excitation level. It should noted here that the scattering rate at $3.5\mu m$ probe wavelength is obviously higher compared to the rest of the wavelengths and fluctuating around $4.5 \times 10^{13}(s^{-1})$.

Figure.5.15 shows the time resolved carrier concentration at different probe wavelengths and $50mW$ pump power corresponding to excitation fluence of about $4.01mJ/cm^2$. It can be seen from the figure that there is distinctive recombination rate at each probe wavelength spanning from 3.4 to $5\mu m$.

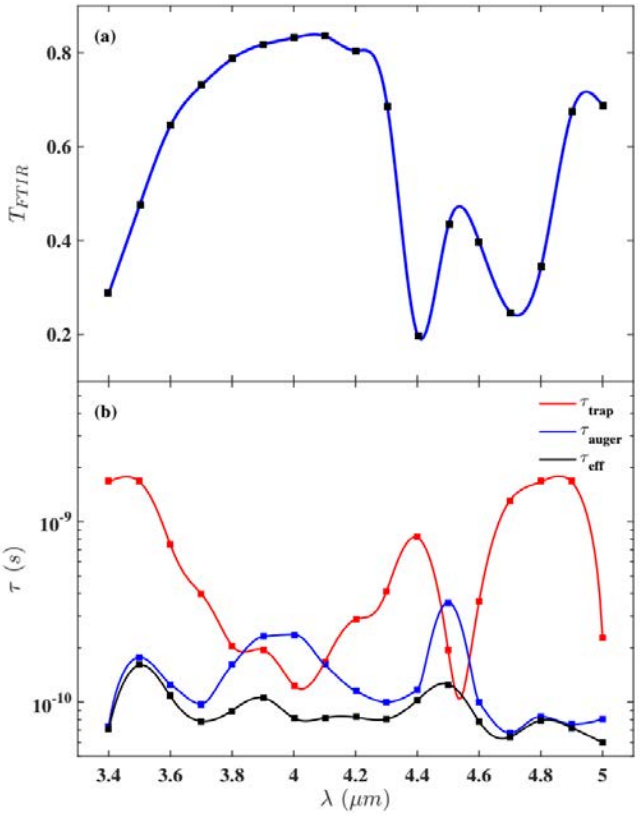

FIGURE 5.16: (a)the recombination time as a function of probe wavelengths at $50mW$ pump power corresponding to excitation fluence of about $4.01mJ/cm^2$(b)FTIR measurements for the $111\mu m$-thick $npSi$. The recombination times were extracted using the equation 5.1 to fit the time resolved data shown in the figure.5.13.

The recombination dynamics of the *npSi* is evaluated based on the decay rate equation as illustrated in the equation 5.1. Figure.5.14 shows the retrieved recombination time and FTIR measurements for 111μm-thick *npSi*. The recombination times were extracted through fitting the the rate equation to the carrier concentration as a function of time delay shown in the figure.5.15. Here, the carrier recombination considered to be due to three different processes including Shockley Read Hall(SRH)or trap assisted, carrier-carrier and Auger recombination.

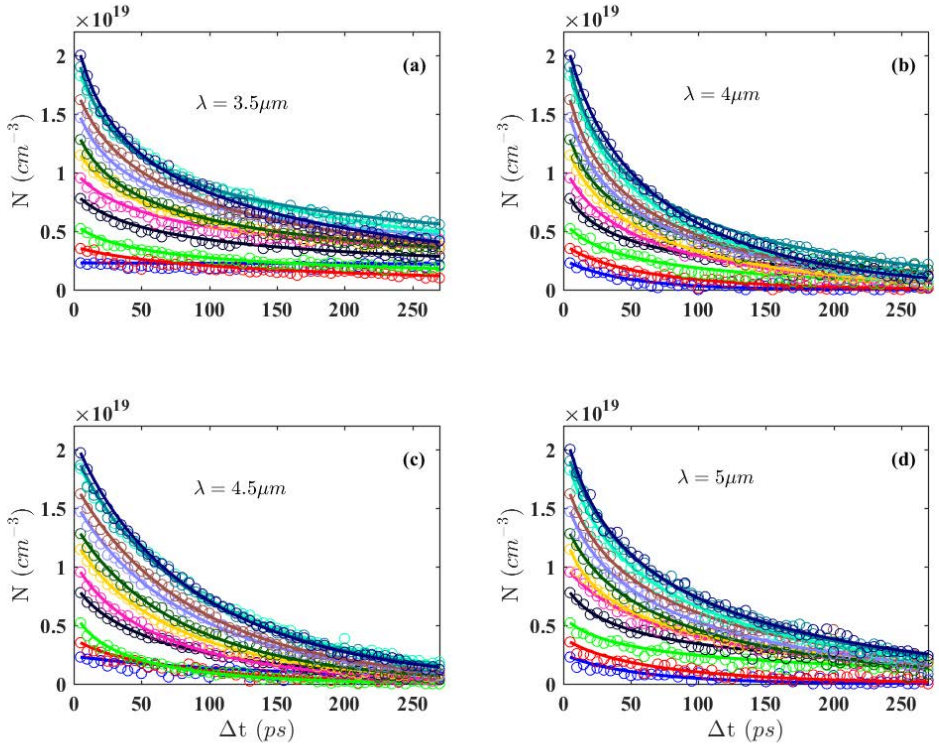

FIGURE 5.17: Carrier concentration as a function of time delay at different probe wavelengths and excitation fluences from 0.401 to 4.812mJ/cm^2. The WKB model is used together with Maxwell Garnett effective medium theory (EMT) modified to include Drude like contribution to fit the time resolved data shown in the figures 5.10 and 5.11

It can be seen from the figure 5.16(b) that the trap assisted recombination is not the only dominating recombination process over the probe wave length spanning from 3.4-5μm. Instead, at certain probe wavelengths, the contribution of the Auger recombination enhances and leads the recombination process. In order to examine the underpinning reason, the FTIR spectrum is present covering the same range

of probe wavelengths to examine the possible electronic-vibrational coupling, as shown in the figure 5.16(a). It can be clearly seen that the Auger recombination processes remarkably enhances around the highest absorption region in the FTIR spectrum. This enhancement can be attributed to surface absorbates vibrational modes assigned as $Si-O-H$ at $3.4\mu m$ and $Si-H$ at the wavelength range $4.4-4.7\mu m$. The relaxation time for a fundamental $O-H(\nu=1)$ stretching vibration mode is $216ps$ at room temperature [213] and those for SiH_1, SiH_2 and O_3Si-H are 24, 89 and $12ps$, respectively [214]. The relaxation time of the $O-H$ molecular vibration is longer than that of the $Si-H$ related modes. This means that a longer molecular vibration lifetime induces a slower decay of the photo-excited electrons. Therefore, the longer decay time at the probe wavelength of $3.5\mu m$ related to the $O-H$ mode arises from the longer lifetime of the $O-H$ molecular vibration compared with the $Si-H$ related modes.

In the previous paragraphs, the recombination processes following the pump excitation were evaluated at single excitation level. However, deep understanding of the process that follows the excitation of the $npSi$ sample requires recombination evaluation at different excitation levels as well as different probe wavelengths. To do that, the same optical model used to fit the reflection and transmission signals at different excitation levels from 0.4 to $4.8mJ/cm^2$ as well as different probe wavelengths. The extracted carrier concentration are presented in the figure 5.17. The figure shows that the carrier concentration increases around the zero delay as a result of pump excitation. The figure also indicates that the $npSi$ sample shows different recombination rate at different excitation fluences as well as different probing wavelengths. By fitting the data shown in the figure 5.17, the corresponding relaxation times, at different excitation fluences as well as different probing wavelengths, can be obtained as shown in the figure 5.18.

Figure 5.18 shows the recombination times as a function of carrier concentration extracted by fitting the recombination equation to the time resolved carrier concentration shown in the figure 5.15.

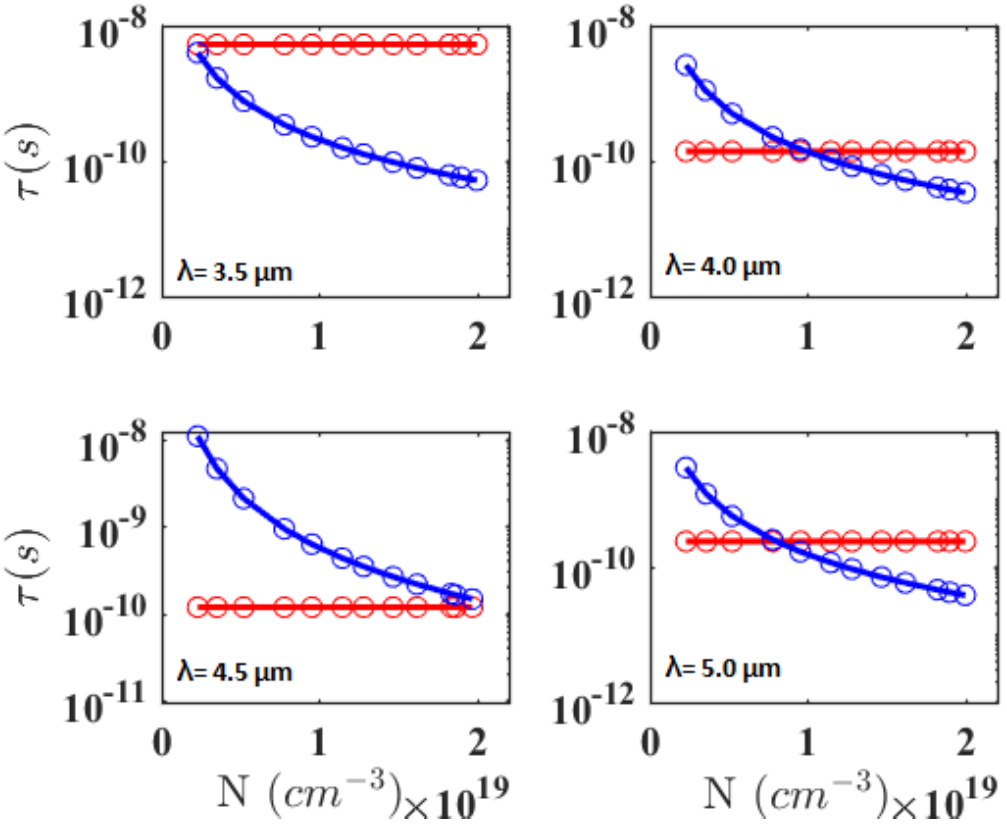

FIGURE 5.18: The recombination times for both (a) SHR or trap assisted recombination (Red circles) (b) Auger recombination (blue circles). The recombination times extracted from the fitting of the recombination equation to the data shown in the figure 5.15.

It can be seen from the figure that there are different recombination time for each involved process at different probe wavelength. It should be noted here that the carrier concentration are extracted from the figure 5.17 at the maximum excitation fluence. The figure shows that the Auger recombination time for all probe wavelengths are nearly comparable and compete and even become faster than SRH process at high excitation fluences. The result indicated that SRH or trap assisted recombination at $3.5\mu m$ is two order of magnitude longer compared to that shown with the rest of the wavelengths. The SRH recombination times at the probing wavelengths 4.0, 4.5 and $5\mu m$ are almost comparable. It can be concluded here that the longer SRH or trap assisted recombination time at $3.5\mu m$ probe wavelength could be due to the coupling between the vibrational mode and electronic states. As it is mentioned previously, the $O-H$ vibrational possess

longer relaxation time compared to the rest of the modes. Thus, the longer SRH or trap assisted recombination time could be attributed to the long life time of the $O-H$ vibrational mode.

5.6 Summary

In this chapter, the recombination dynamics of the microporous $mpSi$ and nanoporous $npSi$ following photo-excitation are evaluated. The results indicated that the the carrier recombination of the 16μm-thick sample follows Shockley Read Hall (SRH) recombination with recombination coefficient of about $1.65\times10^{9}s^{-1}$. The recombination dynamics of the $npSi$ was investigated based on the recombination time of each process involved in the recombination process. the result showed that there are different recombination times for different probing wavelength. The result also indicated that both SRH and Auger process have contributions to the carrier recombination process of the $npSi$ sample at different probe wavelengths. At low excitation fluence, the Auger recombination times almost two order of magnitude longer than that shown with SRH at $4\mu m$, $4.5\mu m$ and $5.0\mu m$. At high excitation flunces, the Auger process competes with and even become faster than the SRH type at some probing wavlengths except for $3.5\mu m$ where two order of magnitude longer times was observed. The longer recombination time observed with $3.5\mu m$ is attributed to the coupling between the electronic states and the vibrational modes.

Chapter 6

Conclusion

The optical components operating in MWIR range have attracted great attention recently due to their significant importance in many technological areas such as free space optical communication and multi-spectral thermal imaging. Furthermore, the motivation rises from the fact that such optical components capable to operate at different atmospheric conditions with relatively higher performances. Realising fast optical modulators accomplish new capabilities such as protection of rapidly activated sensors, hyper spectral imaging and time of flight applications. The optical based modulators also allow overcoming the inherent drawbacks of traditional electro-mechanical modulators. In the most of previously conducted studies, the optical modulation has been evaluated over limited or discrete spectral wavelengths while the rest of the MWIR spectral range still needs to be evaluated. Moreover, the optically modulated semiconductors provides faster switching speed associated with carrier recombination process with reduced noise as they avoid electro-optical signal conversion.

In conclusion, the performance of nanoporous $npSi$ and microporous $mpSi$ silicon as an active component for electro-optical light modulators are compared and evaluated in the mid-wave infrared MWIR range. Both membranes were evaluated using different measurements: The first approach includes FTIR measurements of the ground state transmission of unexcited sample as well as the modulation contrast induced by pump at different probe wavelengths. In the second approach

fluence dependence reflectance and transmittance were evaluated at different pump fluences while the third part involved reflectance and transmittance measurements as a function of time delay between the pump and probe signals. The measurements indicated that the porosity, pores as well as the the dimensions of the skeleton have crucial contribution to the spectral features of both membranes. The results also revealed that the transmitted light through the $mpSi$ is mainly influenced by the scattering from sub-micron size pores at shorter wavelengths, while distinctive absorption bands associated with impurities at the surface were observed with $npSi$ membrane. The time resolved pump-probe measurements showed that the response time of the $npSi$ is faster than that of $mpSi$ which allow its use as an optical modulator in the GHz range. The FTIR (ground state transmission)measurements demonstrated that both membranes have transparencies of about 90%, while 60% of the infrared light can be blocked if the membranes pumped optically with fluence less than $5mJ/cm^2$. The time resolved reflectance measurements revealed the phenomenon of plasma resonance at which the optical properties of the $mpSi$ sample become similar to that shown by metals. At the resonance, the dielectric function become negative and the $mpSi$ sample becomes more reflective. This feature can be exploited in the design and development of semiconductor based optical modulators. As a possible direction of enhancing the filtering and the modulation depth of the membranes, one might suggest affecting the band structure by artificial stress or using multi layered porous silicon structure [215].

The recombination of the excited carriers of the nanoporous and microporous silicon are also evaluated and compared. The carrier recombination of the $mpSi$ is analysed based on the initial carrier concentration method. The result revealed that the carrier recombination of the excited $mpSi$ membrane follows Shockley−Read−Hall (SRH) process with recombination coefficient of about $1.65\times 10^9 s^{-1}$. On the other hand, the optical model based on the Maxwell−Garnett approximation and WKB transfer matrix method are used to simulate the reflection and transmission of the $npSi$ membrane. From the simulation, the optical properties as well as the Drude parameters are extracted. According the rate equation,

the recombination times are calculated at different probe wavelengths. The recombination times demonstrated that the SRH recombination process dominates at low excitation fluences except for $3.5\mu m$ where the recombination time is two order of magnitude slower. At high excitation fluences, the Auger recombination process competes with SRH type and even faster at some probe wavelengths. The longer SRH recombination time observed at probe wavelength of $3.5\mu m$ is attributed to the vibrational-electronic state coupling.

Bibliography

[1] P. Lautenschlager, M. Garriga, L. Vina, and M. Cardona, "Temperature dependence of the dielectric function and interband critical points in silicon," *Physical Review B*, vol. 36, no. 9, p. 4821, 1987.

[2] G. Jellison, "Optical functions of silicon determined by two-channel polarization modulation ellipsometry," *Optical Materials*, vol. 1, no. 1, pp. 41–47, 1992.

[3] V. Yakovlev and E. Irene, "An interface enhanced spectroscopic ellipsometry technique: Application to si-sio2," *Journal of The Electrochemical Society*, vol. 139, no. 5, pp. 1450–1455, 1992.

[4] N. V. Nguyen, D. Chandler-Horowitz, P. M. Amirtharaj, and J. G. Pellegrino, "Spectroscopic ellipsometry determination of the properties of the thin underlying strained si layer and the roughness at sio2/si interface," *Applied physics letters*, vol. 64, no. 20, pp. 2688–2690, 1994.

[5] Z. Chang, *Fundamentals of attosecond optics*. CRC Press, 2016.

[6] A. Esser, H. Heesel, H. Kurz, C. Wang, G. Parsons, and G. Lucovsky, "Femtosecond spectroscopic study of ultrafast carrier relaxation in hydrogenated amorphous silicon a-si: H," *Journal of applied physics*, vol. 73, no. 3, pp. 1235–1239, 1993.

[7] E. Lioudakis, A. Othonos, and A. Nassiopoulou, "Ultrafast transient photoinduced absorption in silicon nanocrystals: Coupling of oxygen-related states to quantized sublevels," *Applied physics letters*, vol. 90, no. 17, p. 171103, 2007.

[8] J. Von Behren, Y. Kostoulas, K. B. Üçer, and P. Fauchet, "The femtosecond optical response of porous, amorphous and crystalline silicon," *Journal of non-crystalline solids*, vol. 198, pp. 957–960, 1996.

[9] P. Fauchet, D. Hulin, R. Vanderhaghen, A. Mourchid, and W. Nighan, "The properties of free carriers in amorphous silicon," *Journal of non-crystalline solids*, vol. 141, pp. 76–87, 1992.

[10] V. Grivickas and J. Linnros, "Free-carrier absorption and luminescence decay of porous silicon," *Thin solid films*, vol. 255, no. 1, pp. 70–73, 1995.

[11] R. Ulbricht, E. Hendry, J. Shan, T. F. Heinz, and M. Bonn, "Carrier dynamics in semiconductors studied with time-resolved terahertz spectroscopy," *Reviews of Modern Physics*, vol. 83, no. 2, p. 543, 2011.

[12] L. Fekete, P. Kužel, H. Němec, F. Kadlec, A. Dejneka, J. Stuchlík, and A. Fejfar, "Ultrafast carrier dynamics in microcrystalline silicon probed by time-resolved terahertz spectroscopy," *Physical Review B*, vol. 79, no. 11, p. 115306, 2009.

[13] M. C. Beard, G. M. Turner, and C. A. Schmuttenmaer, "Subpicosecond carrier dynamics in low-temperature grown gaas as measured by time-resolved terahertz spectroscopy," *Journal of Applied Physics*, vol. 90, no. 12, pp. 5915–5923, 2001.

[14] M. C. Beard, G. M. Turner, and C. A. Schmuttenmaer, "Transient photoconductivity in gaas as measured by time-resolved terahertz spectroscopy," *Physical Review B*, vol. 62, no. 23, p. 15764, 2000.

[15] D. Cooke, A. MacDonald, A. Hryciw, J. Wang, Q. Li, A. Meldrum, and F. Hegmann, "Transient terahertz conductivity in photoexcited silicon nanocrystal films," *Physical Review B*, vol. 73, no. 19, p. 193311, 2006.

[16] M. Samoc, A. Samoc, B. Luther-Davies, Z. Bao, L. Yu, B. Hsieh, and U. Scherf, "Femtosecond z-scan and degenerate four-wave mixing measurements of real and imaginary parts of the third-order nonlinearity of soluble conjugated polymers," *JOSA B*, vol. 15, no. 2, pp. 817–825, 1998.

[17] J. Wang, M. Sheik-Bahae, A. Said, D. J. Hagan, and E. W. Van Stryland, "Time-resolved z-scan measurements of optical nonlinearities," *JOSA B*, vol. 11, no. 6, pp. 1009–1017, 1994.

[18] P. Zhang, X. Zhang, P. Lu, J. Xu, X. Xu, W. Li, and K. Chen, "Interface state-related linear and nonlinear optical properties of nanocrystalline si/sio 2 multilayers," *Applied Surface Science*, vol. 292, pp. 262–266, 2014.

[19] R. R. Gattass, L. B. Shaw, and J. S. Sanghera, "Broadband watt-level mid-infrared fiber-coupled variable optical attenuator," *IEEE Photonics Technology Letters*, vol. 25, no. 20, pp. 2007–2009, 2013.

[20] C. Lee and J. A. Yeh, "Development and evolution of moems technology in variable optical attenuators," *Journal of Micro/Nanolithography, MEMS, and MOEMS*, vol. 7, no. 2, pp. 021003–021003, 2008.

[21] L. Fekete, J. Hlinka, F. Kadlec, P. Kužel, and P. Mounaix, "Active optical control of the terahertz reflectivity of high-resistivity semiconductors," *Optics letters*, vol. 30, no. 15, pp. 1992–1994, 2005.

[22] M. Först, J. Niehusmann, T. Plötzing, J. Bolten, T. Wahlbrink, C. Moormann, and H. Kurz, "High-speed all-optical switching in ion-implanted silicon-on-insulator microring resonators," *Optics letters*, vol. 32, no. 14, pp. 2046–2048, 2007.

[23] L. O'Faolain, D. M. Beggs, T. P. White, T. Kampfrath, K. Kuipers, and T. F. Krauss, "Compact optical switches and modulators based on dispersion engineered photonic crystals," *IEEE Photonics Journal*, vol. 2, no. 3, pp. 404–414, 2010.

[24] D. Liang and J. E. Bowers, "Recent progress in lasers on silicon," *Nature Photonics*, vol. 4, no. 8, pp. 511–517, 2010.

[25] G. T. Reed, G. Mashanovich, F. Gardes, and D. Thomson, "Silicon optical modulators," *Nature photonics*, vol. 4, no. 8, pp. 518–526, 2010.

[26] I. Littler, L. Fu, E. Mägi, D. Pudo, and B. Eggleton, "Widely tunable, acousto-optic resonances in chalcogenide as2se3 fiber," *Optics express*, vol. 14, no. 18, pp. 8088–8095, 2006.

[27] B. J. Eggleton, B. Luther-Davies, and K. Richardson, "Chalcogenide photonics," *Nature photonics*, vol. 5, no. 3, pp. 141–148, 2011.

[28] M. Nedeljkovic, A. Khokhar, Y. Hu, X. Chen, J. S. Penades, S. Stankovic, H. Chong, D. Thomson, F. Gardes, G. Reed, *et al.*, "Silicon photonic devices and platforms for the mid-infrared," *Optical Materials Express*, vol. 3, no. 9, pp. 1205–1214, 2013.

[29] T. Hu, B. Dong, X. Luo, T.-Y. Liow, J. Song, C. Lee, and G.-Q. Lo, "Silicon photonic platforms for mid-infrared applications," *Photonics Research*, vol. 5, no. 5, pp. 417–430, 2017.

[30] R. Shankar and M. Lončar, "Silicon photonic devices for mid-infrared applications," *Nanophotonics*, vol. 3, no. 4-5, pp. 329–341, 2014.

[31] R. A. Soref, "Silicon-based optoelectronics," *Proceedings of the IEEE*, vol. 81, no. 12, pp. 1687–1706, 1993.

[32] L. Kimerling, L. Dal Negro, S. Saini, Y. Yi, D. Ahn, S. Akiyama, D. Cannon, J. Liu, J. Sandland, D. Sparacin, *et al.*, "Monolithic silicon microphotonics," in *Silicon Photonics*, pp. 89–120, Springer, 2004.

[33] M. Salib, L. Liao, R. Jones, M. Morse, A. Liu, D. Samara-Rubio, D. Alduino, and M. Paniccia, "Silicon photonics.," *Intel Technology Journal*, vol. 8, no. 2, 2004.

[34] V. R. Almeida, C. A. Barrios, R. R. Panepucci, and M. Lipson, "All-optical control of light on a silicon chip," *Nature*, vol. 431, no. 7012, pp. 1081–1084, 2004.

[35] K. K. Lee, *Transmission and routing of optical signals in on-chip waveguides for silicon microphotonics*. PhD thesis, Massachusetts Institute of Technology, 2001.

[36] P. Dainesi, L. Thevanaz, and P. Robert, "5 mhz 2× 2 optical switch in silicon on insulator technology using plasma dispersion effect," in *Optical Communication, 2001. ECOC'01. 27th European Conference on*, vol. 2, pp. 132–133, IEEE, 2001.

[37] R. Soref and B. Bennett, "Electrooptical effects in silicon," *IEEE journal of quantum electronics*, vol. 23, no. 1, pp. 123–129, 1987.

[38] M. W. Geis, S. J. Spector, R. Williamson, and T. Lyszczarz, "Submicrosecond submilliwatt silicon-on-insulator thermooptic switch," *IEEE photonics technology letters*, vol. 16, no. 11, pp. 2514–2516, 2004.

[39] J. Faist, F. Capasso, D. L. Sivco, C. Sirtori, A. L. Hutchinson, A. Y. Cho, *et al.*, "Quantum cascade laser," *Science*, vol. 264, no. 5158, pp. 553–556, 1994.

[40] E. R. Weber, R. Willardson, H. Liu, and F. Capasso, *Intersubband transitions in quantum wells: physics and device applications*, vol. 62. Academic press, 1999.

[41] R. D. Kekatpure and M. L. Brongersma, "Near-infrared free-carrier absorption in silicon nanocrystals," *Optics letters*, vol. 34, no. 21, pp. 3397–3399, 2009.

[42] A. Liu, R. Jones, L. Liao, D. Samara-Rubio, D. Rubin, O. Cohen, R. Nicolaescu, and M. Paniccia, "A high-speed silicon optical modulator based on a metal–oxide–semiconductor capacitor," *Nature*, vol. 427, no. 6975, pp. 615–618, 2004.

[43] J. Barreto, T. Roger, and A. Kaplan, "Resolving the ultrafast dynamics of charge carriers in nanocomposites," *Applied Physics Letters*, vol. 100, no. 24, p. 241906, 2012.

[44] S. J. Park, A. Zakar, V. L. Zerova, D. Chekulaev, L. T. Canham, and A. Kaplan, "All-optical modulation in mid-wavelength infrared using porous si membranes," *Scientific Reports*, vol. 6, 2016.

[45] M. Nedeljkovic, R. Soref, and G. Z. Mashanovich, "Free-carrier electrorefraction and electroabsorption modulation predictions for silicon over the 1–14-infrared wavelength range," *IEEE Photonics Journal*, vol. 3, no. 6, pp. 1171–1180, 2011.

[46] R. K. Willardson, E. R. Weber, and K.-T. Tsen, *Ultrafast Physical Processes in Semiconductors*, vol. 67. Elsevier, 2000.

[47] S. Furukawa and T. Miyasato, "Quantum size effects on the optical band gap of microcrystalline si: H," *Physical Review B*, vol. 38, no. 8, p. 5726, 1988.

[48] V. Cesari, W. W. Langbein, P. Borri, M. Rossetti, A. Fiore, S. Mikhrin, I. Krestnikov, and A. Kovsh, "Ultrafast gain dynamics in 1.3 um inas/gaas quantum-dot optical amplifiers: The effect of p doping," *Applied physics letters*, vol. 90, no. 20, 2007.

[49] H. Benisty, C. Sotomayor-Torres, and C. Weisbuch, "Intrinsic mechanism for the poor luminescence properties of quantum-box systems," *Physical Review B*, vol. 44, no. 19, p. 10945, 1991.

[50] D. Paul and L. Robeson, "Polymer nanotechnology: nanocomposites," *Polymer*, vol. 49, no. 15, pp. 3187–3204, 2008.

[51] A. C. Turner-Foster, M. A. Foster, J. S. Levy, C. B. Poitras, R. Salem, A. L. Gaeta, and M. Lipson, "Ultrashort free-carrier lifetime in low-loss silicon nanowaveguides," *Optics express*, vol. 18, no. 4, pp. 3582–3591, 2010.

[52] C. Kittel and C.-y. Fong, *Quantum theory of solids*, vol. 33. Wiley New York, 1963.

[53] A. Othonos, "Probing ultrafast carrier and phonon dynamics in semiconductors," *Journal of applied physics*, vol. 83, no. 4, pp. 1789–1830, 1998.

[54] T. Ichibayashi and K. Tanimura, "Ultrafast carrier relaxation in si studied by time-resolved two-photon photoemission spectroscopy: intravalley scattering and energy relaxation of hot electrons," *Physical review letters*, vol. 102, no. 8, p. 087403, 2009.

[55] H. Choo, X. Hu, M. Downer, and V. Kesan, "Femtosecond ellipsometric study of nonequilibrium carrier dynamics in ge and epitaxial si1- xgex," *Applied physics letters*, vol. 63, no. 11, pp. 1507–1509, 1993.

[56] B. E. Sernelius, "Generalized drude approach to the conductivity relaxation time due to electron-hole collisions in optically excited semiconductors," *Physical Review B*, vol. 40, no. 18, p. 12438, 1989.

[57] E. Hendry, M. Koeberg, J. Pijpers, and M. Bonn, "Reduction of carrier mobility in semiconductors caused by charge-charge interactions," *Physical Review B*, vol. 75, no. 23, p. 233202, 2007.

[58] T.-I. Jeon and D. Grischkowsky, "Nature of conduction in doped silicon," *Physical Review Letters*, vol. 78, no. 6, p. 1106, 1997.

[59] N. Daldosso and L. Pavesi, "Nanosilicon photonics," *Laser & Photonics Reviews*, vol. 3, no. 6, pp. 508–534, 2009.

[60] L. V. Titova, T. L. Cocker, D. G. Cooke, X. Wang, A. Meldrum, and F. A. Hegmann, "Ultrafast percolative transport dynamics in silicon nanocrystal films," *Physical Review B*, vol. 83, no. 8, p. 085403, 2011.

[61] L. Bagolini, A. Mattoni, G. Fugallo, L. Colombo, E. Poliani, S. Sanguinetti, and E. Grilli, "Quantum confinement by an order-disorder boundary in nanocrystalline silicon," *Physical review letters*, vol. 104, no. 17, p. 176803, 2010.

[62] A. Yoffe, "Semiconductor quantum dots and related systems: electronic, optical, luminescence and related properties of low dimensional systems," *Advances in Physics*, vol. 50, no. 1, pp. 1–208, 2001.

[63] C. Shank, R. Yen, and C. Hirlimann, "Time-resolved reflectivity measurements of femtosecond-optical-pulse-induced phase transitions in silicon," *Physical Review Letters*, vol. 50, no. 6, p. 454, 1983.

[64] M. Lannoo, C. Delerue, and G. Allan, "Theory of radiative and nonradiative transitions for semiconductor nanocrystals," *Journal of Luminescence*, vol. 70, no. 1, pp. 170–184, 1996.

[65] M. Kubinyi, A. Grofcsik, W. Jones, T. Dyer, J. Marshall, and A. Hepburn, "Picosecond decay of photoinduced absorption in undoped amorphous and polycrystalline silicon thin films," *Thin solid films*, vol. 263, no. 1, pp. 99–104, 1995.

[66] L. Hu and G. Chen, "Analysis of optical absorption in silicon nanowire arrays for photovoltaic applications," *Nano letters*, vol. 7, no. 11, pp. 3249–3252, 2007.

[67] R. P. Prasankumar, P. C. Upadhya, and A. J. Taylor, "Ultrafast carrier dynamics in semiconductor nanowires," *physica status solidi (b)*, vol. 246, no. 9, pp. 1973–1995, 2009.

[68] V. I. Klimov, D. McBranch, C. Leatherdale, and M. Bawendi, "Electron and hole relaxation pathways in semiconductor quantum dots," *Physical Review B*, vol. 60, no. 19, p. 13740, 1999.

[69] S. Lyon, "Spectroscopy of hot carriers in semiconductors," *Journal of luminescence*, vol. 35, no. 3, pp. 121–154, 1986.

[70] S. Sundaram and E. Mazur, "Inducing and probing non-thermal transitions in semiconductors using femtosecond laser pulses," *Nature materials*, vol. 1, no. 4, pp. 217–224, 2002.

[71] M. Alonso, I. Marcus, M. Garriga, A. Goni, J. Jedrzejewski, and I. Balberg, "Evidence of quantum confinement effects on interband optical transitions in si nanocrystals," *Physical Review B*, vol. 82, no. 4, p. 045302, 2010.

[72] P.-C. Ou, W.-R. Liu, H.-J. Ton, J.-H. Lin, W.-F. Hsieh, *et al.*, "Ultrafast relaxation and absorption saturation at near exciton resonance in a thin zno epilayer," *Journal of Applied Physics*, vol. 109, no. 1, 2011.

[73] X. Chen, W. Shen, H. Chen, R. Zhang, and Y. He, "High electron mobility in well ordered and lattice-strained hydrogenated nanocrystalline silicon," *Nanotechnology*, vol. 17, no. 2, p. 595, 2006.

[74] C. Burda, X. Chen, R. Narayanan, and M. A. El-Sayed, "Chemistry and properties of nanocrystals of different shapes," *Chemical reviews*, vol. 105, no. 4, pp. 1025–1102, 2005.

[75] V. I. Klimov, "Optical nonlinearities and ultrafast carrier dynamics in semiconductor nanocrystals," *The Journal of Physical Chemistry B*, vol. 104, no. 26, pp. 6112–6123, 2000.

[76] K. Sokolowski-Tinten and D. von der Linde, "Generation of dense electron-hole plasmas in silicon," *Physical Review B*, vol. 61, no. 4, p. 2643, 2000.

[77] D. Aspnes and A. Studna, "Dielectric functions and optical parameters of si, ge, gap, gaas, gasb, inp, inas, and insb from 1.5 to 6.0 ev," *Physical Review B*, vol. 27, no. 2, p. 985, 1983.

[78] R. Biswas and V. Ambegaokar, "Phonon spectrum of a model of electronically excited silicon," *Physical Review B*, vol. 26, no. 4, p. 1980, 1982.

[79] R. Abram, G. Childs, and P. Saunderson, "Band gap narrowing due to many-body effects in silicon and gallium arsenide," *Journal of Physics C: Solid State Physics*, vol. 17, no. 34, p. 6105, 1984.

[80] A. Sabbah and D. M. Riffe, "Femtosecond pump-probe reflectivity study of silicon carrier dynamics," *Physical Review B*, vol. 66, no. 16, p. 165217, 2002.

[81] D. B. Mawhinney, J. A. Glass, and J. T. Yates, "Ftir study of the oxidation of porous silicon," *The Journal of Physical Chemistry B*, vol. 101, no. 7, pp. 1202–1206, 1997.

[82] L. T. Canham, "Properties of porous silicon," Institution of Electrical Engineers, 1997.

[83] J. Z. Wallner, "Porous silicon technology for integrated microsystems," dissertation, Michigan Technological University, 2006.

[84] L. Canham, *Handbook of porous silicon*. Springer, 2014.

[85] S. Lust and C. Lévy-Clément, "Chemical limitations of macropore formation on medium-doped p-type silicon," *Journal of The Electrochemical Society*, vol. 149, no. 6, pp. C338–C344, 2002.

[86] T. Trifonov, *Photonic bandgap analysis and fabrication of macroporous silicon by electrochemical etching*. PhD thesis, Universitat Rovira i Virgili. Departament d'Enginyeria Electrònica, Elèctrica i Automàtica, 2004.

[87] F. Müller, A. Birner, U. Gösele, V. Lehmann, S. Ottow, and n. Föll, "Structuring of macroporous silicon for applications as photonic crystals," *Journal of Porous Materials*, vol. 7, no. 1-3, pp. 201–204, 2000.

[88] C. Levy-Clement, A. Lagoubi, R. Tenne, and M. Neumann-Spallart, "Photoelectrochemical etching of silicon," *Electrochimica acta*, vol. 37, no. 5, pp. 877–888, 1992.

[89] L. T. Canham, "Silicon quantum wire array fabrication by electrochemical and chemical dissolution of wafers," *Applied Physics Letters*, vol. 57, no. 10, pp. 1046–1048, 1990.

[90] P. Calcott, K. Nash, L. Canham, M. Kane, and D. Brumhead, "Identification of radiative transitions in highly porous silicon," *Journal of Physics: Condensed Matter*, vol. 5, no. 7, p. L91, 1993.

[91] L. Tsybeskov, J. V. Vandyshev, and P. Fauchet, "Blue emission in porous silicon: Oxygen-related photoluminescence," *Physical Review B*, vol. 49, no. 11, p. 7821, 1994.

[92] M. Rosenbauer, S. Finkbeiner, E. Bustarret, J. Weber, and M. Stutzmann, "Resonantly excited photoluminescence spectra of porous silicon," *Physical Review B*, vol. 51, no. 16, p. 10539, 1995.

[93] A. Halimaoui, C. Oules, G. Bomchil, A. Bsiesy, F. Gaspard, R. Herino, M. Ligeon, and F. Muller, "Electroluminescence in the visible range during anodic oxidation of porous silicon films," *Applied Physics Letters*, vol. 59, no. 3, pp. 304–306, 1991.

[94] K. Hirschman, L. Tsybeskov, S. Duttagupta, P. Fauchet, *et al.*, "Silicon-based visible light-emitting devices integrated into microelectronic circuits," *Nature*, vol. 384, no. 6607, pp. 338–341, 1996.

[95] M. Fried, T. Lohner, O. Polgár, P. Petrik, E. Vazsonyi, I. Bársony, J. Piel, and J. Stehle, "Characterization of different porous silicon structures by spectroscopic ellipsometry," *Thin Solid Films*, vol. 276, no. 1, pp. 223–227, 1996.

[96] V. Klimov, D. McBranch, and V. Karavanskii, "Strong optical nonlinearities in porous silicon: Femtosecond nonlinear transmission study," *Physical Review B*, vol. 52, no. 24, p. R16989, 1995.

[97] T. Matsumoto, T. Futagi, H. Mimura, and Y. Kanemitsu, "Ultrafast decay dynamics of luminescence in porous silicon," *Physical Review B*, vol. 47, no. 20, p. 13876, 1993.

[98] M. Vaněček, A. Poruba, Z. Remeš, N. Beck, and M. Nesládek, "Optical properties of microcrystalline materials," *Journal of non-crystalline solids*, vol. 227, pp. 967–972, 1998.

[99] F. Wooten, *Optical properties of solids*. Academic press, 2013.

[100] O. Bisi, S. Ossicini, and L. Pavesi, "Porous silicon: a quantum sponge structure for silicon based optoelectronics," *Surface Science Reports*, vol. 38, no. 1, pp. 1 – 126, 2000.

[101] W. He, I. V. Yurkevich, L. T. Canham, A. Loni, and A. Kaplan, "Determination of excitation profile and dielectric function spatial nonuniformity in porous silicon by using wkb approach," *Optics express*, vol. 22, no. 22, pp. 27123–27135, 2014.

[102] W. He, *Ultrafast dynamics of photoexcited carriers in semiconducting nano materials*. PhD thesis, University of Birmingham, 2015.

[103] T. W. Roger, W. He, I. V. Yurkevich, and A. Kaplan, "Enhanced carrier-carrier interaction in optically pumped hydrogenated nanocrystalline silicon," *Applied Physics Letters*, vol. 101, no. 14, p. 141904, 2012.

[104] T. Suzuki and R. Shimano, "Cooling dynamics of photoexcited carriers in si studied using optical pump and terahertz probe spectroscopy," *Physical Review B*, vol. 83, no. 8, p. 085207, 2011.

[105] J. Knab, X. Lu, F. A. Vallejo, G. Kumar, T. E. Murphy, and L. M. Hayden, "Ultrafast carrier dynamics and optical properties of nanoporous silicon at terahertz frequencies," *Optical Materials Express*, vol. 4, no. 2, pp. 300–307, 2014.

[106] C. Pickering, M. Beale, D. Robbins, P. Pearson, and R. Greef, "Optical studies of the structure of porous silicon films formed in p-type degenerate and non-degenerate silicon," *Journal of Physics C: Solid State Physics*, vol. 17, no. 35, p. 6535, 1984.

[107] P. Badoz, D. Bensahel, G. Bomchil, F. Ferrieu, A. Halimaoui, P. Perret, J. Regolini, I. Sagnes, and G. Vincent, "Characterization of porous silicon: structural, optical and electrical properties," in *MRS Proceedings*, vol. 283, p. 97, Cambridge Univ Press, 1992.

[108] G. Vincent, F. Leblanc, I. Sagnes, P. Badoz, and A. Halimaoui, "Investigation of optical properties of free-standing porous silicon films by absorption and mirage effect," *Journal of luminescence*, vol. 57, no. 1, pp. 217–221, 1993.

[109] V. Lehmann and U. Gösele, "Porous silicon formation: a quantum wire effect," *Applied Physics Letters*, vol. 58, no. 8, pp. 856–858, 1991.

[110] R. Boyd and D. Prato, *Nonlinear Optics*. Nonlinear Optics Series, Academic Press, third ed., 2008.

[111] S. A. Anson, *Ultrafast spectroscopic measurement of the optical and electronic properties of narrow-band-gap semiconductor laser materials*. Thesis (phd), Engineering: Electronics and Electrical, Physics, The university of IOWA, dec 1999.

[112] R. Kaindl, D. Smith, M. Joschko, M. Hasselbeck, M. Woerner, and T. Elsaesser, "Femtosecond infrared pulses tunable from 9 to 18 μm at an 88-mhz repetition rate," *Optics letters*, vol. 23, no. 11, pp. 861–863, 1998.

[113] G. Vaillancourt, T. Norris, J. S. Coe, P. Bado, and G. Mourou, "Operation of a 1-khz pulse-pumped ti: sapphire regenerative amplifier," *Optics letters*, vol. 15, no. 6, pp. 317–319, 1990.

[114] G. Cheriaux, B. Walker, L. Dimauro, P. Rousseau, F. Salin, and J. Chambaret, "Aberration-free stretcher design for ultrashort-pulse amplification," *Optics letters*, vol. 21, no. 6, pp. 414–416, 1996.

[115] B. V. Olson, *Time-resolved measurements of charge carrier dynamics and optical nonlinearities in narrow-bandgap semiconductors*. The University of Iowa, 2013.

[116] B. V. Olson, *Time-resolved measurements of charge carriers dynamics and optical nonlinearities in narrow-bandgap semiconductors*. Thesis (phd), Physics, The university of Iowa, may 2013.

[117] W. He, I. V. Yurkevich, A. Zakar, and A. Kaplan, "High-frequency conductivity of optically excited charge carriers in hydrogenated nanocrystalline silicon investigated by spectroscopic femtosecond pump–probe reflectivity measurements," *Thin Solid Films*, vol. 592, pp. 287–291, 2015.

[118] E. Hecht, "Optics 4th edition," *Optics, 4th Edition, Addison Wesley Longman Inc, 1998*, 1998.

[119] M. Born and E. Wolf, "Principle of optics, 6th éd," 1980.

[120] E. Nichelatti, "Complex refractive index of a slab from reflectance and transmittance: analytical solution," *Journal of Optics A: Pure and Applied Optics*, vol. 4, no. 4, p. 400, 2002.

[121] M. Khashan and A. El-Naggar, "A new method of finding the optical constants of a solid from the reflectance and transmittance spectrograms of its slab," *Optics communications*, vol. 174, no. 5, pp. 445–453, 2000.

[122] O. Stenzel, V. Hopfe, and P. Klobes, "Determination of optical parameters for amorphous thin film materials on semitransparent substrates from transmittance and reflectance measurements," *Journal of Physics D: Applied Physics*, vol. 24, no. 11, p. 2088, 1991.

[123] E. Irene, "Applications of spectroscopic ellipsometry to microelectronics," *Thin Solid Films*, vol. 233, no. 1-2, pp. 96–111, 1993.

[124] J. C. Maxwell, *Matter and motion.* Courier Corporation, 1920.

[125] T. Roger, *Time resolved ultrafast dynamic excitations in semiconductors.* PhD thesis, University of Birmingham, 2013.

[126] M. Born and E. Wolf, "Principles of optics (; oxford," 1980.

[127] G. Jellison, G. Irene, and H. Tompkins, "Handbook of ellipsometry," *edited by HG Tompkins and EA Irene Springer, Heidelberg*, 2005.

[128] K. Seshan, *Handbook of thin film deposition.* William Andrew, 2012.

[129] H. W. Verleur, "Determination of optical constants from reflectance or transmittance measurements on bulk crystals or thin films," *JOSA*, vol. 58, no. 10, pp. 1356–1361, 1968.

[130] V. P. Tolstoy, I. V. Chernyshova, and V. A. Skryshevsky, *Handbook of Infrared Spectroscopy of Ultrathin Films*. Wiley Online Library, 2003.

[131] O. Heavens, "Optical properties of thin films," *Reports on Progress in Physics*, vol. 23, no. 1, p. 1, 1960.

[132] J. Heading, *An introduction to phase-integral methods*. Courier Corporation, 2013.

[133] A. Hartog and M. Adams, "On the accuracy of the wkb approximation in optical dielectric waveguides," *Optical and Quantum Electronics*, vol. 9, no. 3, pp. 223–232, 1977.

[134] J. J. Sakurai and E. D. Commins, "Modern quantum mechanics, revised edition," *American Journal of Physics*, vol. 63, no. 1, pp. 93–95, 1995.

[135] J. White and P. Heidrich, "Optical waveguide refractive index profiles determined from measurement of mode indices: a simple analysis," *Applied optics*, vol. 15, no. 1, pp. 151–155, 1976.

[136] H. Bremmer, "The wkb approximation as the first term of a geometric-optical series," *Communications on Pure and Applied Mathematics*, vol. 4, no. 1, pp. 105–115, 1951.

[137] K. Okamoto, *Fundamentals of optical waveguides*. Academic press, 2010.

[138] M. J. Adams, *An introduction to optical waveguides*, vol. 14. Wiley New York, 1981.

[139] H. Fujiwara, *Spectroscopic ellipsometry: principles and applications*. John Wiley & Sons, 2007.

[140] W. Theiß, "Optical properties of porous silicon," *Surface Science Reports*, vol. 29, no. 3-4, pp. 9195–93192, 1997.

[141] A. H. Sihvola, *Electromagnetic mixing formulas and applications*. No. 47, Iet, 1999.

[142] D. J. Bergman, "The dielectric constant of a composite materiala problem in classical physics," *Physics Reports*, vol. 43, no. 9, pp. 377–407, 1978.

[143] D. J. Bergman, "Hierarchies of stieltjes functions and their application to the calculation of bounds for the dielectric constant of a two-component composite medium," *SIAM Journal on Applied Mathematics*, vol. 53, no. 4, pp. 915–930, 1993.

[144] D. J. Bergman, "Rigorous bounds for the complex dielectric constant of a two-component composite," *Annals of Physics*, vol. 138, no. 1, pp. 78–114, 1982.

[145] W. Theiβ, "The dielectric function of porous siliconhow to obtain it and how to use it," *Thin Solid Films*, vol. 276, no. 1-2, pp. 7–12, 1996.

[146] W. Theiβ, S. Henkel, and M. Arntzen, "Connecting microscopic and macroscopic properties of porous media: choosing appropriate effective medium concepts," *Thin Solid Films*, vol. 255, no. 1-2, pp. 177–180, 1995.

[147] M. Evenschor, P. Grosse, and W. Theiss, "Optics of two-phase composites," *Vibrational spectroscopy*, vol. 1, no. 2, pp. 173–177, 1990.

[148] J. Sturm, P. Grosse, S. Morley, and W. Theiss, "Far infrared optical properties of metal-insulator composites," *Zeitschrift für Physik D Atoms, Molecules and Clusters*, vol. 26, no. 1, pp. 195–197, 1993.

[149] E. Gorges, P. Grosse, J. Sturm, and W. Theiss, "A parameterization of the effective dielectric function of a two-phase composite medium," *Zeitschrift für Physik B Condensed Matter*, vol. 94, no. 3, pp. 223–226, 1994.

[150] J. Sturm, P. Grosse, and W. Theiss, "Effective dielectric functions of alkali halide composites and their spectral representation," *Zeitschrift für Physik B Condensed Matter*, vol. 83, no. 3, pp. 361–365, 1991.

[151] J. M. Garnett, "Colours in metal glasses, in metallic films, and in metallic solutions. ii," *Philosophical Transactions of the Royal Society of London. Series A, Containing Papers of a Mathematical or Physical Character*, pp. 237–288, 1906.

[152] V. D. Bruggeman, "Berechnung verschiedener physikalischer konstanten von heterogenen substanzen. i. dielektrizitätskonstanten und leitfähigkeiten der mischkörper aus isotropen substanzen," *Annalen der physik*, vol. 416, no. 7, pp. 636–664, 1935.

[153] R. Landauer, "The electrical resistance of binary metallic mixtures," *Journal of Applied Physics*, vol. 23, no. 7, pp. 779–784, 1952.

[154] H. Looyenga, "Dielectric constants of heterogeneous mixtures," *Physica*, vol. 31, no. 3, pp. 401–406, 1965.

[155] H. Wallén, H. Kettunen, and A. Sihvola, "Composite near-field superlens design using mixing formulas and simulations," *Metamaterials*, vol. 3, no. 3, pp. 129–139, 2009.

[156] P. U. Jepsen, B. M. Fischer, A. Thoman, H. Helm, J. Suh, R. Lopez, and R. Haglund Jr, "Metal-insulator phase transition in a v o 2 thin film observed with terahertz spectroscopy," *Physical Review B*, vol. 74, no. 20, p. 205103, 2006.

[157] H. Ma, R. Xiao, and P. Sheng, "Third-order optical nonlinearity enhancement through composite microstructures," *JOSA B*, vol. 15, no. 3, pp. 1022–1029, 1998.

[158] D. Zhang, E. Cherkaev, and M. P. Lamoureux, "Stieltjes representation of the 3d bruggeman effective medium and padé approximation," *Applied Mathematics and Computation*, vol. 217, no. 17, pp. 7092–7107, 2011.

[159] G. A. Niklasson, C. Granqvist, and O. Hunderi, "Effective medium models for the optical properties of inhomogeneous materials," *Applied Optics*, vol. 20, no. 1, pp. 26–30, 1981.

[160] A. V. Goncharenko, "Generalizations of the bruggeman equation and a concept of shape-distributed particle composites," *Physical review E*, vol. 68, no. 4, p. 041108, 2003.

[161] M. Fox, "Optical properties of solids," 2002.

[162] D. Hulin, M. Combescot, J. Bok, A. Migus, J. Vinet, and A. Antonetti, "Energy transfer during silicon irradiation by femtosecond laser pulse," *Physical review letters*, vol. 52, no. 22, p. 1998, 1984.

[163] J. Shah, *Ultrafast spectroscopy of semiconductors and semiconductor nanostructures*, vol. 115. Springer Science & Business Media, 2013.

[164] A. Weiner, *Ultrafast optics*, vol. 72. John Wiley & Sons, 2011.

[165] J.-C. Diels and W. Rudolph, *Ultrashort laser pulse phenomena*. Academic press, 2006.

[166] A. Zakar, S. Park, V. Zerova, A. Kaplan, L. T. Canham, K. Lewis, and C. Burgess, "Mwir optical modulation using structured silicon membranes," in *SPIE Security+ Defence*, pp. 999203–999203, International Society for Optics and Photonics, 2016.

[167] G. Cocorullo and I. Rendina, "Thermo-optical modulation at 1.5 mu m in silicon etalon," *Electronics Letters*, vol. 28, no. 1, pp. 83–85, 1992.

[168] R. S. Jacobsen, K. N. Andersen, P. I. Borel, J. Fage-Pedersen, L. H. Frandsen, O. Hansen, M. Kristensen, A. V. Lavrinenko, G. Moulin, H. Ou, *et al.*, "Strained silicon as a new electro-optic material," *Nature*, vol. 441, no. 7090, pp. 199–202, 2006.

[169] B. Chmielak, M. Waldow, C. Matheisen, C. Ripperda, J. Bolten, T. Wahlbrink, M. Nagel, F. Merget, and H. Kurz, "Pockels effect based fully integrated, strained silicon electro-optic modulator," *Optics express*, vol. 19, no. 18, pp. 17212–17219, 2011.

[170] M. Vollmer and K.-P. Möllmann, *Infrared thermal imaging: fundamentals, research and applications*. John Wiley & Sons, 2010.

[171] U. Adomeit and R. Ebert, "Ir-dual-band-camera demonstrator: experimental assessment, practical applications," in *Optics/Photonics in Security and Defence*, pp. 673703–673703, International Society for Optics and Photonics, 2007.

[172] P. Fairley and H. Rutt, "Novel germanium infrared modulator," *Journal of Physics D: Applied Physics*, vol. 33, no. 21, p. 2837, 2000.

[173] S. Stepanov and S. Ruschin, "Modulation of light by light in silicon-on-insulator waveguides," *Applied physics letters*, vol. 83, no. 25, pp. 5151–5153, 2003.

[174] G. Chen, C. G. Bethea, R. Martini, P. Grant, R. Dudek, and H. Liu, "High-speed all-optical modulation of a standard quantum cascade laser by front facet illumination," *Applied Physics Letters*, vol. 95, no. 10, p. 101104, 2009.

[175] T. G. Euser and W. L. Vos, "Spatial homogeneity of optically switched semiconductor photonic crystals and of bulk semiconductors," *Journal of applied physics*, vol. 97, no. 4, p. 043102, 2005.

[176] D. J. Cho, W. Wu, E. Ponizovskaya, P. Chaturvedi, A. M. Bratkovsky, S.-Y. Wang, X. Zhang, F. Wang, and Y. R. Shen, "Ultrafast modulation of optical metamaterials," *Optics express*, vol. 17, no. 20, pp. 17652–17657, 2009.

[177] F. Z. Henari, K. Morgenstern, W. J. Blau, V. A. Karavanskii, and V. S. Dneprovskii, "Third-order optical nonlinearity and all-optical switching in porous silicon," *Applied physics letters*, vol. 67, no. 3, pp. 323–325, 1995.

[178] A. J. M. Abietar, J. B. Solbes, P. S. Kilders, J. V. G. Conejos, J. García-Rupérez, E. Jordana, P. Gautier, Y. Lebour, S. Hernández, R. Spano, *et al.*, "Ultrafast all-optical switching in a silicon-nanocrystal-based silicon slot waveguide at telecom wavelengths," in *Nano letters*, vol. 10, pp. 1506–1511, American Chemical Society, 2010.

[179] H. Cai, S. Liu, E. Lalanne, D. Guo, X. Chen, X. Wang, F.-S. Choa, and A. M. Johnson, "Femtosecond measurements of near-infrared pulse induced

mid-infrared transmission modulation of quantum cascade lasers," *Applied Physics Letters*, vol. 104, no. 21, p. 211101, 2014.

[180] D. Thomson, L. Shen, J. Ackert, E. Huante-Ceron, A. Knights, M. Nedeljkovic, A. Peacock, and G. Mashanovich, "Optical detection and modulation at 2μm-2.5 μm in silicon," *Optics express*, vol. 22, no. 9, pp. 10825–10830, 2014.

[181] J. Chiles and S. Fathpour, "Mid-infrared integrated waveguide modulators based on silicon-on-lithium-niobate photonics," *Optica*, vol. 1, no. 5, pp. 350–355, 2014.

[182] L. Shen, N. Healy, C. J. Mitchell, J. S. Penades, M. Nedeljkovic, G. Z. Mashanovich, and A. C. Peacock, "Mid-infrared all-optical modulation in low-loss germanium-on-silicon waveguides," *Optics letters*, vol. 40, no. 2, pp. 268–271, 2015.

[183] Y. Chabal and S. Christman, "Evidence of dissociation of water on the si (100) 2× 1 surface," *Physical Review B*, vol. 29, no. 12, p. 6974, 1984.

[184] V. Dubin, F. Ozanam, and J.-N. Chazalviel, "In situ luminescence and ir study of porous silicon during and after anodic oxidation," *Thin Solid Films*, vol. 255, no. 1-2, pp. 87–91, 1995.

[185] L. Fekete, F. Kadlec, P. Kužel, and H. Němec, "Ultrafast opto-terahertz photonic crystal modulator," *Optics letters*, vol. 32, no. 6, pp. 680–682, 2007.

[186] W. Spitzer and H. Fan, "Infrared absorption in n-type silicon," *Physical Review*, vol. 108, no. 2, p. 268, 1957.

[187] D. Chekulaev, V. Garber, and A. Kaplan, "Free carrier plasma optical response and dynamics in strongly pumped silicon nanopillars," *Journal of Applied Physics*, vol. 113, no. 14, p. 143101, 2013.

[188] S. A. Miller, M. Yu, X. Ji, A. G. Griffith, J. Cardenas, A. L. Gaeta, and M. Lipson, "Low-loss silicon platform for broadband mid-infrared photonics," *arXiv preprint arXiv:1703.03517*, 2017.

[189] A. R. Motamedi, A. H. Nejadmalayeri, A. Khilo, F. X. Kärtner, and E. P. Ippen, "Ultrafast nonlinear optical studies of silicon nanowaveguides," *Optics express*, vol. 20, no. 4, pp. 4085–4101, 2012.

[190] J. Meitzner, F. G. Moore, B. M. Tillotson, S. D. Kevan, and G. L. Richmond, "Time-resolved measurement of free carrier absorption, diffusivity, and internal quantum efficiency in silicon," *Applied Physics Letters*, vol. 103, no. 9, p. 092101, 2013.

[191] D. Reitze, T. Zhang, W. M. Wood, and M. C. Downer, "Two-photon spectroscopy of silicon using femtosecond pulses at above-gap frequencies," *JOSA B*, vol. 7, no. 1, pp. 84–89, 1990.

[192] T. Y. Choi and C. P. Grigoropoulos, "Plasma and ablation dynamics in ultrafast laser processing of crystalline silicon," *Journal of applied physics*, vol. 92, no. 9, pp. 4918–4925, 2002.

[193] J. Bonse, "All-optical characterization of single femtosecond laser-pulse-induced amorphization in silicon," *Applied Physics A: Materials Science & Processing*, vol. 84, no. 1, pp. 63–66, 2006.

[194] M. Agranat, S. Ashitkov, S. Anisimov, A. Ovchinnikov, A. Shvartsburg, D. Sitnikov, and V. Fortov, "Formation of absorbing heterogeneous plasma layer by femtosecond laser-induced melting and ablation of silicon," *Applied Physics A: Materials Science & Processing*, vol. 94, no. 4, pp. 879–887, 2009.

[195] P. Malỳ, F. Trojanek, A. Hospodkova, V. Kohlova, and I. Pelant, "Transmission study of picosecond photocarrier dynamics in free-standing porous silicon," *Solid state communications*, vol. 89, no. 8, pp. 709–712, 1994.

[196] P. Malỳ, F. Trojánek, J. Kudrna, A. Hospodková, S. Banáš, V. Kohlová, J. Valenta, and I. Pelant, "Picosecond and millisecond dynamics of photoexcited carriers in porous silicon," *Physical Review B*, vol. 54, no. 11, p. 7929, 1996.

[197] P. Fauchet, "Ultrafast carrier dynamics in porous silicon," *physica status solidi (b)*, vol. 190, no. 1, pp. 53–62, 1995.

[198] W. He, A. Zakar, T. Roger, I. V. Yurkevich, and A. Kaplan, "Determination of recombination coefficients for nanocrystalline silicon embedded in hydrogenated amorphous silicon," *Optics letters*, vol. 40, no. 16, pp. 3889–3892, 2015.

[199] A. J. Nozik, "Nanoscience and nanostructures for photovoltaics and solar fuels," *Nano letters*, vol. 10, no. 8, pp. 2735–2741, 2010.

[200] F. Priolo, T. Gregorkiewicz, M. Galli, and T. F. Krauss, "Silicon nanostructures for photonics and photovoltaics," *Nature nanotechnology*, vol. 9, no. 1, pp. 19–32, 2014.

[201] C. Smith and D. Binks, "Nanomaterials 2014, 4, 19–45."

[202] K.-G. Gan, C.-K. Sun, S. P. DenBaars, and J. E. Bowers, "Ultrafast valence intersubband hole relaxation in ingan multiple-quantum-well laser diodes," *Applied physics letters*, vol. 84, no. 23, pp. 4675–4677, 2004.

[203] K. W. Williams, N. R. Monahan, T. J. Evans, and X.-Y. Zhu, "Direct time-domain view of auger recombination in a semiconductor," *Physical Review Letters*, vol. 118, no. 8, p. 087402, 2017.

[204] U. Bockelmann and G. Bastard, "Phonon scattering and energy relaxation in two-, one-, and zero-dimensional electron gases," *Physical Review B*, vol. 42, no. 14, p. 8947, 1990.

[205] P. Han and G. Bester, "Carrier relaxation in colloidal nanocrystals: Bridging large electronic energy gaps by low-energy vibrations," *Physical Review B*, vol. 91, no. 8, p. 085305, 2015.

[206] S. Xu, A. Mikhailovsky, J. Hollingsworth, and V. Klimov, "Hole intraband relaxation in strongly confined quantum dots: Revisiting the phonon bottleneck problem," *Physical Review B*, vol. 65, no. 4, p. 045319, 2002.

[207] A. Cullis, L. T. Canham, and P. Calcott, "The structural and luminescence properties of porous silicon," *Journal of Applied Physics*, vol. 82, no. 3, pp. 909–965, 1997.

[208] O. Bisi, S. Ossicini, and L. Pavesi, "Porous silicon: a quantum sponge structure for silicon based optoelectronics," *Surface science reports*, vol. 38, no. 1, pp. 1–126, 2000.

[209] P. Jonsson, H. Bleichner, M. Isberg, and E. Nordlander, "The ambipolar auger coefficient: Measured temperature dependence in electron irradiated and highly injected n-type silicon," *Journal of applied physics*, vol. 81, no. 5, pp. 2256–2262, 1997.

[210] A. W. Cohn, A. M. Schimpf, C. E. Gunthardt, and D. R. Gamelin, "Size-dependent trap-assisted auger recombination in semiconductor nanocrystals," *Nano letters*, vol. 13, no. 4, pp. 1810–1815, 2013.

[211] A. Sabbah and D. M. Riffe, "Measurement of silicon surface recombination velocity using ultrafast pump–probe reflectivity in the near infrared," *Journal of Applied Physics*, vol. 88, no. 11, pp. 6954–6956, 2000.

[212] S. Tanaka, T. Ichibayashi, and K. Tanimura, "Dynamics of bulk-to-surface electron transitions on si (001)-(2× 1) studied by time-resolved two-photon photoemission spectroscopy," *Physical Review B*, vol. 79, no. 15, p. 155313, 2009.

[213] M. Casassa, E. Heilweil, J. Stephenson, and R. Cavanagh, "Time-resolved measurements of oh (v= 1) vibrational relaxation on SiO2 surfaces: Isotope and temperature dependence," *The Journal of Chemical Physics*, vol. 84, no. 4, pp. 2361–2364, 1986.

[214] K. Jobson, J.-P. Wells, N. Vinh, P. Phillips, C. Pidgeon, and J. Dijkhuis, "Mid-infrared pump–probe spectroscopy of si–h stretch modes in porous silicon," *Optical materials*, vol. 30, no. 5, pp. 740–742, 2008.

[215] Z. Wang, J. Zhang, S. Xu, L. Wang, Z. Cao, P. Zhan, and Z. Wang, "1d partially oxidized porous silicon photonic crystal reflector for mid-infrared application," *Journal of Physics D: Applied Physics*, vol. 40, no. 15, p. 4482, 2007.